Advanced Modulation for Optical Communication Systems

Thèse

Aminreza Yekani Khoei

Doctorat en génie électrique
Philosophiæ doctor (Ph. D.)

Québec, Canada

Advanced Modulation for Optical Communication Systems

Thèse

Aminreza Yekani Khoei

Sous la direction de:

Leslie A. Rusch, directeur de recherche

Résumé

La demande toujours croissante pour la capacité du réseau conduit au développement de systèmes de communication optique pour couvrir les normes Terabit Ethernet récemment proposées. Les applications de courte distance nécessitent une solution peu coûteuse et peu complexe avec détection directe. Cependant, le coût de la détection cohérente diminue chaque jour et en fait un bon candidat pour les applications à courte distance futures afin d'accroître l'efficacité spectrale et d'utiliser des formats de modulation avancés. Dans cette thèse, nous étudions des solutions pour les applications court-courrier actuelles et futures.

Dans la première partie, nous nous concentrons sur des solutions pour les applications de courte distance. Le premier chapitre est la première démonstration de la transmission multi-tonalité discrète (DMT) à plus de 100 Gb/s en utilisant une photonique au silicium en bande O (SiP). Nous comparons expérimentalement le DMT avec la modulation d'amplitude d'impulsion (PAM) sur la bande O. Notre expérience montre qu'en augmentant la longueur des fibres de plus de 10 km, la PAM surpasse le DMT. Pour la bande C, nous utilisons un multi-ton discret à bande latérale unique (SSB-DMT) pour éviter l'effet d'évanouissement de la puissance induit par la dispersion chromatique. Nous étudions l'effet du bruit de phase, de la dispersion chromatique et de la sensibilité du récepteur pour optimiser le signal du DMT et extraire des équations théoriques pour calculer le taux d'erreur binaire (BER) du SSB-DMT. Ensuite, nous comparons la PAM sur bande O avec le SSB-DMT sur bande C et quantifions l'impact des limitations imposées par le matériel sur les deux formats de modulation. Notre étude fournit un outil analytique pour les applications de courte distance afin de sélectionner le format et le matériel de modulation appropriés en fonction de la portée requise, du débit binaire, etc.

Dans la deuxième partie, le ciblage des futurs systèmes de détection cohérents justifie l'utilisation d'un format de modulation complexe avec détection cohérente. Nous utilisons un format de modulation avancé dans lequel nous avons combiné la propagation de transformée de Fourier discrète avec le DMT pour augmenter l'efficacité spectrale. Le format de modulation hybride a un rapport de puissance crête à moyenne inférieur (vis-à-vis du DMT) et une efficacité spectrale plus élevée (vis-à-vis de la QAM à porteuse unique). Dans la première étape, nous comparons expérimentalement les performances des modulations hybrides, DMT

standard et monoporteuse en utilisant un modulateur SiP IQ. Ensuite, nous développons une stratégie de contrôle pour le format de modulation hybride en échangeant la non-linéarité de la fonction de transfert du modulateur et le rapport signal / bruit optique. Le format de modulation hybride est ensuite optimisé pour avoir un débit maximum. En utilisant une simulation de Monte Carlo, nous comparons le format de modulation hybride optimisé avec le DMT standard pour différents débits binaires. Enfin, nous avons une comparaison de complexité entre hybride et DMT pour différentes longueurs de fibre.

Abstract

Ever increasing demand for network capacity is driving the development of optical communication systems to cover recently proposed Terabit Ethernet standards. Short haul applications need low cost and low complexity solutions with direct detection, as the cost of coherent detection comes down, it will become a good candidate for future short-haul applications to increase spectral efficiency and exploit advanced modulation formats. In this thesis, we investigate solutions for both current and future short-haul systems.

In the first part, we focus on solutions for short haul applications. The first chapter is the first time demonstration of more than 100 Gb/s discrete multi-tone (DMT) transmission using an O-band silicon photonics (SiP). We experimentally compare DMT with pulse amplitude modulation (PAM) on O-band. Our experiment shows that by increasing fiber length more than 10 km, PAM outperforms DMT. For C-band, we use single sideband discrete multi-tone (SSB-DMT) to avoid chromatic dispersion-induced power fading effect. We study the effect of phase noise, chromatic dispersion, and receiver sensitivity to optimize DMT signal and extract theoretical equations to calculate bit error rate (BER) of SSB-DMT. Next, we analytically compare PAM on O-band with SSB-DMT on C-band and quantify the impact of hardware-imposed limitations on both modulation formats. Our study provides an analytical tool for short haul applications to select appropriate modulation format and hardware based on required reach, bit rate, etc.

In the second part we examine complex modulation formats that will be enabled in the future by low cost, integrated components for coherent detection.. We use an advanced modulation format in which we combined discrete Fourier transform spread with DMT to increase spectral efficiency. Hybrid modulation format has a lower peak to average power ratio (vis-a-vis DMT) and higher spectral efficiency (vis-a-vis single carrier QAM). In the first step, we experimentally compare the performance of the hybrid, standard DMT, and single carrier modulations using a SiP IQ modulator. Next, we develop a driving strategy for hybrid modulation format by trading off the modulator transfer function non-linearity and optical signal to noise ratio. Then hybrid modulation format is optimized to have maximum throughput. Using Monte Carlo simulation we compare optimized hybrid modulation format with standard DMT for different bit rates. Finally, we have a complexity comparison between hybrid

and DMT for different fiber lengths to motivate same investigation for long-haul applications where, we should consider fiber non-linearity, attenuation,a polarization multiplexing.

Contents

List of Tables

List of Figures

Abbreviations

ADC	Analog-to-digital converter
ASE	Amplified spontaneous emission
ASIC	Application specific integrated circuit
AWGN	Additive white Gaussian noise
B2B	Back-to-back
BER	Bit error rate
BR	Baud rate
CAGR	Compound annual growth rate
CD	Chromatic dispersion
CMOS	Complementary metal oxide semiconductor
CO Rx	Coherent receiver
CPR	Carrier phase recovery
CPS	number of complex multipliers per signal symbol
CPB	number of complex multipliers per bit
DAC	Digital-to-analog converter
DC	Direct current
DD-LMS	Decision-directed least mean square error
DDMZM	dual drive Mach-Zehnder modulator
DFE	Decision-feedback equalizers
DFT	Discrete Fourier transform
DFT-S	Discrete Fourier transform spread
DMT	Discrete multi-tone
DSP	Digital signal processing
EDFA	Erbium-doped fiber amplifier
EVM	Error vector magnitude
FDE	Frequency domain implementation of equalizer
FEC	Forward error correction
FFT	Fast Fourier transform
FOC	Frequency offset compensation
FPGA	Field programmable gate array
GbE	Gigabit Ethernet

HD	High definition
ICI	Inter-carrier interference
IFFT	Inverse fast Fourier transform
IMDD	Intensity modulation with direct detection
IQM	IQ modulator
ISI	Inter-symbol interference
LD	Laser diode
LO	Local oscillator
MQAM	M-ary quadrature amplitude modulation
MMSE	Minimum mean square error
MMA	Multi-modulus algorithm
MMSE	Minimum mean square error
MZM	Mach-Zehnder modulator
NN	Nearest neighbor
OBPF	Optical bandpass filter
OFDM	Orthogonal frequency-division multiplexing
OOK	On-off keying
OSNR	Optical signal-to-noise ratio
P2A	Phase-to-amplitude
P/S	Parallel-to-serial
PAM	Pulse amplitude modulation
PAPR	Peak-to-average power ratio
PD	Photodiode
PON	Passive optical network
PR	Phase rotation
PRBS	Pseudorandom binary sequence
PSD	Power spectral density
QAM	Quadrature amplitude modulation
QPSK	Quadrature phase-shift keying
RF	Radio frequency
RS	Receiver sensitivity
RTO	Real-time oscilloscope
S/P	Serial-to-parallel
SCR	Signal-to-carrier power ratio
SE	Spectral efficiency
SER	Symbol error rate
SiP	Silicon photonics
SMF	Single-mode fiber

SNR	Signal-to-noise ratio
SSB	Single sideband
SSB-DMT	Single sideband discrete multi-tone
SSBI	Signal-signal beat interference
TDE	Time domain implementation of equalizer
SSBI	Signal-signal beat interference
VNI	Visual networking index
VR	Virtual reality
WDM	Wavelength-division multiplexing

List of Symbols

γ^2	Signal-to-carrier power ratio
γ	Signal-to-carrier amplitude ratio
N_d	Number of data carrying sub-channels
s_{DMT}	DMT signal
A_c	Optical carrier amplitude
f_c	Optical carrier frequency
$\Phi(t)$	Laser phase noise
$\Delta\nu$	Laser linewidth
Δf	Sub-channel frequency spacing
p_k	Allocated power of k^{th} sub-channel
d_k	Normalized complex amplitude of k^{th} sub-channel
N	Number of sub-channels
T_k	Time delay for k^{th} sub-channel
c	Speed of light in vacuum
D	Dispersion
L	Fiber length
P_c	Carrier power
ρ_k	Phase fluctuation of k^{th} sub-channel
θ_k	Phase of k^{th} sub-channel
J_n	n^{th} order Bessel function of the first kind
λ	Optical carrier wavelength
σ^2	Noise power
P_s	Overall signal power
α_k	The power degradation of the k^{th} sub-channel due to phase noise
β_k	Phase noise power in thek^{th} sub-channel
T_s	Sampling time
M_k	Delay relative to the carrier (in number of samples) for the k^{th} sub-channel
B	Signal bandwidth
P_N	Noise power
R_b	Signal bit rate
f_s	Sampling frequency

E_s	Energy of signal
N_0	Noise spectral density
BR	Signal baud rate
V_{pp}	Peak-to-peak voltage
N_{DMT}	Number of subchannels dedicated to DMT partition of hybrid modulation
N_{QAM}	Number of subchannels dedicated to DFT-S QAM partition of hybrid modulation
N_{SPS}	Number of samples per symbol
N_{eq}	Number of equalizer taps

To my wife Shabnam,
to my parents,
and to my sister Elmira

Acknowledgment

Firstly, I would like to express my sincere gratitude to my supervisor Professor Leslie Ann Rusch for her patience, motivation, and immense knowledge. Her priceless guidance helped me grow both professionally and personally. She never hesitated to devote her time to me, and I will forever be grateful of all the time she did not spare on advising me with my research and her guidance in my academic cultivation.

I would like to thank the members of jury, Prof. Sophie LaRochelle, Prof. John Cartledge, and Prof. Paul Fortier, for taking the time to read my thesis and for valuable comments and suggestions.

A special thanks to Siamak Amiralizadeh my old friend and colleague that we had hours of fruitful discussions and I learned a lot from him. Many thanks to all members of optical communications group at COPL.

I cannot forget my best friend, Roozbeh who was there during hard times, cheered me on, and celebrated each accomplishment.

Finally, I want to thank my true love, Shabnam, for her constant and unfailing love and support that made the completion of thesis possible. My deepest gratitude to my family. Words cannot express how grateful I am to my mother, father, and sister for all of the sacrifices that you've made on my behalf. Your prayer for me was what sustained me thus far.

Foreword

Five chapters of this thesis are based on the material published in journal papers and conferences. I am the main contributor for all of these publications. In the following, the detailed contribution of each co-author is provided.

Chapter 2: A. Yekani, M. Chagnon, C. S. Park, M. Poulin, D. V. Plant and L. A. Rusch, "Experimental comparison of PAM vs. DMT using an O-band silicon photonic modulator at different propagation distances,", *European Conference on Optical Communication*, 2015 [1]. This paper demonstrates an experimental comparison between PAM and DMT using an O-band mach-Zehnder modulator. Mathieu Chagnon provided the experimental result for PAM modulation, Chul Soo Park assisted me in the experiments. Michel Poulin designed the silicon photonics modulator. Leslie Rusch was the supervisor. I was responsible for DMT experiment and comparing DMT with PAM. The paper was written by me and revised by Leslie Rusch and David Plant.

Chapter 3: A. Yekani, S. Amiralizadeh, and L. A. Rusch, "Analytical Study of Optical SSB-DMT with IMDD", *Journal of Lightwave Technology*, vol. 36, no. 3, pp. 666–674, Apr. 2018. [2]. In this paper, we provide an analytical study of SSB-DMT on C-band that quantifies the impact of signal-to-signal beating interference, phase to amplitude noise receiver sensitivity, and chromatic dispersion. I had fruitful discussions with Siamak Amiralizadeh about extracting theoretical expressions of SNR per subchannel for single side band DMT. Leslie Rusch was the supervisor of the project. All of the simulations and theoretical analysis were performed by me. The manuscript was prepared by me and revised by Leslie Rusch.

Chapter 4: A. Yekani, and L. A. Rusch, "Interplay of Bit Rate, Linewidth, and Reach on Optical DMT and PAM with IMDD", *submitted to IEEE Transactions on Communications*. In this paper, we develop an analytical comparison between O-band PAM and C-band DMT. We provide a tool to select modulation format, to select appropriate hardware (modulators and laser sources), or to quantify attainable bit rates. Leslie Rusch was the supervisor of the project. All of the simulations and theoretical analysis were performed by me. The manuscript was prepared by me and revised by Leslie Rusch.

Chapter 5: A. Yekani, M. Banawan, and L. A. Rusch, "Flexible Modulation and Fre-

quency Allocations for SNR-limited Coherent Systems", *Canadian conference on electrical and computer engineering*, 2018. In this paper, we use hybrid modulation format to increase the throuput of an IQ SiP modulator on C-band. Our hybrid signal is a mix of DFT-S QAM for low frequencies and DMT for high frequencies. We experimentally compare the performance of hybrid, DMT and single carrier modulation formats. Mai Banawan assisted me in developing the idea and presenting the paper. Leslie Rusch was the supervisor of the project. I ran the experiments, processed the captured experimental data and performed the comparison. The manuscript was prepared by me and revised by Leslie Rusch.

Chapter 6: A. Yekani, and L. A. Rusch, "Numerical Study of a Hybrid Optical DMT/DFT-S QAM Modulation", *submitted to Journal of Lightwave Technology*. In this paper, we provide a numerical study to optimize hybrid modulation format and maximize system throughput. We compare hybrid modulation with standard DMT in terms of bit rate and implementation complexity. Our hybrid signal is a mix of discrete Fourier transform spread (DFT-S) QAM for low frequencies and DMT for high frequencies. Leslie Rusch was the supervisor of the project. All of the simulations and numerical analysis were performed by me. The manuscript was prepared by me and revised by Leslie Rusch.

Chapter 1

Introduction

1.1 Motivation

In recent years social networking, ultra high definition (HD) video streaming, virtual reality (VR) streaming and etc. have caused an enormous growth in worldwide data traffic and the demand for network capacity. Based on Cisco visual networking index (VNI), Table 1.1 shows the global IP traffic as well as compound annual growth rate (CAGR) since 2016 until 2021. Predicted CAGR is 23% for fixed Internet and even higher for mobile data. Figure 1.1 shows the IP traffic growth for data centers in 2021 will be 20.6 zettabyte. The portion of data traffic for short range, within data center communications is 71.5% and the rest is for longer communication distances including 13.6% data center to data center, and 14.9% data center to user [3, 4].

Table 1.1 – Global IP traffic, 2016–2021 (Petabytes [PB] per Month).

	2016	2017	2018	2019	2020	2021	CAGR (2016–2021)
Fixed Internet	65,942	83,371	102,960	127,008	155,121	187,386	23%
Managed IP	22,911	27,140	31,304	35,226	38,908	42,452	13%
Mobile data	7,201	11,183	16,646	24,220	34,382	48,270	46%

Optical communication faced huge advance to meet the ever-increasing demand in network capacity and data transmission. Every few years, IEEE introduces new standardization that requires more transmission speed compared to previous ones. The most recent standard is 400 GbE (Gigabit Ethernet), which is the second step of Terabit Ethernet after 200 GbE. Both standards are developed by IEEE 802.3bs task force. Transmission speed of 400 Gb/s could be provided by wavelength division multiplexing 16 lanes of 25 Gb/s, 8 lanes of 50 Gb/s, or 4 lanes of 100 Gb/s. Two first options are commercially available but the third one is still a challenge for research groups to find the optimum way to achieve such transmission speed

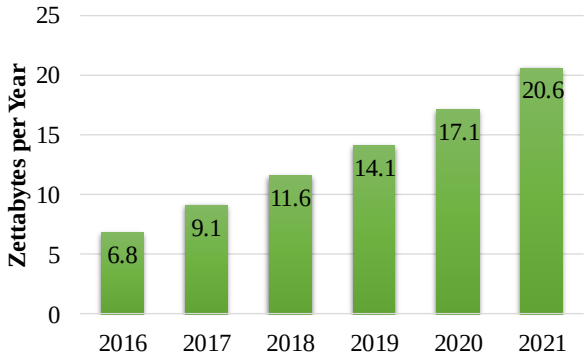

Figure 1.1 – Global data center IP traffic growth.

in all parts of the network such as data centers (fiber length < 10 km), passive optical networks (fiber length < 60 km), metro (fiber length < 100 km), and long haul (fiber length > 100 km). And the next step, 800 GbE, will not happen until single lane 100 Gb/s would be commercially available.

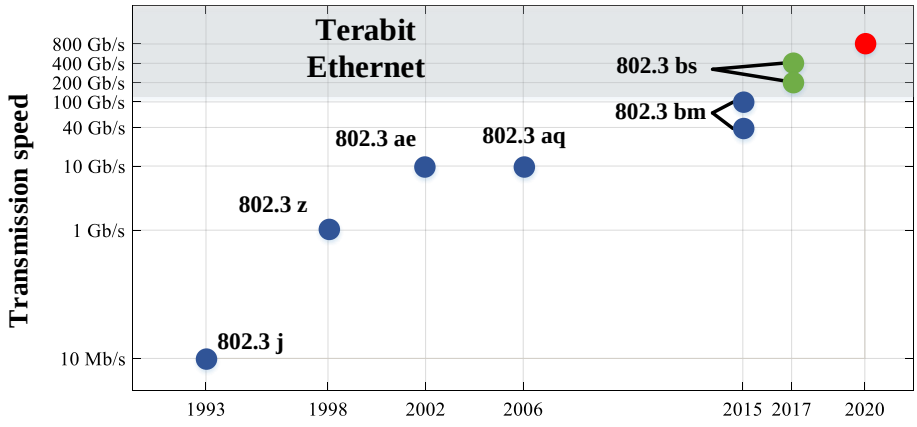

Figure 1.2 – IEEE Ethernet standards over fiber.

Solutions for new standardization are provided in two main sections. Section one is for data centers and passive optical networks (PON), where cost and complexity are important. Section two is for future coherent detection systems where reduced implementation cost justifies the use of advanced modulation and coherent detection.

1.2 General discussion

1.2.1 Short haul application

Data centers and PONs require lower cost and lower complexity compared to other links. Use of intensity modulation and direct detection (IMDD) is a promising solution for this market. Pulse amplitude modulation (PAM) and discrete multi-tone (DMT) are both good candidates to achieve high transmission rate because of high spectral efficiency and low complexity due to their compatibility with IMDD.

Developing high-speed devices that meet the requirement of data centers, attracts research groups to use silicon as the host material for fabricating active and passive components. Silicon photonics (SiP) technology provides a low cost solution for data centers which also has the capability of large scale integration and high yield manufacturing process [5]. Another interesting aspect of SiP technology is its compatibility with integration with complementary metal oxide semiconductor (CMOS) technology. This helps SiP to leverage existing CMOS techniques and fabricate both electrical and optical devices in a single chip and reduce the footprint and cost.

To be able to design an IMDD system using a SiP modulator for short haul applications we need to decide which frequency band our modulator should support. There are two available bands for high speed data communication in terms of low cost optical components, the first one is O-band (1310 nm) and the other one is C-band (1550 nm). O-band has zero dispersion on single mode fibers, so we will not have dispersion caused degradation such as power fading in our IMDD system. But on the other hand O-band has higher attenuation compared to C-band. Therefore, each band could be a better choice for different applications.

This motivates the subject of part I of this thesis, where we concentrate on low cost low complexity direct detection system as a solution for short haul applications and compare PAM with DMT experimentally and numerically. The main goal of this part is to provide a analytical tool to select the best hardware and modulation choice depending on the application requirements for short range optical communication.

1.2.2 Coherent detection systems

Moving to the case of future coherent detection systems with low implementation costs, we can consider using coherent detection with advanced modulation formats to first of all double the spectral efficiency by sending complex signal, and also to be able to compensate phase related degradation. While our study is limited to short reach applications of future coherent detection systems, they could be extended to long haul application by including attenuation and nonlinear effects induced by a long fiber length and introducing second polarization.

Modulation schemes for single lane transmission with coherent detection can be catego-

rized into two major types of single carrier and multicarrier. Using multicarrier modulation format such as DMT helps us to divide frequency range into smaller subchannels and have the freedom of allocating different number of bits as well as power for different sub channels. However the DMT signal has a high peak-to-average power ratio (PAPR), which increases quantization noise and nonlinearity from modulator transfer function and electrical amplifiers.

Single carrier modulation on the other hand, has lower PAPR but it is not compatible with bit allocation. The spectral efficiency of single carrier quadrature amplitude modulation (QAM) depends on the pulse shaping method we use and the highest spectral efficiency belongs to the Nyquist pulse shape.

Recently a hybrid modulation is introduced that combines QAM modulation where the frequency response is almost flat with DMT where we have steep slope in frequency response of the system and we have to adapt our signal with frequency selective variations. This combination has lower PAPR compared to DMT and higher spectral efficiency compared to QAM.

This motivates the subject of part II of this thesis, where we use a hybrid modulation format and experimentally compare it with both multicarrier and single carrier modulation schemes. After the comparison we have a numerical study to optimize hybrid modulation and maximize the throughput. The main goal of this part is to seek the advantages of hybrid modulation format and propose a methodology to optimize hybrid modulation format to have the maximum capacity.

1.3 Thesis Outline

1.3.1 Part I: Short haul application (data centers and passive optical networks)

In chapter 2, for the first time, we demonstrate more than 100 Gb/s transmission of DMT signal with silicon modulator as a promising solution for data centers. The SiP modulator we used in this work is a single drive Mach-Zehnder modulator on O-band with push pull configuration. The performance of DMT is compared to PAM in different fiber lengths. As expected, we had different behavior for DMT and PAM. For Data centers up to 10 km DMT was a better solution but by increasing fiber length to 20 km PAM outperforms DMT. Our experiments show that increasing fiber length has less impact on PAM compared to DMT. Our contributions in this chapter are:

- First demonstration of DMT at 100 Gb/s on a SiP modulator with direct detection for up to 20 km transmission.

- Comparison of experimental results of DMT vs. PAM bit rate and reach in O-band with SiP modulator.

In chapter 3, we propose a theoretical study of the single sideband discrete multi-tone (SSB-DMT) performance in the C-band with IMDD. In this study, we considered dispersion, phase noise, attenuation, limited system 3 dB bandwidth (the combined electrical and optical bandwidth), and additive white Gaussian noise as main degradation sources. The interaction phase-to-amplitude noise (P2A) and signal-to-signal beating interference (SSBI) was studied to optimize signal-to-carrier power ratio (SCR). Signal-to-noise ratio (SNR) is calculated for each suchannel and compared to the simulation to validate our study. Analytical equations are provided to calculate bit error rate (BER) of SSB-DMT. DMT performance is examined in various system parameters of laser linewidth system 3-dB bandwidth, and fiber length. Our contributions in this chapter are:

- An analytical study of SSB-DMT on C-band that quantifies the impact of signal-to-signal beating interference, phase to amplitude noise receiver sensitivity, and chromatic dispersion.
- A method to find the signal to carrier power ratio of SSB-DMT with minimum BER by trading off SSBI and P2A impairments.

In chapter 4, we compare the performance of two most promising solutions of 400 GbE standardization: SSB-DMT in C-band, and PAM4 on O-band. In section 2, we experimentally show that PAM outperforms DMT when the fiber length increases. Because of this reason we chose PAM as the best candidate for O-band and using our study in chapter 3 we developed an analytical comparison. Our comparison has been done for different laser linewidths, fiber lengths, and system 3 dB bandwidth (the combined electrical and optical bandwidth). Our comparison gives a tool to select modulation format, to select appropriate hardware (modulators and laser sources), or to quantify attainable bit rates for data centers and PON applications. Our contributions in this chapter are:

- We study the disparate effect of system bandwidth, laser linewidth, and data rate on PAM and DMT modulation.
- An analytical comparison of low complexity, un-precompensated PAM on O-band and SSB-DMT on C-band in terms of BER and achievable bit rate.

1.3.2 Part II: Long haul application or future coherent detection systems

In chapter 5, for the first time, we have a demonstration of hybrid modulation using a IQ SiP modulator. We experimentally compare the performance of hybrid modulation with

standard DMT and single carrier QAM modulation. Our hybrid modulation is a mix of discrete Fourier transform spread (DFT-S) of QAM modulation and DMT. DFT-S QAM is used in low frequencies where the frequency response is almost flat and DMT is used for the rest to utilize water-filling technique to maximize the capacity. We show that BER for hybrid modulation is lower in expense of higher complexity. Our contributions in this chapter are:

- First demonstration of hybrid DFT-S QAM/DMT modulation on a SiP IQ modulator.
- Experimental comparison of hybrid, standard DMT and single carrier QAM on a SiP IQ modulator.

In chapter 6, we propose a driving strategy for hybrid modulation format to minimize BER. In our strategy, we consider transfer function nonlinearity, system additive white Gaussian noise (AWGN) and system 3 dB bandwidth (the combined electrical and optical bandwidth) as the main noise contributions. We optimize the hybrid combination by choosing the best frequency occupation as well as modulation order for DFT-S QAM part. We show how changing the split point changes the performance of hybrid modulation. For the first time, we compare the complexity of hybrid modulation with standard DMT. The complexity is calculated in terms of number of required complex multipliers per bit. Our study shows that the complexity of hybrid modulation is much higher than standard DMT and clearly hybrid is not a good solution for short haul applications. We consider the dispersion compensation block when the fiber length increases and we show that the complexity gap between hybrid and DMT becomes reasonable even for long haul applications. Our contributions in this chapter are:

- A driving strategy for hybrid modulation format, to minimize the effect of modulator transfer function nonlinearity and optical signal-to-noise ratio (OSNR).
- An optimized hybrid modulation format in terms of frequency occupation and modulation order in the DFT-S section.
- A performance comparing of optimized hybrid modulation vis-avis standard DMT for back-to-back.
- A comparison of the complexity for hybrid modulation with standard DMT.

1.3.3 Appendices

Four appendices are included at the end of this thesis. In Appendix A we explain our method of calculating SNR per subchannel for DMT modulation format; this method is used in all chapters when we generate DMT signals and use water-filling technique. In Appendix B we

explain our numerical simulation for uniform SSB-DMT used in chapter 3. This simulation is used to validate our theoretical results predicting SNR per subchannel for SSB-DMT. In appendix C we calculate SNR per subchannel of SSB-DMT assuming SSBI as the only impairment. In Appendix D we provide details of our symbol error rate calculation for a MQAM modulation with AWGN and phase rotation. Appendices C and D are used in chapter 3 to calculate the SNR per subchannel then calculate BER for SSB-DMT signal.

Part I

Short Haul Applications (Data Centers and Passive Optical Networks)

Chapter 2

Experimental Comparison of PAM vs. DMT using an O-Band Silicon Photonic Modulator at Different Propagation Distances

2.1 Résumé

Nous comparons expérimentalement le PAM et le DMT en utilisant le modulateur d'intensité photonique au silicium 1310 nm pour quatre longueurs de fibre. DMT atteint 120 Gb/s à 2 km et 110 Gb/s à 10 km, en dessous du seuil forward error correction (FEC) de 3.8e-3.

2.2 Abstract

We experimentally compare PAM and DMT using a 1310 nm silicon photonics intensity modulator for four fiber lengths. DMT achieves 120 Gb/s at 2 km and 110 Gb/s at 10 km, below the *forward error correction* (FEC) threshold of 3.8e-3.

2.3 Introduction

From chapter 1 we know that the exponential growth in network capacity demand due to high quality video streaming and cloud services drives emerging IEEE standardization of 400 GbE [6]. Data centers focus on short range with extremely low cost components, such as silicon photonics technology and direct detection receivers. Two popular choices meeting these constraints are PAM and DMT. DMT is a version of orthogonal frequency division multiplexing (OFDM) in which water-filling techniques maximize transmission capacity by allocation of optimal power and modulation order for each subcarrier as a function of subcarrier SNR. PAM signaling maximizes transmission capacity using equalization techniques at the transmitter and receiver.

Recently various demonstrations have achieved 400 Gb/s short reach data transmission, using PAM [7] and DMT [8]. Comparisons of these two modulation formats have been reported: a theoretical comparison under clipping noise [9], numerical comparison under different distortions [10] and experimental comparison using a directly modulated laser [11]. Most recent results include experimental study of PAM formats at 1300 nm [12] and DMT at 1550 nm [13] using silicon modulators. PAM measurements were not made by the author of this thesis. We used PAM experimental results from [12] and compared it with our DMT experimental results. Our contribution was identification of system exploitation issues that motivated continued examination of waveband and modulation choices.

Silicon modulators in O-band (1300 nm) provide better performance at lower complexity than C-band (1550 nm) because of the very low level of dispersion. We provide an experimental study of DMT for different number of sub-carriers under different length of propagation using silicon modulator at 1310 nm, using the same experimental conditions as PAM studied in [12]. To the best of our knowledge, this is the first comparison between PAM and DMT with silicon modulator at 1310 nm and also the first demonstration of DMT transmission of more than 120 Gb/s using silicon modulator in the O-band.

2.4 Experimental Setup

Fig. 2.1 illustrates the experimental setup, and the block diagram of offline digital signal processing (DSP). Digital data is generated during offline DSP using a pseudo-random bit sequence (PRBS) of length $2^{21} - 1$, which is converted to an analog signal using an 8-bit digital to analog converter (DAC), and framed to the 2^{18} bit DAC memory. The DAC has an analog 3 dB bandwidth of 15 GHz. The DAC ac-coupled output port is connected to the differential input of an Inphi IN3214SZ linear driver. The amplified radio frequency (RF) signal is input to the SiP intensity modulator. The modulator is described in [7], [12] and features a series push-pull configuration; we operate at the quadrature point of the optical transfer function. Fig. 2.2 shows the frequency response of the SiP modulator chip alone and

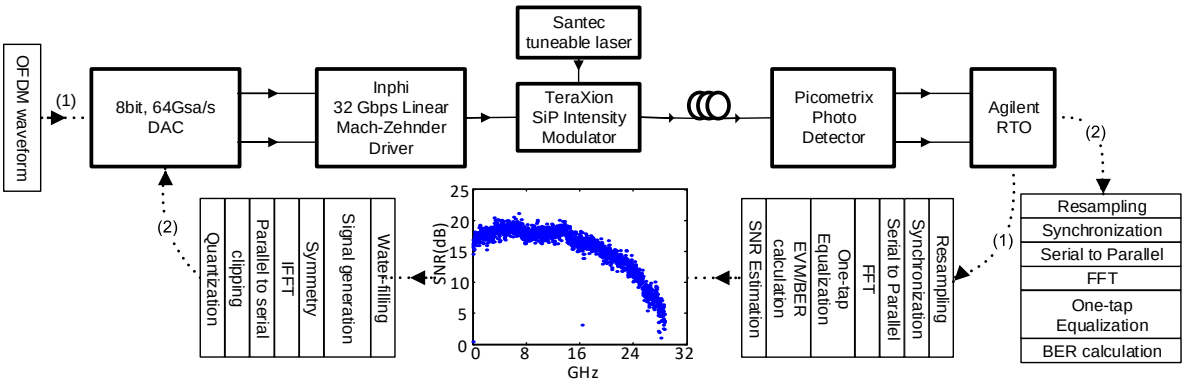

Figure 2.1 – Experimental setup.

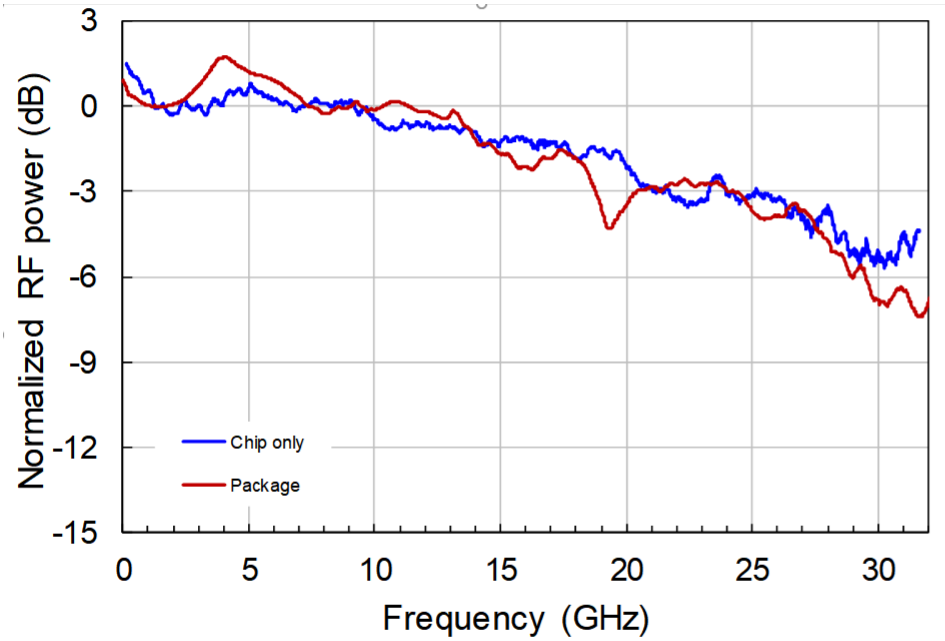

Figure 2.2 – Frequency response of the SiP modulator, chip only in blue and chip after packaging in red.

after packaging (version used here), at a 4 V bias voltage [7], [12].

The 3 dB bandwidth of the modulator is 20 GHz, and it modulates a 20 mW TSL-510 Santec tunable laser tuned to 1310 nm. The modulator output optical signal is launched into four different lengths of SMF-28 (single mode fiber) of 0, 2, 10, and 20 km. In all cases the received optical signal is converted to RF using a PT-40D Picometrix ac-coupled photodiode, with a 3 dB bandwidth of 35 GHz. The received signal power is -3.1 dBm for back-to-back (B2B) and -6.5 dBm (10 km) with the modulator operated at the quadrature point and with a bias of 4 V, mimicking operation in [12]. The signal is captured by an 80 GSample/s Agilent

real time scope (RTO) which has 32 GHz 3 dB bandwidth.

In Fig. 2.1, dotted lines (1) and (2) refer to two measurements sequences. In stage one we transmit QPSK data with uniform power across all sub-channel. This transmission is used to estimate the SNR per sub-channel. The SNR estimate is used in the second measurement sequence to determine the DMT waveform for transmission. [14]

Transmitter-side DSP begins by generating PRBS data and distributing it among sub-channel according to the number of bits to be carried by each sub-channel. In stage one, 2 bits are used for each sub-channel (quadrature amplitude modulation (QPSK)); in stage two the DMT bit mapping determines the number of bits (QAM order) used by each sub-channel. These bits are mapped to the appropriate symbol constellation and goes through a symmetry block to assure Hermitian symmetry among the sub-channel. The frequency domain data is then converted to a time domain signal by taking the inverse fast Fourier transform (IFFT). Because of almost zero dispersion in our frequency range, we do not add any cyclic prefix and proceed directly to the parallel-to-serial (P/S) block. In the next step, to avoid very high PAPR, data is clipped to limit the PAPR to 10 dB. Finally clipped data is quantized over 8-bit and uploaded to the DAC.

During the second stage, we calculate bit and power allocation per sub-channel using Chow's water-filling technique [14] with knowledge of the estimated SNR and a target bit error rate of 10^{-3}. These calculations are made for each sweep of 1) fiber length, 2) subcarrier number, and 3) targeted bit rate. Fig. 3 shows the estimated SNR curve, and the resulting bit allocation and power allocation for B2B case with 2048 subcarriers, and a bit rate of 120 Gb/s.

At the receiver side, the differential outputs of the ac-coupled photodetector are captured by two 80 GSample/s RTO ports. After off-line subtraction of the two signals, data is resampled to 64 GSample/s and synchronized to identify the start of the known transmit data sequence. After a serial-to-parallel (S/P) block, the time domain data is converted to frequency domain data using an fast Fourier transform (FFT). Channel equalization using a frequency domain one-tap equalizer and constellation de-mapping are performed. For stage one measurements, following QPSK detection, both SER and error vector magnitude (EVM) are calculated. The SNR for each subchannel is estimated using SER or EVM, the selection is determined by the accuracy of each measurement. High SNR leads to a more accurate EVM (virtually error-free), while low SNR has more accurate BER (many counted errors); the cut-off occurs at SNR $\approx$7 dB. More details of SNR estimation is provided in appendix A. For stage two measurements, the detector uses the decision thresholds appropriate to each subcarrier QAM level. Only BER is computed. All other manipulations remain unchanged.

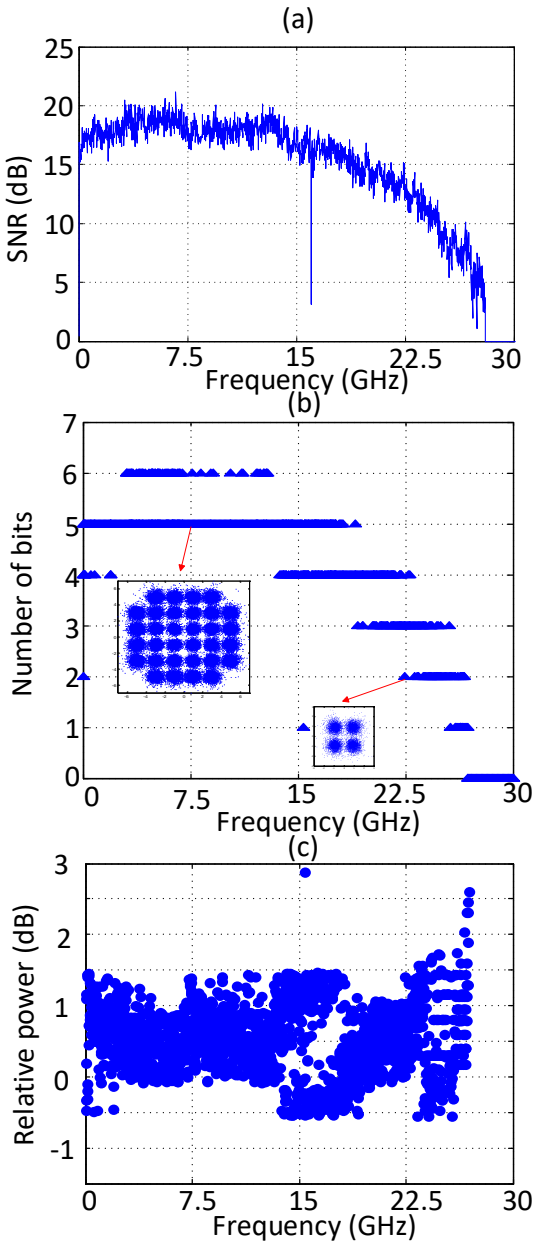

Figure 2.3 – Results for 2048 subcarriers, B2B transmission and 120 Gb/s: (a) stage one SNR estimates, and stage two (b) bit allocation and (c) power allocation. Insets in (b) show typical signal constellations at reception.

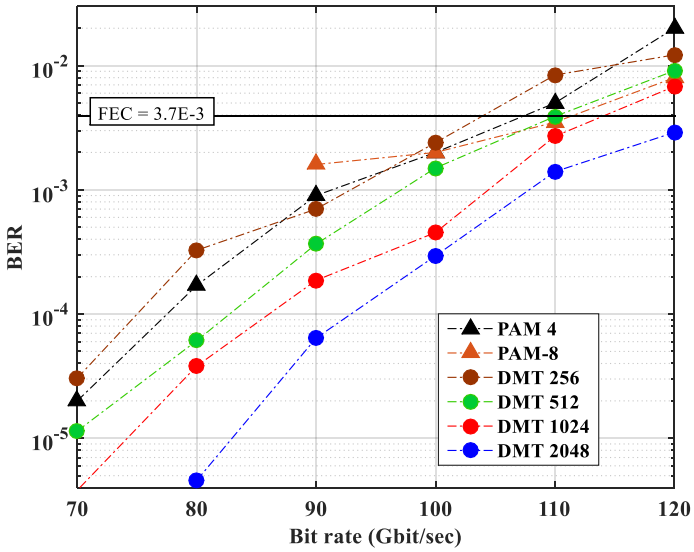

Figure 2.4 – BER performance vs. bit rate for PAM and DMT, back-to-back.

2.5 Results and Discussion

Fig. 2.4 shows the BER measurements for B2B using four different FFT sizes, i.e., number of subcarriers. Larger subcarrier size leads to better DMT optimization, but adds complexity to transmitter and receiver. For comparison we also plot the BTB PAM4 and B2B PAM8 results from [12], retaining only PAM8 at high bit rates where PAM8 outperformed PAM4. The results show that, as expected, larger FFT size in DMT has better performance as the SNR within the small subchannel is more uniform (meaning more optimal allocations), which in turn leads to less inter carrier interference. At 120 Gb/s, 2048 subcarriers are required to remain under the FEC limit. At 110 Gb/s this can be relaxed to 512 subcarriers. Comparing DMT and PAM, DMT performance is always better than PAM in the case of B2B for 512 subcarriers and higher. The 256 subcarrier DMT has comparable performance to PAM4.

Fig. 2.5 shows the comparison between DMT-2048 and PAM4 in the case of different propagation distances. PAM4 remains virtually unchanged to 10 km, but deteriorates at 20 km. DMT has no degradation at 2 km, and at 10 km, DMT still outperforms PAM4. At 20 km, we can see PAM4 performs best, but both are limited to sub 100 Gb/s rates.

2.6 Conclusion

Performance of DMT is compared with PAM using a SiP intensity modulator at 1310 nm. We report bit rates of 120 Gb/s over 2 km and 110 Gb/s over 10 km, remaining below the hard-decision FEC threshold of 3.7e-3 [14].

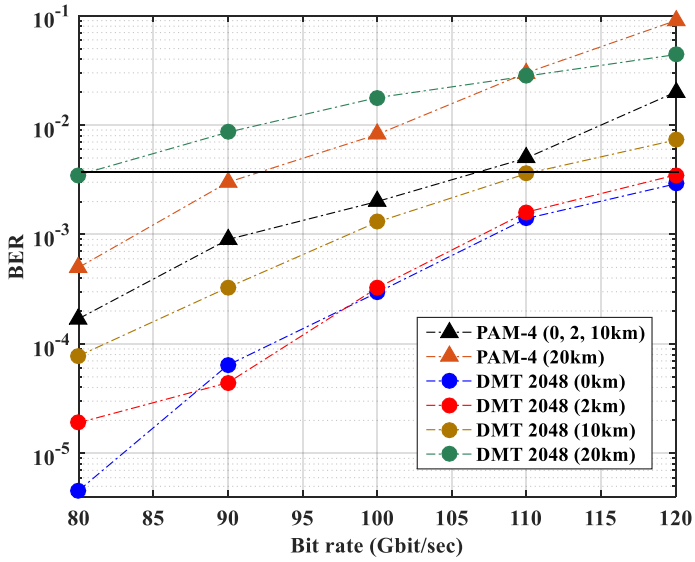

Figure 2.5 – BER performance vs. bit rate for PAM in [12] and DMT for various fiber lengths.

Chapter 3

Analytical Study of Optical SSB-DMT with IMDD

3.1 Résumé

Nous étudions théoriquement les performances du SSB-DMT dans la bande C avec IMDD. Notre analyse nous permet de quantifier l'impact de différentes sources de bruit telles que l'interférence de battement de signal à signal, le bruit de phase à amplitude, l'atténuation et la sensibilité du récepteur sur le SSB-DMT. Nos outils analytiques nous permettent également d'optimiser le rapport de puissance signal-porteuse pour maximiser le débit du SSB-DMT. Nous fournissons des équations pour calculer le taux d'erreur de bit alloué au SSB-DMT. Enfin, nous examinons divers paramètres système (largeur de ligne du laser, bande passante du système et longueur de fibre) pour déterminer leur impact sur les performance .

3.2 Abstract

We theoretically study the performance of SSB-DMT in the C-band with IMDD. Our analysis allows us to quantify the impact of different noise sources such as signal-to-signal beating interference, phase-to-amplitude noise, attenuation, and receiver sensitivity on SSB-DMT. Our analytical tools also allow us to optimize the signal-to-carrier power ratio to maximize SSB-DMT throughput. We provide equations to calculate bit error rate of bit allocated SSB-DMT. Finally we examine various system parameters (laser linewidth, overall system 3 dB bandwidth (combined electrical and optical bandwidth), and fiber length) to determine their impact on the performance of zero guard band SSB-DMT.

3.3 Introduction

High speed video streaming, social networking, and cloud services are driving 400 GbE standardization. Data centers ($\leq$10 km) and passive optical networks ($\leq$40 km) will require 400 Gb/s transmission at low complexity and cost. DMT, because of its high throughput and compatibility with IMDD, is one of the most promising modulation schemes for these short reach applications.

Recently various experimental demonstrations have witnessed more than 100 Gb/s data transmission with DMT, such as our previous work on an O-band SiP modulator at 120 Gb/s [1], 130 Gb/s DMT transmission using SiP modulator in the C-band (1550 nm) [13], etc. In this paper we provide tools to predict the performance of DMT in different system parameters (laser linewidth, fiber length, bandwidth, and signal-to-carrier power ratio). We focus on SSB-DMT in the C-band however, our analysis could be also used for DMT in the O-band.

C-band has nonzero chromatic dispersion in single mode fiber (SMF), which causes inter-symbol interference (ISI) and power fading. Power fading can be bypassed for DMT when using single sideband (SSB) modulation. Both our analysis and simulation assumes ideal SSB-DMT. SSB-DMT can be created by filtering one sideband or via dual drive Mach-Zehnder modulator (DDMZM) [15]; the second choice suffers no distortion from non-ideal filtering.

When chromatic dispersion in C-band combines with phase noise in the optical source (especially when using low cost, large linewidth lasers) other noise sources are introduced to SSB-DMT, such as inter-carrier interference (ICI), phase rotation (PR), and P2A noise. Our semi-analytical model for DMT performance in the C-band takes all these noise sources into account.

The effect of phase noise combined with fiber chromatic dispersion was studied previously for uniform SSB-DMT with the assumption of zero padding half of the sub-carriers to avoid generation of SSBI [16]. This assumption eases analysis, but cuts the achievable transmission rate by half. To achieve more spectral efficiency, we assume zero guard band. There are many SSBI compensation techniques. One example is the Krames-Kronig method and 4x oversampling [17,18], or using receiver-based two-stage linearization filter [19], or other DSP based methods in [20–22]. Hardware cancellation techniques based on balanced receivers [23,24] can be used in the optical domain. Such techniques increase complexity, thus we focus instead on mitigating SSBI by controlling signal-to-carrier power ratio (SCR or γ^2).

P2A noise has been studied before for the case of on-off keying (OOK) modulation [25], however, to the best of our knowledge there is no study of its effect on DMT. We examine the relative importance of P2A and SSBI to overall performance as SCR varies. Increasing SCR decreases SSBI but at the same time it increases P2A noise, making it non-negligible.

This paper starts with a mathematical model of DMT in section 3.4, where all noise

contributions in DMT are identified. In section 3.4.1 the DMT noise sources are studied in detail to estimate SNR per subchannel in the presence of laser phase noise and chromatic dispersion. The estimate of cumulative (from all noise sources) SNR per subchannel is compared with SNR per subchannel prediction from Monte Carlo simulation with good agreement. In section 3.5, results from section 3.4.1 are used to find the SCR yielding an SNR distribution per subchannel leading to optimal DMT performance. The optimal DMT operating point (i.e. the best SCR) is used in section 3.7, where we demonstrate the performance of DMT in different system parameters. Finally, some concluding remarks are made.

3.4 System Model for SSB-DMT

In this paper we use the model in [16] for our single-polarization, uniform SSB-DMT signal. Our only modification is removing the frequency gap between signal and carrier (i.e., we set $N_d = N$ where N_d is the number of data carrying subchannels in [16]), allowing us to study the SSBI effect. The launched SSB-DMT signal in the time domain is

$$s_{DMT}(t) = A_c e^{j2\pi(f_c)t + j\Phi(t)} \left(1 + \gamma \sum_{k=1}^{N} p_k d_k e^{(j2\pi k\Delta f)t}\right), \tag{3.1}$$

where $s_{DMT}(t)$ is the DMT signal in time domain, A_c is the carrier amplitude, f_c is the carrier frequency, γ^2 is the SCR, p_k and d_k are the allocated power and normalized complex amplitude of the k^{th} subchannel, respectively, N is the number of subchannels, and Δf is the subchannel frequency spacing. Laser phase noise, $\Phi(t)$, with linewidth of $\Delta\nu$, is modeled by a Wiener process. Let

$$T_k = [cDLk\Delta f / f_c^2] \tag{3.2}$$

be the time delay or the walk-off for the k^{th} subchannel, in which D is dispersion, L is fiber length, and c is the speed of light in a vacuum. Fiber chromatic dispersion is modeled in the time domain by a delta function $\delta(t - T_k)$, applicable to a single subchannel.

Taking into account laser phase noise and fiber chromatic dispersion, the received signal modulating the optical carrier ($e^{j2\pi f_c t}$), can be modeled as

$$\begin{aligned} r(t) = &\sum_{k=-\infty}^{\infty} A_c e^{j\Phi(t)} * \delta(t - T_k) \\ &+ A_c e^{j\Phi(t)} \gamma \sum_{k=1}^{N} p_k d_k e^{j2\pi k\Delta f t} * \delta(t - T_k) \end{aligned} \tag{3.3}$$

The first term is the impact of fiber dispersion on carrier phase noise, which will create P2A noise after square-law photo detection. This has been studied previously for OOK in [25]. In section 3.4.2 we extend that previous OOK study to the uniform SSB-DMT case.

By assuming that the laser linewidth is smaller than the frequency spacing of one subchannel, the second term of (3.3) can be approximated by

$$\begin{aligned} & A_c e^{j\Phi(t)} \gamma \sum_{k=1}^{N} p_k d_k e^{j2\pi k \Delta f t} * \delta(t - T_k) \\ \approx\ & A_c \gamma \sum_{k=1}^{N} p_k d_k e^{j2\pi k \Delta f (t-T_k) + j\Phi(t-T_k)}, \end{aligned} \tag{3.4}$$

This assumption is reasonable even for the worst case we examine where the overall frequency occupation is more than 10 GHz, the number of subchannels is $N = 512$, hence $\Delta f \geq 19.5$ MHz, and our laser linewidth $\Delta\nu$ is less then 2 MHz.

After square-law photodetection, the output signal is

$$\begin{aligned} & \left(2P_c \mathrm{Re}\left[\gamma \sum_{k=1}^{N} p_k d_k e^{j2\pi k \Delta f t + j\rho_k(t) + j\theta_k} \right] \right. \\ & \left. + \left[P_c \gamma^2 \sum_{k=1}^{N} |p_k . d_k|^2 \right] + P2A + SSBI \right), \end{aligned} \tag{3.5}$$

where $P_c = |A_c|^2$ is carrier power, $\rho_k(t) = [\Phi(t - T_k) - \Phi(t)]$ is phase fluctuation on kth subchannel, and $\theta_k = -2\pi k \Delta f T_k$. The first term in (3.5) is the SSB-DMT signal distorted by ICI, PR, and power degradation. The second term is a direct current (DC) offset.

The third term in (3.5), as mentioned earlier, is the carrier self-interference which we call P2A noise, this term can be expressed as

$$\begin{aligned} P2A = A_c^2 \sum_{k=-\infty}^{\infty} \sum_{j=-\infty}^{\infty} & e^{j\Phi(t)} * \delta(t - T_k) \times \\ & e^{j\Phi(t)} * \delta(t - T_j). \end{aligned} \tag{3.6}$$

We analyze P2A noise in section 3.4.2. The last term in (3.5) is the signal self-interference in the form of SSBI which is created by subchannels beating against one another, and we analyze this contribution in section 3.4.3 The SSBI term is not affected by phase noise or chromatic dispersion. Note that P2A was neglected in previous works with zero padding of half the available subchannels where systems operate in the high SCR regime. We will see in the next section that without that assumption, P2A noise can dominate for low signal-to-carrier power ratios.

3.4.1 Validation of Theoretical SNR Prediction

In this section we estimate SNR per subchannel of uniform SSB-DMT ($p_k = 1$) and validate our results via Monte Carlo simulation. The SNR estimates are the basis for determining non-uniform DMT performance using water-filling techniques in section 3.5 and 3.6.

In appendix B we describe a numerical simulation model for estimating SNR per subchannel using Monte Carlo techniques. By its nature, the SNR estimates include the cumulative effect of all noise sources. Figures in this section include Monte Carlo results (cumulative effect of noise) and analytical results (contribution of each independent noise).

In this section we individually analyze each noise contribution in turn. For different signal-to-carrier ratios, the relative importance of each noise source varies. We examine several SCR regimes where different noises dominate.

Analysis in [25] found an expression for P2A noise power spectral density (PSD), which was used to find P2A noise for OOK. In Section 3.4.2 we find P2A noise power for SSB-DMT using this P2A PSD. Section 3.4.3 presents new analysis of SSBI noise. Section 3.4.4 recalls results from [16] on the interaction dispersion with phase noise. Section 3.4.5 combines results from previous subsections into a prediction of overall SNR.

3.4.2 Phase to Amplitude Noise

In (3.5) the P2A degradation depends on the carrier, not the signal. The binary OOK signal analysis of P2A noise [25] is extended here to DMT signals, to the best of our knowledge for the first time. As in [25], we use a Bessel expansion of the electrical field and neglect contributions from the higher order terms. The power spectral density of P2A noise is

$$PSD_{P2A}(f) \approx \frac{1}{2}\left[\sum_{n=0}^{\infty} 4J_n\left(\frac{1}{f}\sqrt{\frac{2\Delta\nu}{\pi}}\right) J_{n+1}\left(\frac{1}{f}\sqrt{\frac{2\Delta\nu}{\pi}}\right) \times \sin\left\{\frac{1}{2}(2n+1)(2\pi f)^2 k'' L\right\}\right]^2, \tag{3.7}$$

where J_n is the n^{th} order Bessel function of the first kind, L is the fiber length, and $k'' = \frac{\lambda^2}{2\pi c}D$, where c is the speed of light. The P2A noise power is the product of the carrier power and P2A PSD.

To calculate SNR for the k^{th} subchannel we find subchannel noise power $\sigma^2_{k(P2A)}$ and signal power $\sigma^2_{k(S)}$ by

$$\sigma^2_{k(P2A)} = P_c \int_{(k-1)\Delta f}^{k\Delta f} PSD_{P2A}(f)df, \tag{3.8}$$

$$\sigma^2_{k(S)} = \frac{P_s}{N_s} = \frac{\gamma^2 P_c}{N_s}, \tag{3.9}$$

where N_s is the number of subchannels with data, P_s is the overall signal power, and γ^2 is the signal-to-carrier power ratio. Finally, the SNR per subchannel for P2A noise is

$$SNR_{k(P2A)} = \frac{\sigma^2_{k(S)}}{\sigma^2_{k(P2A)}}. \tag{3.10}$$

To validate (3.10), we vary SCR and compare Monte Carlo (MC) simulations of SNR per subchannel (see appendix B) with theoretical predictions from (3.10). Results are presented in Fig. 3.1 for fiber length of 20 km, with overall signal frequency occupation of 32 GHz, and laser linewidth of 100 kHz. Two abscissa axes are provided, the lower one for subchannel number, and the upper one for frequency. The MC simulation (solid lines) take into account all noise sources.

In Fig. 3.1a we vary SCR γ^2 from -30.5 dB to -22.5 dB; theoretical results (dotted lines) include only P2A noise. For low SCR, P2A-only theory matches the all-noise simulation (solid lines). However, as the signal-to-carrier power ratio increases, the two begin to diverge. We conclude that at low SCR the P2A noise dominates, but other noise sources take over as the signal power grows. We next examine those other noise sources.

3.4.3 Signal-to-Signal Beating Interference (SSBI)

The last term in (3.5), SSBI, shows the effect of subchannels beating against one another instead of the carrier. This effect can be calculated as

$$\sigma^2_{k(SSBI)} = \frac{1}{P_c} \sum_{n=-N}^{N} \sigma^2_{n(S)} \sigma^2_{k-n(S)}, \tag{3.11}$$

more details for (3.11) are provided in appendix C. The SNR per subchannel is calculated by

$$SNR_{k(SSBI)} = \frac{\sigma^2_{k(S)}}{\sigma^2_{k(SSBI)}}. \tag{3.12}$$

As γ^2 grows, so does the signal power $\sigma^2_{k(S)}$, and SSBI as well. From (3.10), increasing SCR γ^2 leads to lower $SNR_{k(P2A)}$, leading to SSBI to dominate after a threshold value for signal-to-carrier power ratio.

In Fig. 3.1b we vary γ^2 from -22.5 dB to -13 dB, and theoretical results from (3.12) (dotted lines) include only SSBI noise. Comparing all-noise Monte Carlo simulation and SSBI-only theory we see that for SCR greater than -16 dB, SSBI is the dominant noise source.Parameter γ^2 affects both P2A and SSBI, but in opposite ways.

3.4.4 Interaction of dispersion with phase noise

In (3.5), the first term describes the interaction of dispersion with phase noise. This interaction leads to these effects: 1) power degradation α, 2) ICI, and 3) PR. These degradations were studied in uniform SSB-DMT where half the subchannels (those near the carrier) were used as a guard band to eliminate SSBI [16]. Using this results with zero guard band ($N_d = 0$), the power degradation of the k^{th} subchannel due to phase noise is

$$\alpha_k \approx 1 - 2\pi\Delta\nu T_k = 1 - \beta_k, \tag{3.13}$$

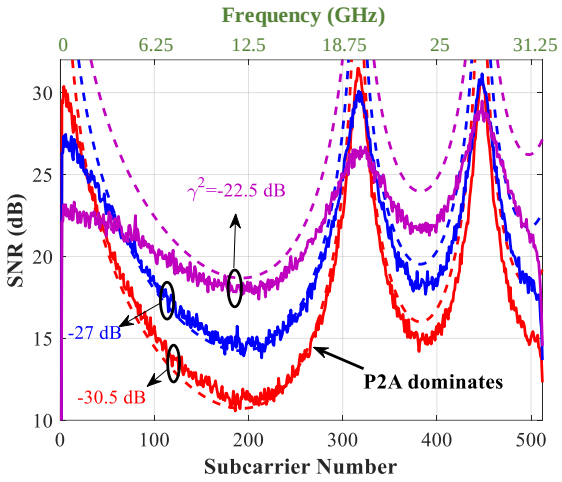

(a)

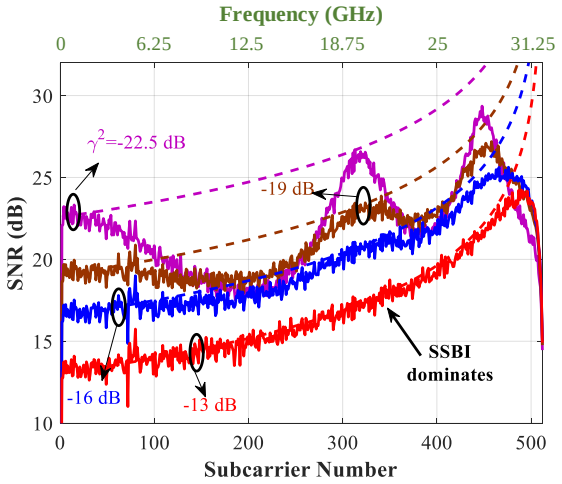

(b)

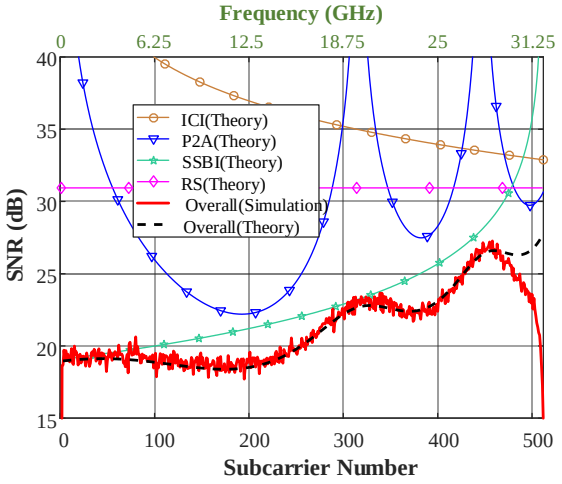

(c)

Figure 3.1 – SNR per subchannel is found for 20 km of fiber, overall signal frequency occupation of 32 GHz, and 100 kHz laser linewidth. Monte Carlo simulation of all noise sources is shown in solid lines, theoretical SNR predictions are shown in (a) for P2A only (dashed) for three values of γ^2; (b) for SSBI only (dashed) for three values of γ^2; and (c) for $\gamma^2 = -23$ dB for each noise source separately (see markers), and all noise sources (black dotted).

where $\beta_k = 2\pi\Delta\nu T_k$ is the phase noise power in the k^{th} subchannel.

The variance of the ICI for k^{th} subchannel is

$$\sigma^2_{k(ICI)} \approx \frac{\beta_k}{N^2}\left(N^2 + \frac{1}{3}M_k^2 - NM_k - \frac{1}{3}\right), \tag{3.14}$$

where T_s is the sampling interval of the DAC and $M_k = T_k/T_s$ is the delay relative to the carrier (in number of samples) for the k^{th} subchannel.

The PR variance for the k^{th} subchannel is

$$\sigma^2_{k(PR)} \approx \frac{\beta_k}{3N^2}\left(-M_k^2 + 3NM_k + 1\right), \tag{3.15}$$

The PR variance is essential in the calculation of symbol error rate from estimated SNR described in appendix D. However, the impact of PR on the subchannel SNR itself is negligible as the sum of ICI and PR variances is dominated by the ICI variance. To see this, we note that the ratio of PR variance to ICI variance decreases with increasing fiber length or decreasing FFT size. For 50 km fiber and typical FFT size of 1024, that ratio is less than -32 dB. This small value justifies writing the SNR per subchannel for the first term of (3.5) as

$$SNR_{k(ICI)} = \frac{\alpha_k}{\sigma^2_{k(ICI)} + \sigma^2_{k(PR)}} \approx \frac{\alpha_k}{\sigma^2_{k(ICI)}}. \tag{3.16}$$

3.4.5 Overall SNR

In this section we combine the effect of all noise sources using superposition law as

$$\begin{aligned}\frac{1}{SNR_k} =& \frac{1}{SNR_{k(ICI)}} + \frac{1}{SNR_{k(P2A)}} \\ &+ \frac{1}{SNR_{k(SSBI)}}. + \frac{1}{SNR_{k(RS)}},\end{aligned} \tag{3.17}$$

where $SNR_{k(RS)}$ captures the effect of receiver sensitivity (RS) and is a white process with the same noise power for all subchannels. In (3.17) we assumed that the effects of different noise sources on each other are negligible and that they may be considered independent. A final simulation was run to validate this assumption.

Figure 3.1c shows the SNR from each noise source separately: ICI with circle markers, P2A with triangles, SSBI with stars and RS with diamonds. The dashed line is the total SNR predicted by (3.17). As can be seen, the theoretical total SNR matches well the MC simulated SNR per subchannel. In the case of bandlimited channel, the overall SNR per subchannel would, of course, also be affected by the channel frequency response.

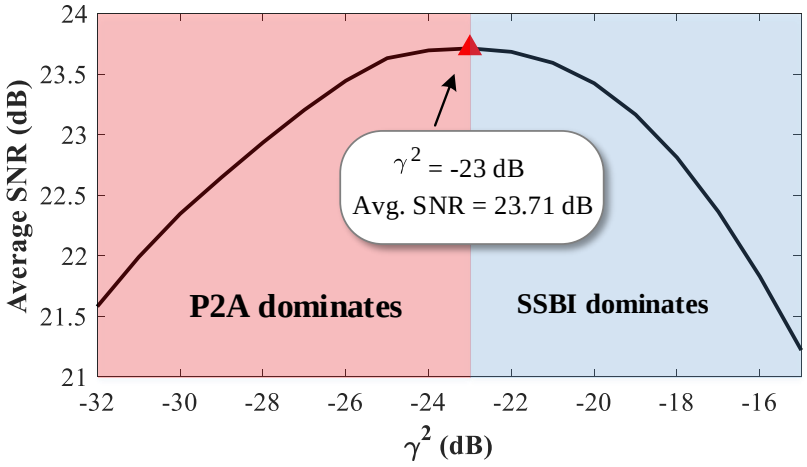

Figure 3.2 – Average SNR over subchannels for different values of γ^2.

3.5 Optimal SCR for DMT

The performance of DMT is determined by the SNR distribution per subchannel, which is influenced by the SCR. To justly comparing PAM and DMT, we use our SNR prediction per subchannel to select the most beneficial operating point for DMT, that is, the optimal signal-to-carrier ratio γ^2. BER is the most appropriate optimality criterion, but requires excessive calculation and results will vary depending on the DMT bit and power allocation algorithm used. We compare SCR minimizing BER under Chow's algorithm with SCR maximizing the average SNR. We will find that optimal SCR under the two criteria are very close (within ~ 1 dB).

3.5.1 SNR averaged over subchannels

From the total SNR per subchannel, the SNR averaged over subchannels can be found as a function of SCR. Figure 3.2 plots average SNR versus SCR. Once again, results are for fiber length of 20 km and laser linewidth of 100 kHz, but no bandwidth limit. This figure shows that for $\gamma^2 < -23$ dB P2A noise dominates, while above that threshold, SSBI dominates. For Fig. 3.2, receiver sensitivity was an AWGN with $SNR_{RS(B2B)} = 35$ dB to focus on other degradation sources. However, in subsequent estimations we use a more practical value typical for photodetection; $SNR_{RS(B2B)} = 22$ dB for the balance of the paper.

We next systematically examine the three system parameters that affect the SNR averaged over subchannels: laser linewidth, fiber length and system bandwidth. The average SNR in dB (a 2D color map) as a function of γ^2 over the range -38 dB to -3 dB is found for each parameter in turn in three plots.

Figure 3.3a shows average SNR for linewidth from 100 kHz to 2 MHz. For this plot the

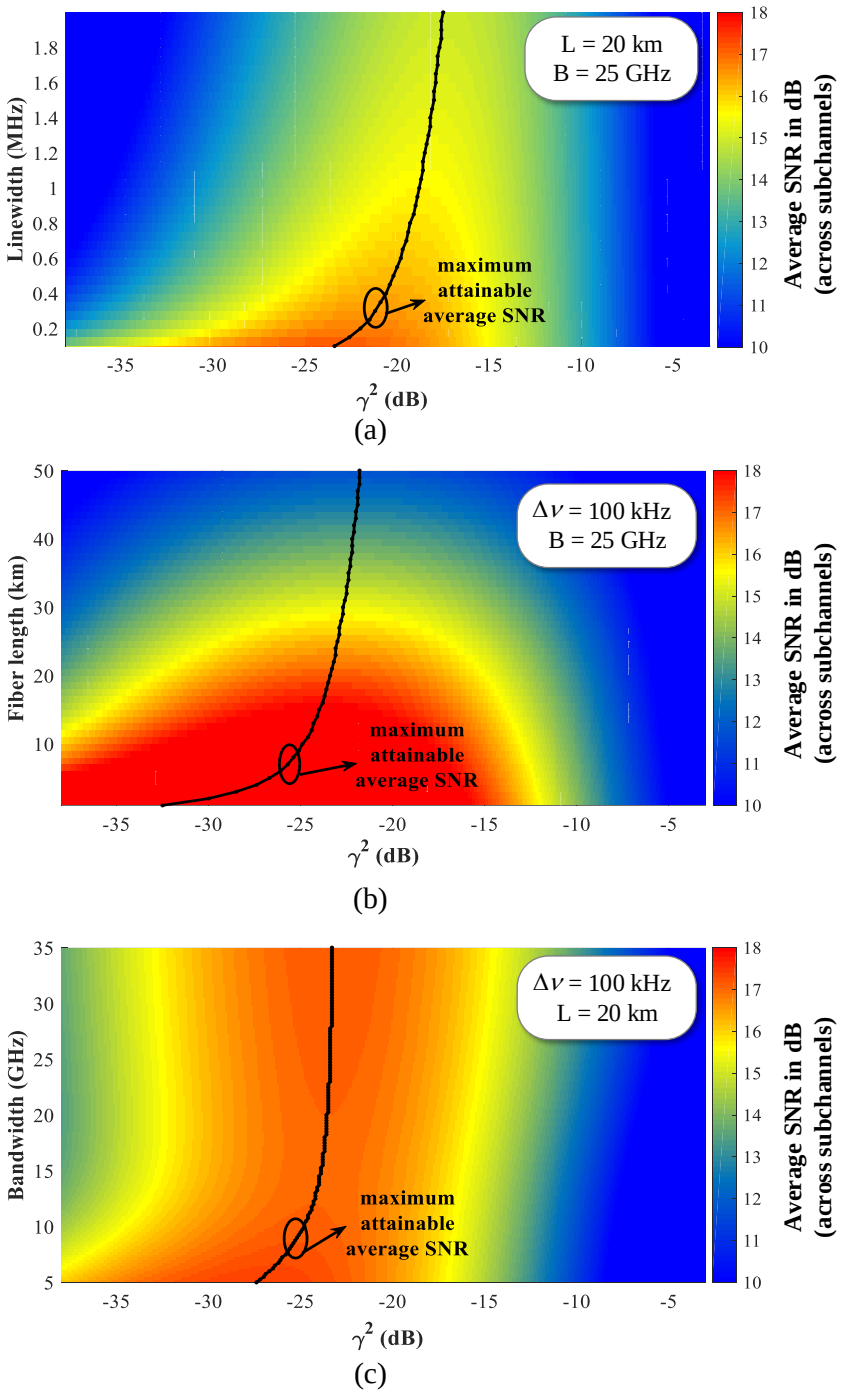

Figure 3.3 – Average SNR in dB for different values of γ^2 and different values of a) laser linewidth, b) fiber length, and c) channel bandwidth. Black curves show the maximum attainable average SNR in each case.

fiber length is 20 km and overall system 3 dB bandwidth is 25 GHz. The black line traces the optimum SCR as a function of linewidth, ranging from -23 dB for narrow linewidth to -18 dB at 2 MHz linewidth.

Figure 3.3b holds linewidth at 100 kHz and system overall 3-dB bandwidth at 25 GHz, and varies fiber length from 0 km (B2B) to 50 km. Again, optimum SCR is traced in the black line, ranging from -33 dB for B2B to -23 dB at 50 km.

Finally, Fig. 3.3c holds fiber length to 20 km and linewidth to 100 kHz, and examines system bandwidth. As bandwidth changes from 5 GHz to 35 GHz the optimum value for signal-to-carrier power ratio ranges from -27 dB to -23 dB. Comparing the three plots in Fig. 3.3, average SNR and optimum SCR is more sensitive to fiber length than linewidth or bandwidth.

3.5.2 DMT BER calculation

We calculate DMT performance using the theoretical estimation of SNR per subchannel from the previous sections for a given linewidth $\Delta\nu$, fiber length L and system bandwidth B. This SNR per subchannel is used to find the bit and power allocation for DMT using Chow's margin adaptive algorithm [14]. This water-filling algorithm starts with bit allocation (for the given SNR per subchannel) to achieve a target bit rate. The second step is calculating the required power allocation for each subchannel to achieve a target BER with the bit allocation. Certain combinations of bit rate and bit error rate will be achievable for a given SNR distribution, while others will not. Note that Chow's algorithm uses a strict Gaussian noise assumption to determine the bit and power allocations.

Once the bit and power allocations are determined, we calculate the overall BER using equations developed in appendix D that include phase rotation effects (not considered in Chow's algorithm). For a given subchannel, the bit allocation determines the MQAM constellation used, and (3.17) gives the SNR for the additive white Gaussian noise. The PR is a non-additive Gaussian noise. The symbol error rate (SER) can be found when conditioned on the PR, and then averaging over the PR probability density function. The SER calculation is based on each QAM constellation point falling into one of three categories, depending on its number of nearest neighbors. We find the SER for each category, and then the total SER in the presence of AWGN and PR. Finally, we assume Grey coding to find the BER.

3.5.3 DMT Optimization

Using this technique for BER calculation we can sweep SCR and find the optimum SCR that minimizes BER. We compare the optimum SCR when minimizing BER vs. maximizing average SNR in Fig. 3.4. The SCR maximizing average SNR is given by a black dashed line. As the BER will vary with bit rate, we examine three rates: 80, 100 and 120 Gb/s

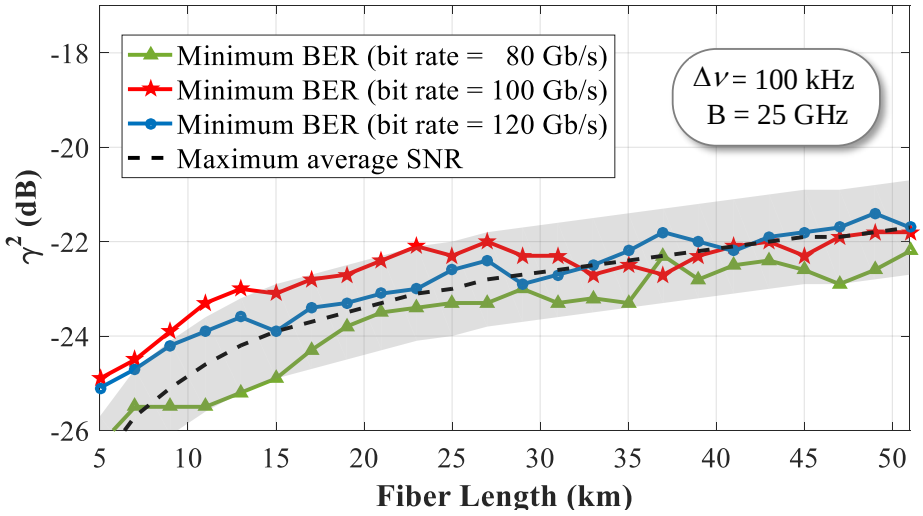

Figure 3.4 – Optimized γ^2 which maximizes average SNR (dotted line) and when it minimizes BER for three different bit rates 80, 100, and 120 Gb/s (solid lines) versus fiber length.

whose optimal SCR is traced by green, red, and blue solid lines, respectively. The optimum SCR varies with the triplet (L, $\Delta\nu$, B). In Fig. 3.4, fiber length as an example of triplet is swept, while the two others are held constant. The same analysis is done for linewidth and bandwidth. The grey region represents the zone within 1 dB on either side of the curve for SCR maximizing average SNR.

In all cases changing bit rate does not have much effect on the value of optimized SCR, i.e., the curves are clustered in all plots. We also observe that SCR for minimum BER falls within or very close to the gray region. That is, that the two optimality criteria result in an optimal SCR that is similar (to within ~ 1 dB). Optimizing signal-to-carrier power ratio by maximizing average SNR is much less compute intensive than minimizing BER. In the next section, DMT performance is found with SCR optimized for maximum average SNR.

3.6 Impact of System Parameters on SSB-DMT

In this section we use our analytical tool to study the performance of SSB-DMT in a variety of operational constraints examining the triplet of fiber length, linewidth, and channel bandwidth (L, $\Delta\nu$, B), as well as the bit rate.

3.6.1 Impact of Fiber Length and Linewidth

We study the joint effect of fiber length and laser linewidth on SSB-DMT. Figure 3.5 shows via color map, the logarithm of SSB-DMT BER for fiber length 10 to 45 km and linewidth from 0.1 to 2 MHz. Bandwidth is held at 25 GHz and the bit rate is 100 Gb/s. The ordered pairs of fiber length and laser linewidth leading to BER $= 3.8 \times 10^{-3}$ are given in the black

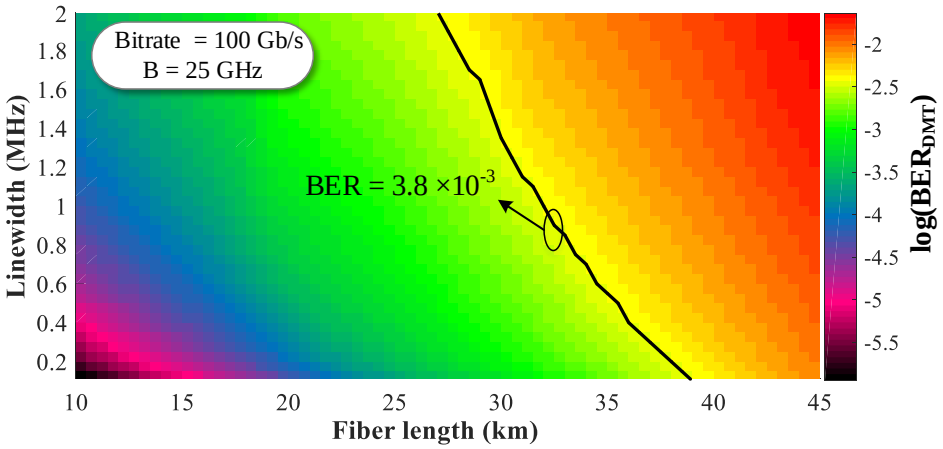

Figure 3.5 – BER of SSB-DMT for different laser linewidth and fiber length (Channel bandwidth = 25 GHz).

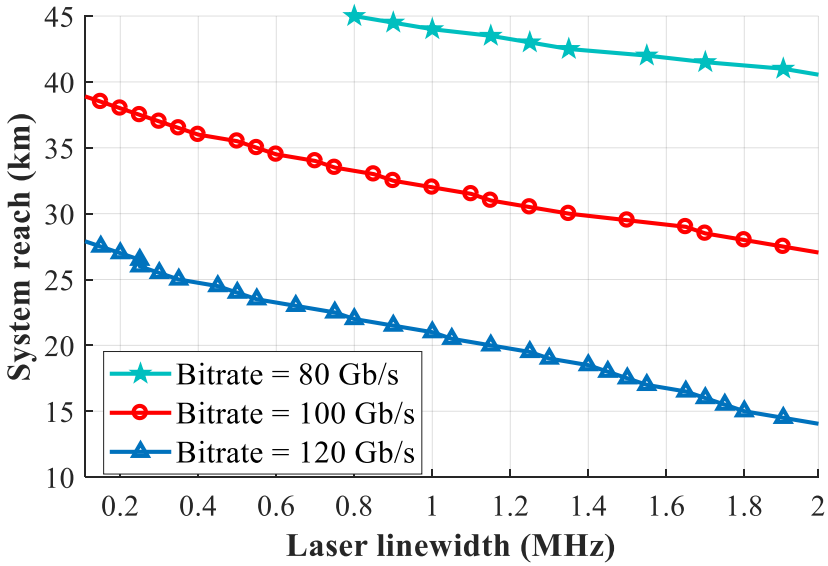

Figure 3.6 – System reach at BER = 3.8×10^{-3} of SSB-DMT for different laser linewidth.

line. This figure shows that the system reach (maximum fiber length with BER under FEC threshold) for the case of a costly, high quality laser with linewidth of 100 kHz is almost 40 km; with a lower quality laser with linewidth of 2 MHz, we can still achieve 30 km reach.

System reach is also calculated for bit rates of 80, 100, and 120 Gb/s in Fig. 3.6. Increasing bit rate will force the DMT waterfilling technique to choose higher order QAM, which is more sensitive to noise, thus decreasing system reach. This figure shows that the system reach of 80 Gb/s SSB-DMT is always greater than 40 km, even when using a lower cost laser with linewidth of 2 MHz. When increasing the bit rate to 120 Gb/s, system reach is limited to 27 km for the best case of laser linewidth 0.1 MHz.

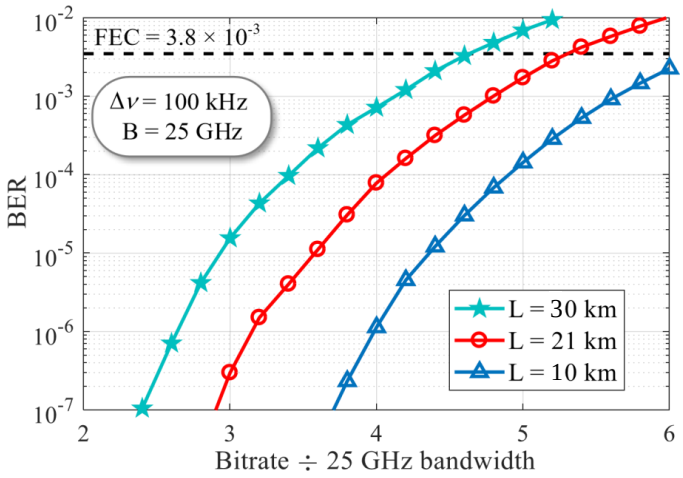

Figure 3.7 – BER versus spectral efficiency. (Channel bandwidth = 25 GHz, and $\Delta\nu$ = 100 kHz).

3.6.2 Impact of Bandwidth Constraints

In this section, we assume a fixed hardware solution limiting the channel bandwidth to 25 GHz, and we vary the bit rate. This bandwidth represents current limits of commercially available integrated coherent receivers. We present BER results as a function of spectral efficiency (the ratio of bit rate to system bandwidth). A lower ratio corresponds to less aggressive bit rates for a given hardware solution, while a higher ratio corresponds to aggressively pushing high bit rates through a restricted bandwidth. We selected the case of 10, 21, and 30 km fiber length and 100 kHz laser linewidth for our performance analysis.

Figure 3.7 shows the BER of SSB-DMT versus spectral efficiency. Fiber length influences several noise terms in the SNR per subchannel, leading to a complex effect on DMT performance. In addition, DMT performance changes markedly as we change bit rates (see spread of each curve in Fig. 3.7). This performance analysis shows that when the fiber length is 10 km the maximum bit rate for BER less than FEC is $4.5 \times 25 = 112.5$ Gb/s; if we increase fiber length to 21 and 30 km, the maximum bit rates with BER under FEC threshold are 130 Gb/s and more than 150 Gb/s, respectively.

3.7 Conclusion

We presented a theoretical analysis to study the performance of SSB-DMT. Such an analysis requires that SSB-DMT be optimized, particularly with respect to the signal to carrier ratio. Our tools allows this optimization. Using our analytical tools, we simulated the impact of hardware-imposed bandwidth limitation on SSB-DMT. Our results can be used to select appropriate hardware (modulators and laser sources), or to quantify attainable bit rates or system reach.

Chapter 4

Interplay of Bit Rate, Linewidth, Bandwidth, and Reach on Optical DMT and PAM with IMDD

4.1 Résumé

Nous comparons théoriquement les performances du DMT et du PAM en utilisant la IMDD. Le PAM est une solution moins coûteuse et moins complexe que le DMT, mais il est plus vulnérable à la dispersion chromatique dans la bande C. Nous comparons DMT et PAM en tenant compte de l'interaction entre la largeur de ligne du laser, la longueur de la fibre, le débit de transmission et la bande passante du canal. Nous utilisons un modèle semi-analytique pour examiner les taux d'erreur sur les bits. Nous étudions comment les paramètres du système modifient les avantages de performance entre DMT et PAM. Alors que diverses démonstrations expérimentales ont montré que le PAM ou le DMT donnent de meilleurs résultats, nous étudions l'origine de la variation dans ces essais rapportés.

4.2 Abstract

We theoretically compare the performance of optical DMT and PAM using IMDD. PAM is a lower cost, lower complexity solution than DMT, however it is more vulnerable to chromatic dispersion on the C band. We compare DMT and PAM taking into consideration the interplay of laser linewidth, fiber length, transmission rate, and channel 3 dB bandwidth (combined electrical and optical bandwidth). We use a semi-analytical model to examine bit error rates. We study how system parameters shift the performance advantages between DMT and PAM. Our model can also be used to find the best hardware solution and frequency band for a target modulation format and bit error rate.

4.3 Introduction

As explained in Chapter 1, high demand for expanded network capacity drives new standardization into 400 Gb/s optical fiber transmission. The main focus of this paper is on short haul applications targeting these speeds, such as data centers ($\leq$10 km) and passive optical networks ($\leq$60 km). PAM and DMT are both compatible with cost-effective direct detection, and are popular choices to reach 400 Gb/s.

While various experimental demonstrations have witnessed PAM or DMT perform best, we probe the origin of the variation in reported trials. For example, experimental demonstrations of 112 Gb/s PAM transmission using a SiP modulator [26], 100 Gb/s Nyquist PAM-4 transmission using an electro-absorptive modulated laser have appeared, both on the O-band (1310 nm) [27], 128 Gb/s PAM-4 transmission system using a multi-electrode silicon photonic Mach Zehnder modulator [28], EML-based 4 lanes of 112.5 Gb/s PAM4 [29], and 112 Gb/s PAM4 Amplifier-free using O-band DML [30]. There are also several reports of DMT transmission over 100 Gb/s, such as our previous work with SiP modulators, where we reached 120 Gb/s on the O-band [1], another SiP modulator achieving 130 Gb/s on C-band (1550 nm) [13], beyond 100 Gb/s transmission of SSB-DMT on O-band [31], 4 channels of 100 Gb/s DMT using O band silicon photonic modulator [32], and 100 Gb/s dual side-band DMT with dispersion compesation on C-band [33].There has also been a hybrid PAM/DMT demonstration at 112 Gb/s using a directly modulated laser on O-band [34].

Several comparisons have been made between PAM and DMT both experimentally and theoretically, such as experimental comparison of PAM versus DMT using an O-band directly modulated laser [35], in this work DMT has better performance compared to PAM and the fiber length is 2.2 km. Analytical comparison between PAM and DMT [9], we used same model for PAM as in this paper but unlike our analysis DMT is double sideband and is modeled in O-band. The main degradation sources for DMT are assumed to be receiver noise and clipping noise. Another example is an experimental comparison between PAM and DMT on O-band up to 10 km propagation distance in [36], in this paper the author also compared the implementation complexity and showed that pulsed shaped PAM requires larger number of complex multipliers to be implemented. Unlike previous comparisons we focus on SSB-DMT on C-band and non-pulse shaped PAM on O-band. Our analysis covers up to 100 km where we can neglect fiber non-linearity.

We can generate single side-band DMT (SSB-DMT) at the transmitter using dual drive Mach Zehnder modulators (DDMZM) [15]. This complex signal contains the same data as a DSB-DMT signal made real with Hermitian symmetry, but occupies half the optical spectrum. We already require a digital-to-analog (DAC) converter for DMT, and the DAC can be exploited for SSB. Note that while the optical spectral efficiency is increased by two compared to DSB-DMT, the required DAC bandwidth (or electrical spectral efficiency) is

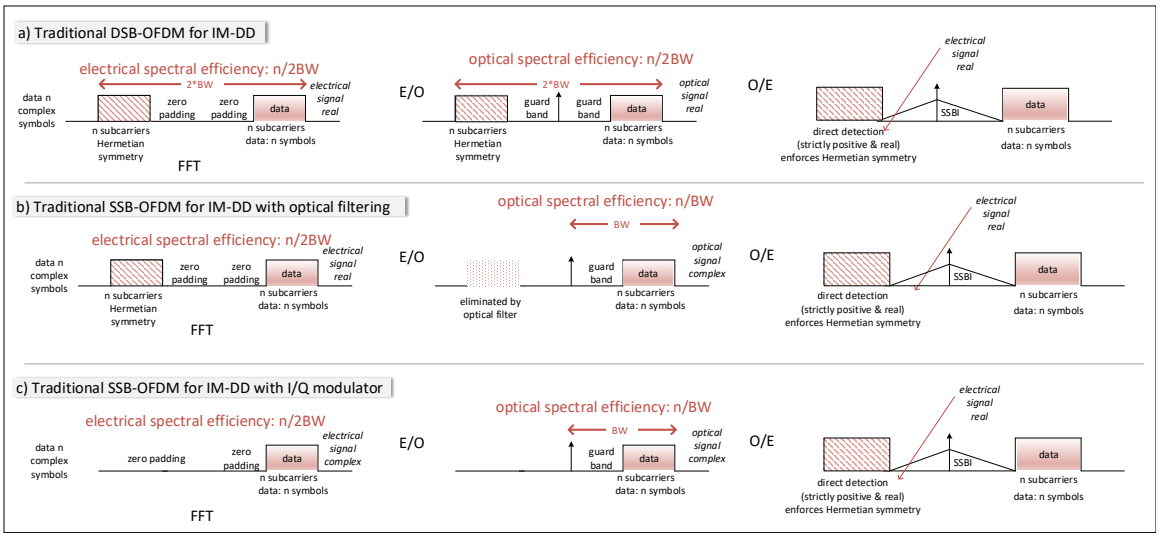

Figure 4.1 – Comparison of a) DSB-OFDM, b) SSB-OFDM with optical filtering, and c) SSB-OFDM with IQ modulator.

unchanged, see Fig. 4.1. The DAC hardware and transmitter DSP is therefore the same for either DSB-DMT or SSB-DMT implementations. PAM, on the other hand, does not require a DAC; PAM would lose much of its low complexity advantage in adopting an SSB implementation. Attenuation on O-band is greater than that on C-band, but on C-band the chromatic dispersion is nonzero. Power fading is the most important degradation caused by chromatic dispersion on single mode fiber (SMF). Therefore, in our comparison we assume that SSB is an option available for DMT and not PAM. In other words, our assumption will lead to PAM suffering from power fading, but not DMT.

Signal to signal beating interference (SSBI) is present in both O-band and C-band and is a major source of impairment for DMT. For O-band modulation, SSBI for SSB-DMT can be mitigated, while on C-band it remains a factor [2]. Therefore, there is a trade-off between attenuation on O-band and dispersion on C-band in comparing DMT with PAM. Depending on the fiber lengths involved, either SSB-DMT on C-band or PAM on O-band may be preferred.

Our analytical study of SSB-DMT on C-band in Chapter 3 shows the effect of P2A, ICI, SSBI, attenuation C-band. Using this analysis we also optimized SSB-DMT in terms of signal-to-carrier power ratio to achieve highest possible throughput in any system condition. In this chapter we use the same analysis for SSB-DMT.

We concede that PAM will typically outperform DMT on the O-band; due to the lower cost of PAM equipment, it is a better choice on O-band. Similarly, DMT will typically outperform PAM on the C-band as overcoming power fading on PAM will lead to excess complexity. Therefore, we focus on the detailed performance comparison of PAM on O-band

and DMT on C-band.

In section 4.4 we provide a mathematical model for SSB-DMT on C-band and PAM on O-band. Section 4.5 introduces equations to calculate BER for PAM and DMT modulation formats, relying on methodology from [2] to optimize DMT performance. Using results from section 4.5, in section 4.6 we expand on [37] to examine the interplay of laser linewidth, fiber length, transmission rate, and channel bandwidth. We offer some concluding remarks in section 4.7.

4.4 System Model

4.4.1 DMT

In this chapter we will examine DMT performance in the C-band. We model the SSB-DMT launched signal as in section 3.4, equation (3.1). Taking into account the chromatic dispersion of fiber in C-band and the laser phase noise, the received signal after photo detection is calculated from equation (3.5).

The SNR per subchannel for each term in (3.5) is calculated separately. Transmitter and/or receiver bandwidth limitations are examined by assuming the overall channel frequency response has a Gaussian shape parameterized by its 3 dB bandwidth. The receiver noise is assumed to be AWGN. Taking the SNR per subchannel, we scale appropriately to have an overall SNR of 22 dB when only receiver noise is present. This same value of SNR is used for PAM and is selected as it represents acceptable performance over a wide range of typical system parameters such as the ratio of bit rate to bandwidth, and the laser linewidth.

4.4.2 O-band PAM

For PAM modulation we assume a rectangular pulse shape $p(t)$, and a Gaussian shaped channel impulse response $h(t)$ whose bandwidth is parameterized by its 3 dB bandwidth (as with DMT analysis). The received PAM signal is

$$s_{PAM}(t) = A_c e^{j2\pi(f_c)t} \left(1 + \sum_n a_n g(t - nT_{sym})\right), \tag{4.1}$$

where $s_{PAM}(t)$ is the PAM signal in the time domain, $g(t) = p(t) * h(t)$, a_n is n^{th} PAM symbol, and T_{sym} is the symbol time. Note that $\{a_n\}$ are scaled to achieve unity power in the multilevel signal. The only distortion on PAM is due to the bandwidth limitation, and the only noise is receiver thermal noise which modeled as additive white Gaussian noise with SNR of 22 dB. Attenuation will cause the SNR to decrease with increasing fiber length. To mitigate ISI caused by a band-limited channel, we assume a proper equalization technique; the overall effect of a band-limited channel with an equalizer will be calculated in the next section.

4.5 BER calculation

In this section at first we define an approach that provides a fair comparison between PAM and SSB-DMT. The second subsection covers BER calculation for SSB-DMT exploiting the knowledge of SNR per subchannel from [2]. Finally BER for O-band PAM with a decision feedback equalizer is calculated.

4.5.1 Comparison Framework

To justly comparing PAM and DMT, we assume the total signal power (P_s) and the receiver noise power spectral density (N_0) for both cases are the same. Equivalently, the ratio of energy per symbol, E_S, to N_0 is the same for both PAM and DMT. The overall DAC bandwidth, BW_{DAC}, will be exploited by SSB-DMT. For DMT, the receiver noise induced SNR, SNR_{RX}, is

$$SNR_{RX} = \frac{P_s}{P_N} = \frac{E_s \times R_s}{N_0 \times BW_{DAC}}. \tag{4.2}$$

We can write the ratio E_S/N_0 in terms of the the receiver noise induced SNR as

$$\frac{E_S}{N_0} = SNR_{RX} \times \frac{BW_{DAC}}{R_s} \tag{4.3}$$

The SNR for DMT, excluding all noises other than receiver thermal noise, is by definition SNR_{RX} since it is referenced to the total DAC bandwidth. For the case of PAM with baud rate R_s, the noise equivalent bandwidth is approximately $2R_s$ and the out-of-band noise is removed by a low pass filter at the receiver. While the thermal noise contribution will be different for PAM, E_S/N_0 will be the same. We use $BW_{DAC} = 32$ GHz as a reference value for our calculations.

4.5.2 C-band SSB-DMT

The SNR per subchannel is found from contributions identified in section 3.4 and is given by (3.17) referenced to unitary subchannel signal power, i.e., before power allocation or channel attenuation. Details on the calculation of $SNR_{k(ICI)}$, $SNR_{k(P2A)}$, and $SNR_{k(SSBI)}$ are provided in section 3.4. We model the bandlimited channel frequency response as a Gaussian low pass filter with 3 dB bandwidth B. Details of BER calculation for SSB-DMT are given in section 3.5.2. The SCR for SSB-DMT is optimized based on section 3.5.3. Note that the power allocation and signal to carrier ratio does not change the overall signal power, only its distribution across frequency.

4.5.3 O-band PAM

Because we are considering PAM in O-band, the only significant degradation is fiber attenuation. The BER of PAM with modulation order M in AWGN is

$$BER_{MPAM} = \frac{M-1}{M \times \log_2 M} \text{erfc}\left(\sqrt{\frac{3SNR}{M^2-1}}\right). \tag{4.4}$$

where erfc is the complementary error function. We next find the SNR value to include in this expression when referencing the receiver noise power to that used for DMT.

In the case of a non-flat channel frequency response, the PAM signal experiences ISI; to reduce this effect an equalizer is used. Nonlinear decision-feedback equalizers (DFE) have been shown to outperform linear feed-forward equalizers, hence we focus on them. PAM BER performance with a nonlinear decision-feedback equalizer was found in [9] via a Gaussian noise approximation. The SNR is reduced due to ISI/equalization. We use this approach and write the cumulative SNR at the equalizer output as

$$\begin{aligned} SNR_{DFE} &= 2\frac{E_s}{N_0} \exp\left\{\frac{1}{f_s}\int_{-f_s/2}^{f_s/2} \ln\left[Y(f)\right] df\right\} \\ &= SNR_{RX}\frac{2BW_{DAC}}{R_s} \exp\left\{\frac{1}{f_s}\int_{-f_s/2}^{f_s/2} \ln\left[Y(f)\right] df\right\}, \end{aligned} \tag{4.5}$$

where f_s is the sampling frequency, $R_s = R_b/\log_2 M$ in which R_b is bit rate, and

$$Y(f) = \sum_{n=-\infty}^{\infty} \left|S(f-nf_s)H(f-nf_s)\right|^2, \tag{4.6}$$

where $S(f)$ is the transmit PAM signal spectrum and $H(f)$ is the channel frequency response. We assume the rectangular PAM pulse sees the same Gaussian channel used in the DMT performance calculation. BER is calculated using SNR_{DFE} and (4.4).

4.6 Performance Comparison

We compare PAM4 and SSB-DMT under a variety of operational constraints, examining the triplet (L, $\Delta\nu$, B), as well as the bit rate. Our goal is to identify under which conditions SSB-DMT in C-band or PAM4 in O-band would be a better modulation choice. For SSB-DMT, some cases may have unattainable target BER due to a limited power budget. We are careful to consider the same power budget for all cases of SSB-DMT and PAM4. Note that while DSP can be used to mitigate SSBI, see for example [20], we consider only standard DMT DSP (without SSBI mitigation). The forward error correction threshold in all comparisons is 3.8×10^{-3}. Note that in all cases in this section DMT refers to SSB-DMT.

4.6.1 Impact of Bandwidth Constraints

In this section we use the analytical tools developed earlier to examine the impact of bandwidth constraints imposed for different hardware solutions. For instance, the use of low-cost silicon photonic modulators can become a bottleneck in the overall channel bandwidth. In one set of comparisons we vary both bit rate and channel bandwidth simultaneously, i.e., where a choice of modulators might exist. In another set of comparisons, we assume a fixed hardware solution limiting channel bandwidth to 25 GHz, and we vary the bit rate. In either case, we present results as a function of the ratio of bit rate to system bandwidth. A lower ratio corresponds to less aggressive bit rates for a given hardware solution, while a higher ratio corresponds to aggressively pushing high bit rates through a restricted bandwidth.

Fixed Bandwidth

Figure 4.2 examines performance when the bandwidth is fixed to 25 GHz (e.g., a given modulator), laser linewidth is equal to 500 kHz, and the bit rate ranges from 50 to 150 Gb/s. For easy comparison with later results, we label the x-axis with the ratio of bit rate to system bandwidth. As PAM4 performance is most influenced by fiber length, we limit our examination to three cases, $L = 10$, 20 and 30 km.

As fiber length is changed, PAM4 and DMT performance varies as seen in Figs. 4.2a, b, and c. For PAM4 this is a simple effect of attenuation with length. For DMT length contributes to several terms in the SNR per subchannel, leading to a more complex effect on performance. In addition, DMT performance changes markedly as we change bit rates. For the shortest fiber (Fig. 4.2a), PAM4 has a clear advantage due to the negligible attenuation. By 30 km (Fig. 4.2c), the lower attenuation on C-band than O-band has tipped the scales to give DMT an edge at all swept bit rates. At a length between these extremes, Fig. 4.2b, the performance of PAM is almost the same as DMT at all bit rates considered.

Bit rate and bandwidth varying

When increasing the baud rate (BR), the PAM noise-equivalent bandwidth increases, and overall noise power increases. This effect worsens the BER of PAM as we increase baud rate (equivalently bit rate for a given M) for a fixed spectral density. As expected, the higher the ratio of bit rate to system bandwidth, the greater the distortion and the worse the BER for PAM in Fig. 4.3. Furthermore, the BER degrades as the bit rate increases from 80 Gb/s in Fig. 4.3b to 120 Gb/s in Fig. 4.3a.

In the case of DMT, greater bit rates require higher modulation levels, i.e., a constellation with more bits per symbol, but requiring greater SNR; as with PAM, performance varies not only with the ratio but also the absolute bit rate. BER performance degrades as we push bit rate (the three curves are progressively higher). For 80 Gb/s (Fig. 4.3b) the performance

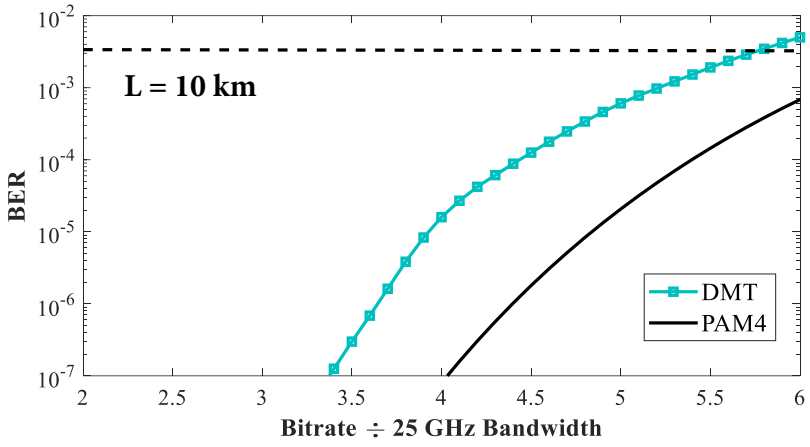

(a)

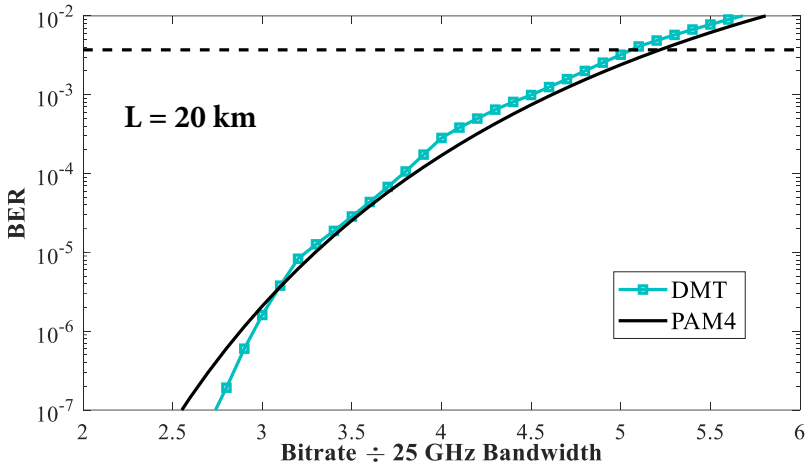

(b)

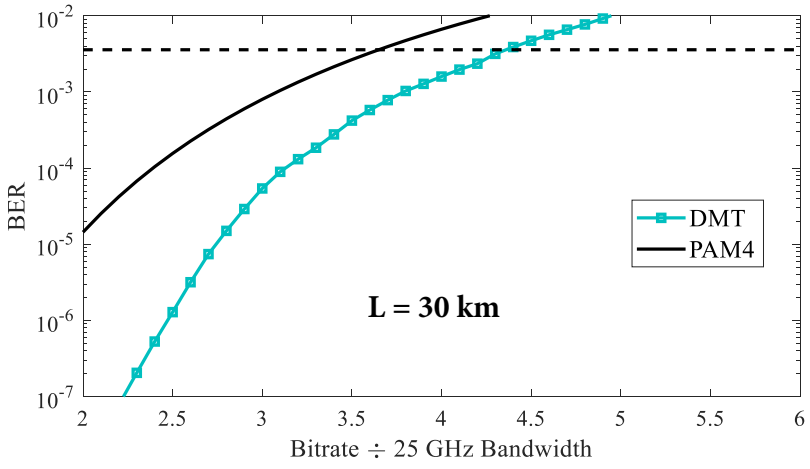

(c)

Figure 4.2 – BER versus spectral efficiency for fiber length = a) 10 km, b) 20 km, c) 30 km. (channel bandwidth = 25 GHz and $\Delta\nu$ = 500 kHz)

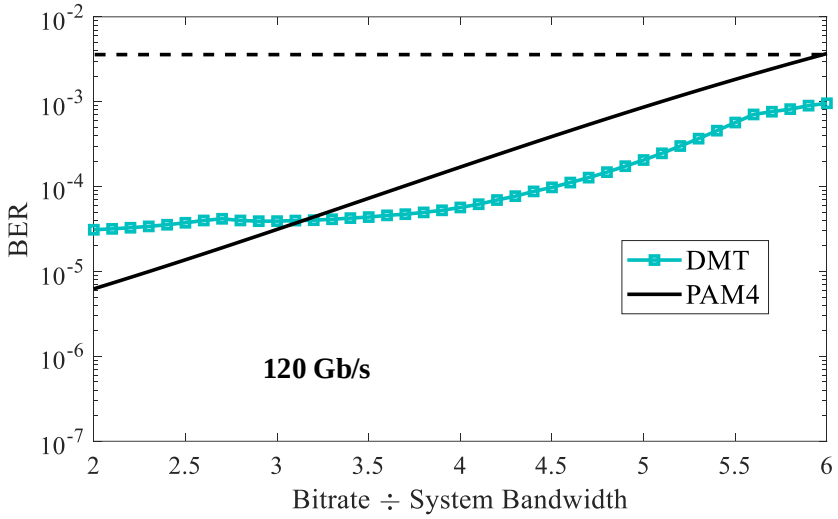

(a)

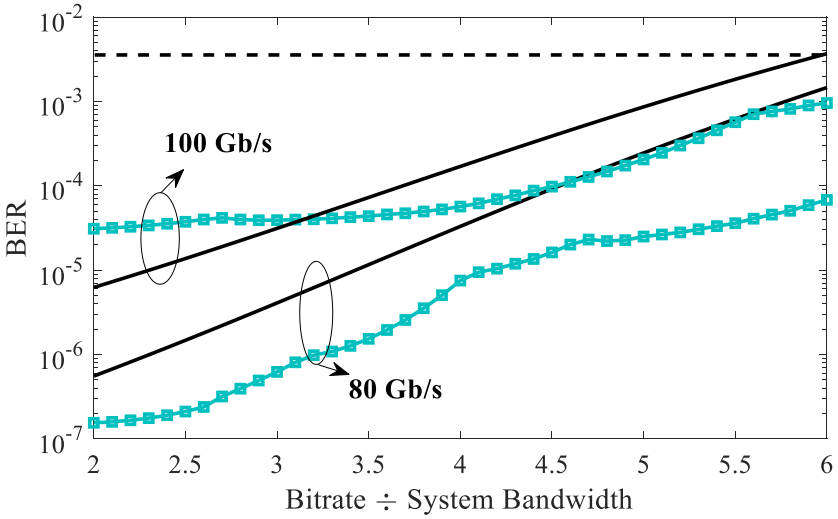

(b)

Figure 4.3 – PAM4 and DMT BER versus the ratio of bit rate over channel bandwidth, for 20 km fiber, 100 kHz laser linewidth, and bit rate = 80, 100, and 120 Gb/s.

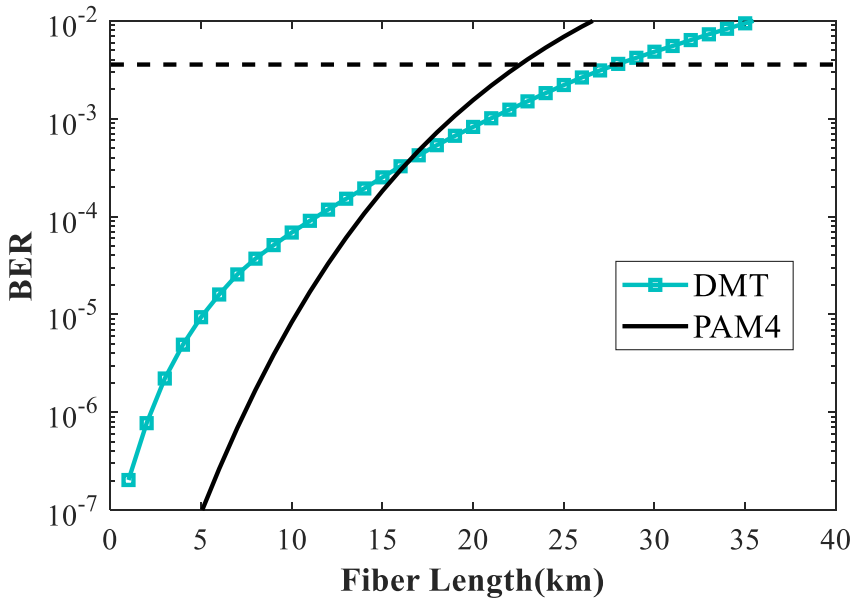

Figure 4.4 – BER versus fiber length for bit rate = 100 Gb/s, system bandwidth = 25 GHz, $\Delta\nu$ = 100 kHz, and γ^2 = -23 dB

of DMT is always better than PAM4, because for low bit rates the water-filling technique (Chow's algorithm) leads to robust, lower QAM orders. By increasing bit rate to 100 Gb/s (Fig. 4.3b), PAM4 and DMT BER curves intersect; PAM4 outperforms DMT in lower bit rate to bandwidth ratios. Further increasing bit rate (Fig. 4.3a) moves the intersection to higher ratios.

4.6.2 Impact of Fiber length and Linewidth

Fiber length

Let us focus on fiber length in Fig. 4.4, for fixed system with bit rate (100 Gb/s), linewidth (100 kHz) and channel bandwidth (25 GHz). Our tools capture the complex impact of fiber length on DMT (in P2A, ICI, PR and power degradation) and quantify at which length DMT and PAM4 performances cross over. Comparisons were also done for 80 and 120 Gb/s (not included in this thesis) and confirm that high attenuation in O-band eventually leads to PAM4 performance worse than DMT; that crossover propagation distance varies with bit rate.

Joint Impact of Linewidth and Fiber Length

While PAM4 is unaffected by laser linewidth, DMT performance will be degraded with wider linewidth. The previous comparisons assumed a narrow (100 kHz) linewidth in order to focus on other effects. In this subsection we vary the linewidth in conjunction with fiber length. As PAM4 performance is heavily determined by fiber length, this provides a good snapshot into

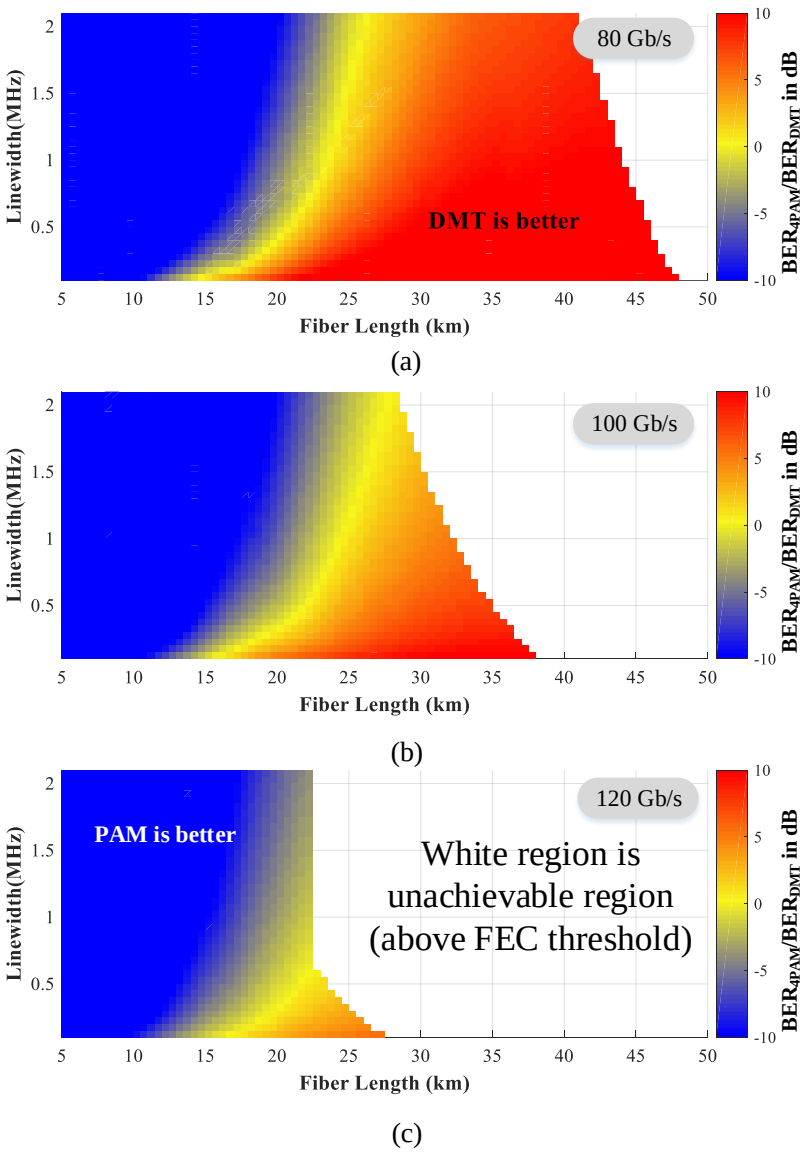

Figure 4.5 – The ratio of BER_{4PAM}/BER_{DMT} in dB, a) Bit rate = 80 Gb/s, b) Bit rate = 100 Gb/s, c) Bit rate = 120 Gb/s (FEC threshold = 3.8e-3)

regimes where PAM4 or DMT might have an advantage.

Figure 4.5 shows via color map, the ratio of PAM4 BER to DMT BER. We sweep fiber length from 5 to 50 km and laser linewidth from 10 kHZ to 2 MHz, a wide range of laser quality. Bandwidth is held at 25 GHz, and three bit rates are examined. These color maps allow the selection of the best modulation for a given cost/quality of the laser source, and desired reach.

The region where DMT is best (red) is largest at lower bit rate, consistent with fixed linewidth results in Fig. 4.3. The region where PAM4 is best (blue) is largest at higher bit

rate, again consistent with Fig. 4.3. Note that white regions reflect unachievable fiber lengths, that is, where the FEC threshold is not respected by either PAM4 or DMT. Intermediate (yellow) areas in Fig. 4.5 shows the crossover between performance of DMT and PAM4. This crossover is slightly moving to higher fiber lengths as linewidth increases, because increasing laser linewidth degrades DMT performance.

4.7 Conclusions

We provide a tool to the systems designer with the choice of both wavelength bands (O vs. C band) and modulation formats. While DMT has inherently greater cost (DAC and FFT) than PAM, we have examined only IMDD DMT to level the playing field and constrain the additional complexity of DMT vis-à-vis PAM. We have provided simulations showing how specific system (reach and bit rate) and hardware (linewidth and bandwidth) choices can shift the relative performance of PAM vs. DMT. The additional cost of DMT hardware must be offset by an appropriate level of performance improvement. Our comparison includes an SSB-DMT solution that is as spectrally efficient as PAM4 and whose performance has been optimized by a judicious choice of the signal to carrier ratio. We have a methodology to select modulation format and appropriate hardware (modulators and laser sources), and to quantify attainable bit rates.

Part II

Coherent Detection Systems

Chapter 5

Flexible Modulation and Frequency Allocations for SNR-limited Coherent Systems

5.1 Résumé

Nous démontrons la transmission cohérente du format de modulation hybride combinant DMT et QAM. Dans un régime limité en SNR, nous démontrons expérimentalement que l'utilisation de la modulation hybride augmente les performances d'un modulateur photonique au silicium.

5.2 Abstract

We demonstrate coherent transmission of hybrid modulation format combining DMT and QAM. In an SNR-limited regime, we demonstrate experimentally the use of hybrid modulation increases performance of a silicon photonics modulator.

5.3 Introduction

The use of hybrid versions of OFDM has attracted interest to overcome various types of impairments. For instance, frequency response limitations can benefit from single carrier PAM at baseband combined with DMT at higher frequencies [34]. PAPR limitations can benefit from having OFDM (either uniform or rate-optimized DMT) yield a section of the lower spectrum to a single-carrier approach.

The main concern with such optimized modulation format is its additional FFT stage at the transmitter side and IFFT stage at the receiver side. This requirement increases the implementation complexity and makes it a less attractive solution for low cost low complexity intensity modulation and direct detection systems in short haul applications, and more suitable for current long haul applications and coherent detection [38], or future short-reach applications, in which implementation cost for coherent detection is reduced.

We examine hybrid modulation for a SiP modulator working in a SNR limited system. We examine experimentally the relative performance of single carrier QAM, rate-optimized DMT, and a hybrid strategy that splits these two options across the available frequencies, taking into account the spectral distribution of the (low) SNR.

5.4 DMT, Nyquist QAM, and Hybrid DMT-QAM

OFDM divides the transmission spectrum into small subchannels to decrease ISI by increasing symbol duration. The main drawback of this technique is high PAPR that increases quantization noise and reduces modulation depth. PAPR is mitigated by techniques such as hard and soft clipping. But in all these methods we are removing a part of the signal, thus increasing bit error rate.

In contrast to OFDM, single carrier modulation has low PAPR. DFT-S is a well known modulation technique that not only divides the overall channel into small subchannels like OFDM (to avoid ISI), but has low PAPR since its data has limited excursions in the time domain.

DMT uses a water-filling technique to allocate the best modulation format and power level for each subchannel based on the available SNR per sub-carrier. DMT maximizes throughput and channel capacity. DMT (like uniform rate OFDM) suffers from high PAPR. As DMT maximizes capacity by varying modulation formats per subcarrier, the DFT-S is not appropriate: different DFT blocks for each modulation formats at both transmitter and receiver side exponentially increases system complexity [39] and is impractical to implement.

Channel frequency response is typically flat at low frequencies leading to the same SNR at these subchannels. Therefore we can create a hybrid modulation by dividing the channel

into two sections, 1) DFT-S in low frequencies, and 2) DMT in higher frequencies. Because we have only one DFT-S part, the additional complexity is only one FFT stage at the transmitter, and one IFFT stage at the receiver. With this technique we are taking advantage of DFT spread to reduce PAPR and also using DMT in higher frequencies to maximize throughput. In this work we compare the performance of Nyquist QAM, DMT and Hybrid DMT-QAM.

5.4.1 Nyquist QAM

The transmitter-side DSP of Nyquist QAM takes QAM symbols and oversamples to achieve the same sampling rate as the DAC. The oversampled signal is pulse-shaped, quantized, and uploaded to the DAC. At the receiver-side, we first remove any frequency offset. Then we equalize the channel via the multi-modulus algorithm. Next, the carrier phase is recovered and compensated. After a final minimum mean square error equialization (MMSE), the BER is measured.

DMT: The SNR of all subchannel is estimated via an OFDM signal using 1024 FFT with QPSK symbols; SNR is calculated from EVM and BER of each subchannel (estimating SNR from EVM is not accurate for low SNR regime and for sub channels with high SNR we don't have enough errors to be able to have an accurate BER calculation and then SNR estimation). Using estimated SNR and Chow's water-filling technique, bit and power allocations per subchannel are found to achieve target BER of 10^{-3}.

Four training frames are added to the DMT signal to help frequency offset estimation at the receiver. DMT data goes through length 1024 IFFT to move it to the time domain. Real and imaginary parts are quantized, and then loaded to the DAC. Receiver side DSP starts with resampling then synchronizing to the FFT frame. Synchronized data goes through Schmidl-Cox's frequency offset compensation block [40], then one tap equalization, followed by carrier phase recovery, and finally BER calculation.

5.4.2 Hybrid QAM/DMT

SNR is estimated using QPSK data with uniform power in both DSP-spread and OFDM frequency sections, including 4 training frames.

Following SNR estimation, binary data is mapped to 16QAM symbols for the DFT-S spectrum allocation. The overall power is chosen (per the estimated SNR) to achieve BER of 10^{-3}. This data is moved to the frequency domain using a length 256 FFT (for the case that QPSK occupies 16 GHz double side band frequency range). For the remaining subchannels, data is mapped to QAM symbols according to the bit and power allocation of each subchannel found via Chow's algorithm. The DFT-S and DMT signals are combined in the frequency domain, training frames are added and then the entire signal is moved to the time domain by a length 1024 IFFT. Real and imaginary parts of the signal are quantized, and then uploaded

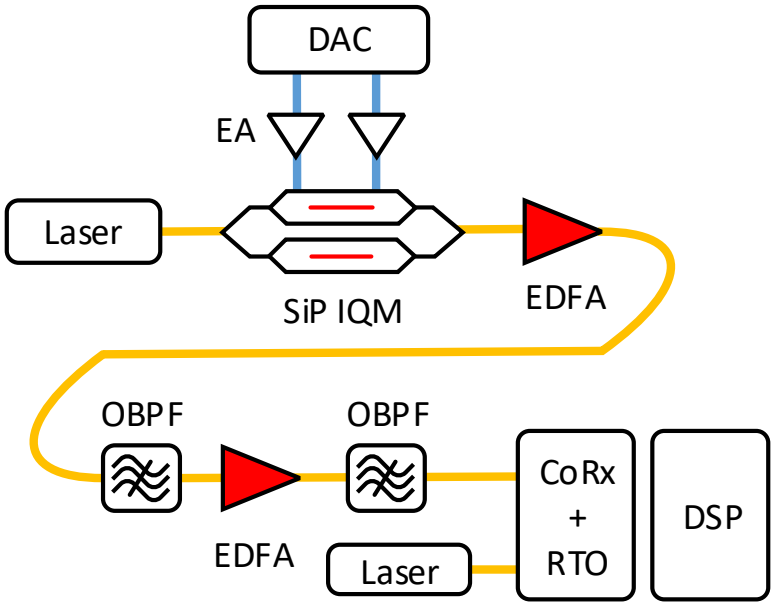

Figure 5.1 – Experimental setup.

to the DAC. At the receiver side, captured data is resampled and synchronized then any frequency offset is compensated with the same method as for DMT. Using a 1024 FFT, data is moved to the frequency domain and the DFT-S part is separated from DMT. For the DMT part, we follow the same steps as explained for DMT.

The DFT spread signal is moved to the time domain using a 256 IFFT; the carrier phase is recovered using the same method as DMT. There are multi-modulus algorithm and MMSE equalization stages, then BER is calculated. A direct detection version of this method is studied in [40], but to the best of our knowledge, this is the first demonstration of this method on coherent detection using a SiP modulator.

5.5 Experimental Setup

Figure 5.1 shows the experimental setup. A 16 dBm continuous wave laser (Cobrite DX1) with linewidth of 100 kHz at 1550 nm, is coupled into the silicon modulator through a fiber array. The silicon IQ modulator consists of two single drive Mach-Zehnder modulators (MZMs) with 4.5 mm length traveling waveguides. The DC bias voltage of the PN-junctions are set to 0 V, to achieve lowest modulation loss (lowest half wave voltage) and 3 dB bandwidth of 20 GHz. The total insertion loss of the silicon IQ modulator is around -27 dB (which includes loss in each MZM phase shifter, on-chip optical routing, and fiber-array coupling).

An order 24 PRBS is generated offline for all modulation IQ tributaries. The I and Q data are resampled to match the 64 GSa/s sampling rate of the 8-bit DAC to generate different

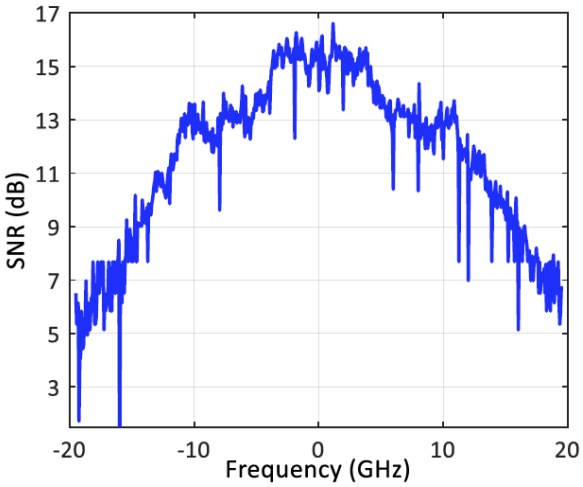

Figure 5.2 – SNR per subchannel.

signaling rates. The IQ drive signals are boosted by two SHF 18 dBm electrical drivers to a 5 V linear peak-to-peak swing, and then applied to the silicon modulator through a GS-SG configured RF probe. The operation point of each MZM is controlled by a thermal heater. The modulated optical light is then amplified by a two stage Erbium-doped fiber amplifier (EDFA) to compensate excess insertion loss. Two optical band pass filters of Finisar Waveshaper 4000S and Alnair Labs BFV-200-SM-FA are deployed after each stage of amplification to reject out-of-band amplified spontaneous emission (ASE) noise.

At the receiver end, the single polarization signal is attenuated to -8 dBm and coherently detected at an integrated polarization diverse coherent receiver with a 13 dBm local oscillator from TeraXion PS-TNL. The resulting electrical signals are captured by a RTO with 33 GHz analog 3 dB bandwidth and sampled at 80 GSample/s sampling ratio. The sampled signal is then processed by off-line DSP using Matlab.

5.6 Results and Discussion

Figure 5.2 shows the SNR per subchannel for our setup, estimated via uniform OFDM with QPSK modulation. As mentioned in the experimental setup section, the overall modulator loss is around 27 dB requiring optical amplification that introduces significant ASE noise. The maximum SNR per subchannel is under 17 dB. Such low SNR limits our transmission rate to maximum 120 Gbps for the best case (using hybrid modulation).

Various Nyquist QAM modulations are tested through the channel, but 16QAM performance was the best. By increasing QAM order the frequency occupation of the signal decreases but noise sensitivity increases as we are in the OSNR limited regime. Therefore our single carrier modulation is limited to 16QAM.

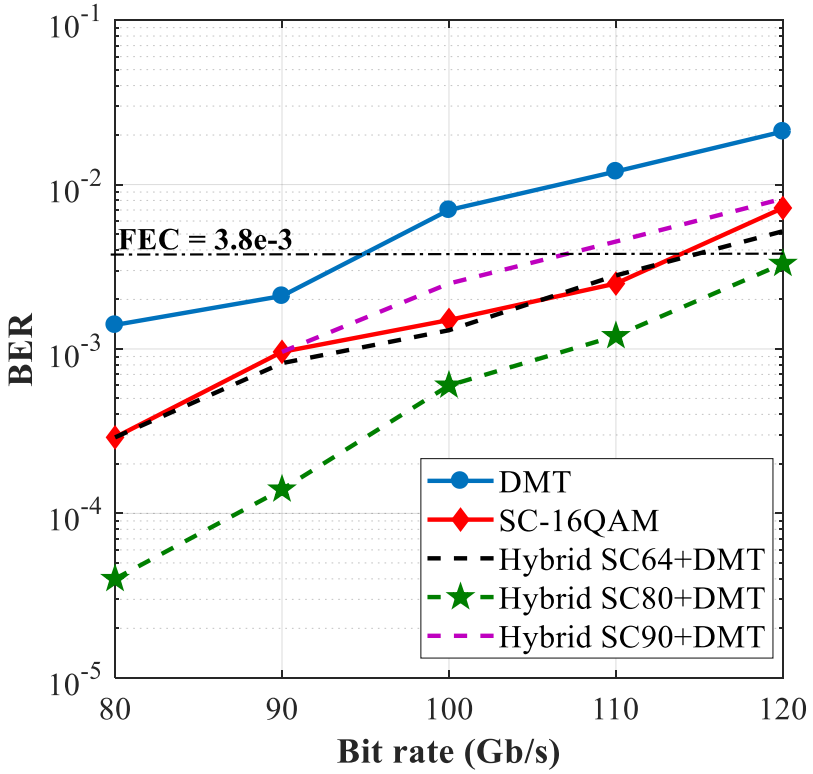

Figure 5.3 – BER vs. bit rate for DMT, single carrier modulation, and hybrid modulation with different DFT-S portions.

Figure 5.3 shows the BER versus bit rate for three different cases of DMT, single carrier 16QAM, and hybrid modulation format in which we have three different configurations of hybrid with different DFT-S portions to find the best one. Considering the curves for hybrid modulation, if we increase the DFT-S portion from 64 to 80 Gb/s the PAPR decreases and the performance increases. The best case for this figure is when the DFT-S portion includes 80 Gb/s of data rate. By increasing DFT-S portion more than 80 Gb/s, the performance of hybrid goes down until it becomes worse than single carrier for the case of 90 Gbps DFT-S. The reason is that by increasing DFT spread the PAPR decreases but at the same time we are limiting DMT in frequency domain and water filling technique allocates high QAM orders with more sensitivity to noise.

Figure 5.3 also shows the BER comparison between single carrier Nyquist QAM, DMT and the best case of Hybrid DMT-QAM which is in green stars. In this case Hybrid DMT-QAM includes QAM up to 10 GHz and DMT from 10 to 20 GHz. The results show that the performance of hybrid is better than others. Because the PAPR of single carrier is lower than DMT, it is more robust to the noise. Since the main distortion source is from AWGN noise induced by EDFAs, the performance of the single carrier is better than DMT. In terms of complexity, we will compare hybrid modulation with standard DMT in section 6.7.

5.7 Conclusion

In this chapter we experimentally compared the performance of single carrier QAM, DMT and hybrid DMT-QAM modulation formats. We examined hybrid modulation in terms of frequency occupation for DFT-S part and found the optimum configuration that gives us the minimum BER. The results shows that using the optimum hybrid enhances the performance.

Chapter 6

Numerical Study of a Hybrid Optical DMT/DFT-S QAM Modulation

6.1 Résumé

Une modulation hybride offre la robustesse du rapport PAPR de la modulation DFT-S QAM avec l'optimisation du débit binaire de la modulation DMT. Nous examinons par simulation dans quelles circonstances cet modulation peut augmenter le débit et/ou l'efficacité spectrale. La réduction hybride du PAPR nous permet d'augmenter la tension crête à crête à l'entrée électrique du modulateur pour améliorer le rapport signal sur bruit. Nous proposons une méthodologie pour identifier la tension crête à crête optimale dans différentes conditions du système. Nous optimisons le débit binaire pour le spectre disponible, c'est-à-dire l'efficacité spectrale, en tenant compte de la nature limitée de la bande passante de l'émetteur.

L'optimisation finale que nous proposons est la partition du spectre disponible dans une bande de fréquence inférieure pour DFT-S et une bande de fréquence supérieure pour DMT. Le niveau de modulation QAM du DFT-S est également optimisé. Nous comparons la performance hybride optimale à la performance DMT pour une gamme de débits binaires dans une bande passante de modulation donnée. L'amélioration des performances se fait au prix d'une plus grande complexité DSP pour la solution hybride. Nous comparons le nombre de multiplicateurs complexes nécessaires pour implémenter la modulation hybride versus DMT pour les systèmes dispersifs et non-dispersifs.

6.2 Abstract

A hybrid modulation offers the PAPR robustness of DFT-S QAM with the bit rate optimization of DMT modulation. We examine via simulation under what circumstances this modulation can increase bit rate, and/or spectral efficiency. Hybrid PAPR reduction allows us to increase the peak-to-peak voltage at the modulator electrical input to enhance optical signal to noise ratio. We propose a methodology to identify the optimal peak-to-peak voltage in different system conditions. We optimize the bit rate for the available spectrum, i.e., the spectral efficiency, taking into account the bandwidth limited nature of the transmitter (combined electrical and optical bandwidth).

The final optimization we propose is the partition of the available spectrum into a lower frequency band for DFT-S and a higher frequency band for DMT. The QAM modulation level of the DFT-S is also optimized. We compare the optimal hybrid performance versus DMT performance for a range of bit rates for a given modulation bandwidth. Improved performance comes at the cost of greater DSP complexity for the hybrid solution. We compare the number of complex multipliers required to implement hybrid versus DMT for both dispersive and non-dispersive systems.

6.3 Introduction

Ever growing demand for network capacity requires increased link speed. This requirement attracts research groups to enhance digital signal processing techniques by designing new modulation formats to increase spectral efficiency, equalize non-flat frequency response, and so on. DMT and DFT-S QAM are two contrasting approaches to this challenge.

As explained in chapter 5, DMT divides available spectrum into narrow-band subchannels, and uses waterfilling techniques to optimally allocate modulation order and power across these subchannels. With knowledge of the SNR per subchannel, we can maximize channel capacity. DMT suffers from PAPR, leading to higher levels of quantization noise [41], amplifier-induced nonlinearities, and modulator transfer function nonlinearity, as compared to other modulations [42]. The most common method to reduce PAPR is clipping, this distortion being milder than that induced by high PAPR [43].

DFT-S modulation allows frequency domain precompensation, a kind of power allocation not unlike DMT. The PAPR of DFT-S modulation is much lower than that of DMT. This method recently achieved 560 Gbit/s with IMDD, where four wavelength channels used DFT-S 128QAM for a 2 km transmission [44].

Unlike DMT modulation, DFT-S cannot assign a non-uniform number of bits per frequency subdivision, as modulation occurs in the time domain before the FFT. This precludes DFT-S from maximizing capacity. Combining DFT-S with DMT in a hybrid modulation we can seek PAPR reduction (as compared to DMT alone), while enhancing spectral efficiency (as compared to DFT-S alone). This approach was used with IMDD when combining PAM and DMT [45], and combining OFDM with PAM in a hybrid fiber-visible laser light system [46].

Hybrid modulation experiments with coherent detection were recently reported with 25 Gb/s vertical cavity surface emitting laser technology in [47] and in our work with a silicon photonics Mach Zehnder IQ modulator [48]. No systematic evaluation of the advantages of the hybrid in coherent detection has yet appeared for these systems.

In this chapter we study the optimization of joint DMT and DFT-S QAM modulation to increase bit rate, and/or spectral efficiency in coherent detection systems. We provide a technique to find optimal hybrid modulation parameters. We study the trade-off between modulator nonlinearity (induced by high PAPR) and AWGN noise in terms of modulator optical output power or electrical input peak-to-peak voltage (V_{pp}). From this study we derive a driving strategy that minimizes BER for a hybrid modulation, while taking into account the bandwidth limited nature of the transmitter. We propose a partition of the available spectrum into a higher frequency band for DMT and a lower frequency band for DFT-S (at optimized QAM modulation level). We compare the performance of optimal hybrid to that of simple DMT for a range of bit rates for a given modulation bandwidth.

Section 6.4 starts with the principals of the hybrid approach. We describe the simulation model and transmitter and receiver side DSP. In section 6.5, we study the hybrid of uniform DMT and DFT-S QAM to find V_{pp} yielding minimum BER. In section 6.6 we optimize the modulation order for QAM, as well as the frequency band partition between DFT-S QAM and DMT. In the end of section 6.6 we compare the optimized hybrid with standard DMT. Section 6.7 is dedicated to a complexity comparison of hybrid modulation and standard DMT. Section 6.8 offers some concluding remarks.

6.4 Principles of Hybrid Modulation and Required DSP

Unlike DMT, PAPR for single carrier modulation can be very low. PAPR varies with pulse shaping; for raised cosine pulse shaping, PAPR is lowest for rectangular pulses and largest for sinc pulses (also known as Nyquist pulses). While Nyquist pulses have the highest PAPR, they have the best spectral efficiency, equal to that of uniform DMT.

DFT-S is a frequency domain implementation of the Nyquist single carrier approach - an alternative to raised cosine approximations to the sinc pulse. With DFT-S, QAM data is generated in the time domain and moved to the frequency domain using a FFT. In the frequency domain we sculpt frequency occupancy, also constraining it to a limited bandwidth. An IFFT moves data back to the time domain. Sculpting the signal in the frequency domain helps us to adapt the waveform to channel characteristics.

As explained in the introduction, we create a hybrid modulation by combining DFT-S QAM signal in lower frequencies (where the frequency response is almost flat and the lack of bit allocation is less critical) and DMT in higher frequencies. The single carrier DFT-S QAM part of the combination lowers PAPR (compared to DMT), and the DMT part of helps us maximize throughput (compared to DFT-S QAM) using proper bit allocation and power allocation. Details of this combination is explained in this section. We present our simulation model and our estimation of SNR (per subchannel in the case of the DMT part). We describe transmitter side DSP for signal sculpting, as well as receiver side DSP. The description covers hybrid modulation; when the DFT-S part is set to zero, it covers standard DMT as well.

6.4.1 Simulation Model

Figure 6.1 shows the simulation model, transmitter side DSP, and receiver side DSP for the hybrid modulation format. The simulator introduces nonlinear behavior in the sinusoidal transfer function of the modulator.

The first block in our simulation model is a DAC with high resolution (8-bit) and a 64 GSample/s sampling rate. The bandwidth limitations of the DAC and modulator are simulated with a single low pass Gaussian filter. The modulator is biased at the null point

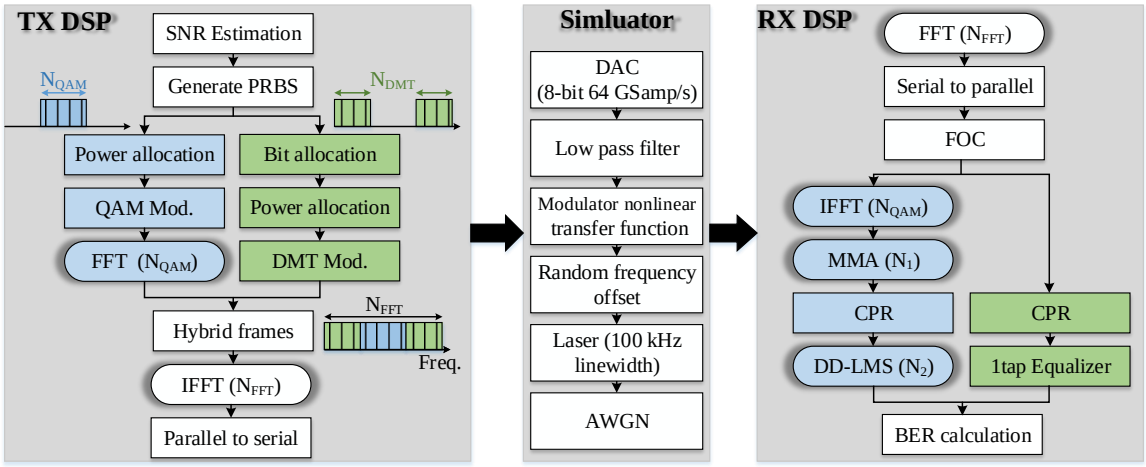

Figure 6.1 – Monte Carlo simulation block diagram (center panel) and flowcharts for hybrid modulation for transmitter-side (left panel) and receiver-side (right panel) DSP.

and has the typical sinusoidal transfer function, normalized so that the maximum amplitude input voltage of $V_\pi/2$ generates an output signal equal to one. The mismatch between the local oscillator and the transmit laser is modeled with a random frequency offset, uniformly distributed between 0 and 500 MHz. The laser is modeled as having phase noise described by a Wiener process and parameterized by a 100 kHz linewidth. Finally, AWGN is added to reflect the noise level being examined. The key simulation parameters are summarized in Table 6.1.

Table 6.1 – Key Simulation Parameters.

Parameter	Value
DAC	28-bit + 64 GSample/s
Laser	Phase noise with Wiener process (LW = 100 kHz)
Modulator	LPF + Transfer function nonlinearity
Frequency offset	Random number between 0-500 MHz

6.4.2 Transmitter DSP

Before starting transmitter-side DSP, we estimate the SNR that will be used for waterfilling and for power allocation between the DMT and the DFT-S QAM portions of the spectrum. In this block, we fix the percentage of available spectrum allocated to DFT-S QAM, illustrated as a block of N_{QAM} subchannels at baseband, and N_{DMT} subchannels at higher frequency. We then run a simulation transmitting QPSK signals with uniform power allocations for DFT-S QAM and DMT. DMT subchannels with the same power level and modulation (QPSK), i.e., uniform DMT is also known as OFDM. At the receiver we estimate the SNR per subchannel for the DMT spectra, and overall SNR for the DFT-S QAM spectrum using

techniques described in [1]. This is repeated for each partitioning of the spectrum that we examine.

The total FFT size is $N_{FFT} = N_{DMT} + N_{QAM}$, as illustrated in Fig. 6.1. The ratio N_{FFT}/N_{QAM} gives the percentage of spectrum allocated to DFT-S QAM. The transmitter side DSP starts with generating a PRBS of order 22. For a fixed hybrid (DFT-S QAM modulation level and percentage of spectrum), we divide the bit sequence appropriately between the two branches in the TX DSP section of Fig. 6.1.

For a fixed hybrid (modulation order for DFT-S and N_{QAM}), we calculate the power allocation for the DFT-S partition as the amount of power needed to achieve a target BER of 10^{-3} based on overall QAM SNR. For the DMT portion, we use Chow's waterfilling algorithm [14], to allocate power again with target BER of 10^{-3}. The bit allocation step of waterfilling [14] spreads the DMT bits among subchannels (N_{DMT} in Fig. 6.1) to achieve the target bit rate. Target bit rate is adjusted to find the highest bit rate achievable.

Modulated QAM symbols for the DFT-S spectrum are moved to the frequency domain with an FFT block. In the frequency domain the DFT-S data is concatenated with DMT data to fill the entire available spectrum as illustrated in cartoons in Fig. 6.1. Finally, a preamble is added for frequency offset estimation. The frequency domain signal is moved to the time domain using an IFFT block. The last stage is parallel to serial conversion.

6.4.3 Receiver DSP

The receiver side DSP starts with an FFT block to move the time domain signal into the frequency domain. We then apply FOC using the Schmidel-Cox algorithm [40]. After FOC, we separate QAM data from DMT. In the DMT side we apply CPR, then one tap equalization and finally we estimate BER.

For the QAM data, we first pass through a parallel to serial block. We then apply blind channel equalization using an N_1 tap multi-modulus algorithm (MMA) at two samples per symbol [49]. We next down sample the data to one sample per symbol and go into the CPR block. After CPR we apply a N_2 tap decision-directed least mean square error (DD-LMS) equalizer and finally we calculate BER.

We used the same CPR technique for both QAM and DMT. We use a small portion of the data in each frame (1/30) to estimate phase rotation for that frame. This estimated phase is applied to all samples of the frame. This method has lower complexity than blind search [50] or other CPR methods. Bit error rate was estimated via Monte Carlo methods, testing 2×10^7 bits and counting a minimum of 20 errors.

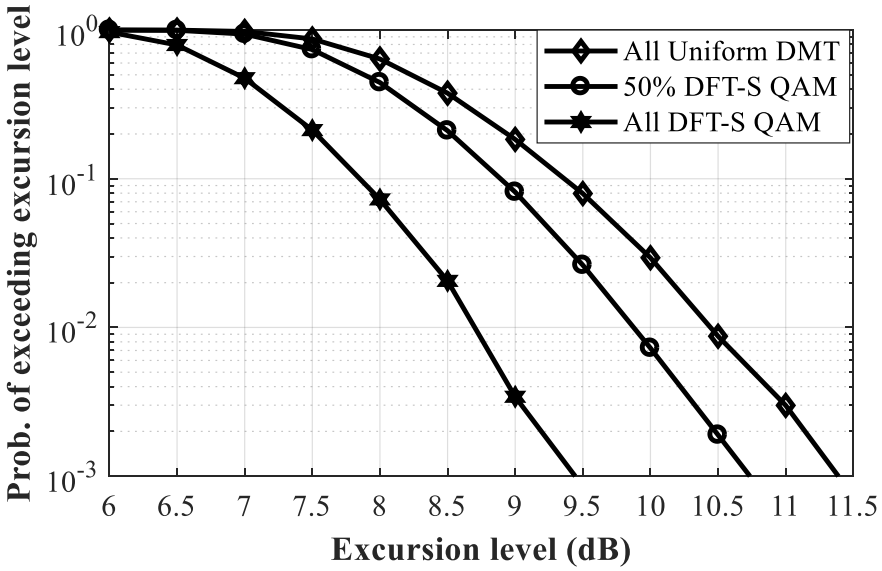

Figure 6.2 – Probability of exceeding at any instance a certain level of excursion from the signal mean value for: strictly uniform 64QAM DMT, strictly DFT-S 64 QAM, and a hybrid of half spectrum uniform 64QAM DMT and half spectrum DFT-S 64QAM.

6.5 Driving Strategy for Hybrid Modulation

In this section, we show that increasing the DFT-S portion of the hybrid decreases the PAPR for the hybrid modulation. Then we study the trade-off between AWGN noise and the modulator nonlinear transfer function. From this trade-off we derive a driving strategy for the modulator to minimize BER for a specific hybrid spectral partition, SNR value, and modulator bandwidth. Following that we optimize modulation order and frequency occupation for DFT-S portion for a fixed bit rate. Finally we find the maximum bit rate under the FEC threshold for optimized hybrid modulation and compare it to standard DMT.

6.5.1 Impact of hybrid spectral partition on PAPR

As explained in the introduction, the main reason to combine DFT-S QAM and DMT is to reduce PAPR. Quantization noise is negligible when using a high resolution (8-bit) DAC, but transfer function nonlinearity can be severe in the presence of high PAPR. The nonlinear distortion is most severe for large excursions from the mean value. The higher the PAPR, The greater the probability of such excursion occurring. The probability of the excursion above the mean is a good predictor of PAPR impact. Typically, excursions of 9.5 dB above the mean value are considered to generate excessive nonlinear distortion.

In Fig. 6.2 we plot the probability of exceeding the mean by a certain excursion level in dB for three hybrid spectral partitions. In the first case we generate uniform DMT, the second one is a combination of 50% DMT and 50% DFT-S QAM, and the last one is all

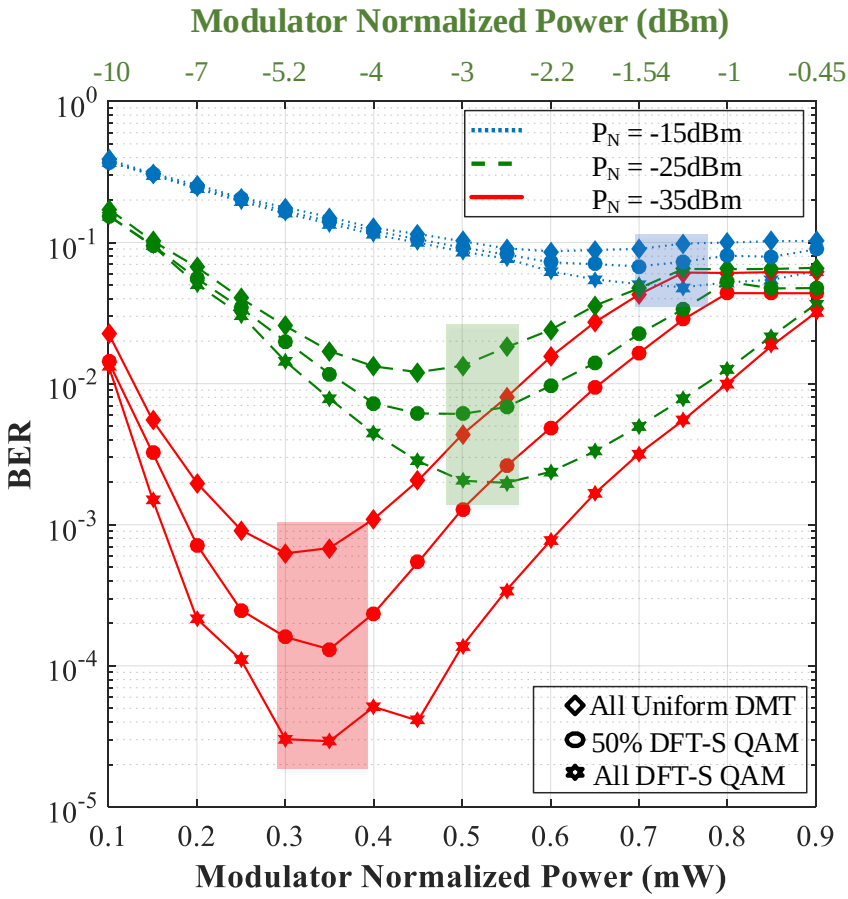

Figure 6.3 – BER versus normalized modulator output power at three noise levels for: strictly uniform 64QAM DMT, strictly DFT-S 64 QAM, and a hybrid of half spectrum uniform 64QAM DMT and half spectrum DFT-S 64QAM.

DFT-S QAM.

Consider the excursion level of 9.5 dB, where nonlinear distortion limits performance. At this level, uniform DMT has 10% of samples distorted. By using a 50-50 hybrid this probability is decreased to 2%. For the case of all DFT-S QAM modulation, only 0.1% of samples are distorted, which is negligible. Clearly DFT-S QAM has lower PAPR, as expected and by adjusting the mix of DMT and DFT-S we can tune the level of PAPR. That is, varying the percentage of DFT-S QAM can shift the plot in Fig. 6.2 any where between the two extremes of all uniform DMT and all DFT-S QAM

6.5.2 Driving strategy minimizing BER

Nonlinearity induced by the modulator sinusoidal transfer function can be reduced by lowering mean power, i.e., operating at lower V_{pp}. While low V_{pp} reduces nonlinearity, it decreases SNR as well. Proper choice of V_{pp} balances these two effects to minimize BER. We examine the trade-off to find the optimal driving strategy for two cases: for modulator bandwidth much

greater than required for the transmission rate (infinite bandwidth) and for bandwidth limited operation, i.e., high bit rates. We used Monte Carlo techniques in the simulator shown in Fig. 6.1 to calculate the BER for each case in this section.

Influence of noise level for infinite bandwidth

In this subsection we continue to use uniform DMT, leaving power and bit allocations for the following sections. The low pass filter in Fig. 6.1 is not present for simulations of this infinite bandwidth case. The noise levels are fixed for the simulation. In this way we can set the noise level independently of the bandwidth assumption.

Figure 6.3 shows the BER versus normalized modulator output power for three values of noise power (P_N): -35 dBm, -25 dBm, and -15 dBm. This values combined with signal power range of -10 to 0 dBm helps us to cover an overal SNR range of 5 to 45 dB. We swept normalized modulator output power by changing the peak-to-peak voltage, while we fixed the bias at the null point. For each value of P_N we consider the three modulations for which we found the PAPR cumulative distribution function in Fig. 6.2.

Lowering PAPR with a fixed SNR reduces the effect of modulator transfer function nonlinearity, decreasing the BER. This effect can be seen no matter the level of P_N. This is also true when sweeping the x-axis. The BER performance is best for full DFT-S QAM, followed by the 50% hybrid, and uniform DMT has the worst performance. The BER trend follows the PAPR cumulative distribution function.

Consider the optimum values for modulator output power for all nine cases shown in Fig. 6.3. The optimum value changes significantly with the noise level. For a fixed noise level, however, the minimum BER occurs at roughly the same normalized modulator power no matter the PAPR level, i.e, no matter the hybrid partition. The optimum region of normalized modulator power is shaded for each noise power case, e.g., the red region (around 0.35 mW) covers the case of $P_N = -35$ dBm. If we increase noise level by 10 dB the optimum value increases to around 0.55 mW. Greater modulator output power is required as we are AWGN noise limited rather than PAPR limited. Further increase in noise power up to -15 dBm increases the optimum value of modulator output power to around 0.75 mW.

Limiting the bandwidth of the system could reduce PAPR of the signal by attenuating higher frequencies and avoiding sudden changes in the amplitude of the signal. For different values of modulator bandwidth the value of SNR will be the same if we keep modulator output power unchanged. Therefore we expect changing system bandwidth should have negligible effect on the optimum value of modulator output power, for the same reasons this was the case when changing the hybrid spectral partition between DFT-S and DMT. We examine this hypothesis in the following.

Influence of noise level for finite bandwidth

For the rest of the chapter our simulator includes a low pass Gaussian filter with a 3 dB bandwidth of 25 GHz. When the system bandwidth is limited, optimized DMT uses waterfilling to adapt the signal to the channel frequency response, thus outperforming uniform DMT. For the balance of the chapter, we maximize capacity by allocating the appropriate power and number of bits per symbol at each subchannel.

The AWGN noise power is set to -33 dBm, a reasonable value for a 25 GHz receiver. From Fig. 6.3, at this noise level the modulator normalized power should be around 0.4 mW to minimize BER, regardless of hybrid split or the system bandwidth. This modulator output power corresponds to 29 dB SNR, which is a reasonable value for a back-to-back experiment.

Figure 6.4 shows the BER versus modulator output power for four different hybrid combinations, all of which achieve a bit rate of 260 Gb/s. The DFT-S 64QAM portion of the four hybrid modulations examined has bit rate varying from 100 Gb/s to 240 Gb/s; the balance of the 260 Gb/s is covered by the waterfilled DMT. Figure 6.4 confirms that the optimal modulator output power is around 0.42 mW, which is in less than 0.1 mW range from what we predicted for infinite bandwidth in Fig. 6.3. While not reported here, we confirmed the same behavior for a variety of system bit rates and bandwidths. In all cases, the optimum modulator output power is not affected by the hybrid spectral allocation, nor by the system 3 dB bandwidth.

6.6 Optimizing Bit Rate

By changing the hybrid spectral allocation to place the split between DMT and DFT-S QAM at higher frequencies, we increase the DFT-S portion and decrease the PAPR of the overall signal. Lower PAPR means lower nonlinear distortion and better performance. Placing the split point too high leads to limited bandwidth to meet DMT bit rate targets. This will force the waterfilling to go to advanced QAM orders that require strong SNR. At these high frequencies, however, the SNR will be limited as the channel rolls off. This is reflected in Fig. 6.4 where we see BER improvement until 52%, and a rapid deterioration at 62% (DFT-S QAM bandwidth as a percentage of the total bandwidth covered by the FFT (64 GHz in our simulations)).

In the first subsection, we find the optimal split point assuming a fixed QAM level for the DFT-S QAM section. This optimization is done for each candidate QAM level. For a given overall bit rate, we identify the best split point and QAM order to minimize BER. We compared the optimized hybrid with DMT for different bit rates in the second subsection. As previously, the SNR is 29 dB, modulator output power is 0.4 mW, and system 3 dB bandwidth is 25 GHz.

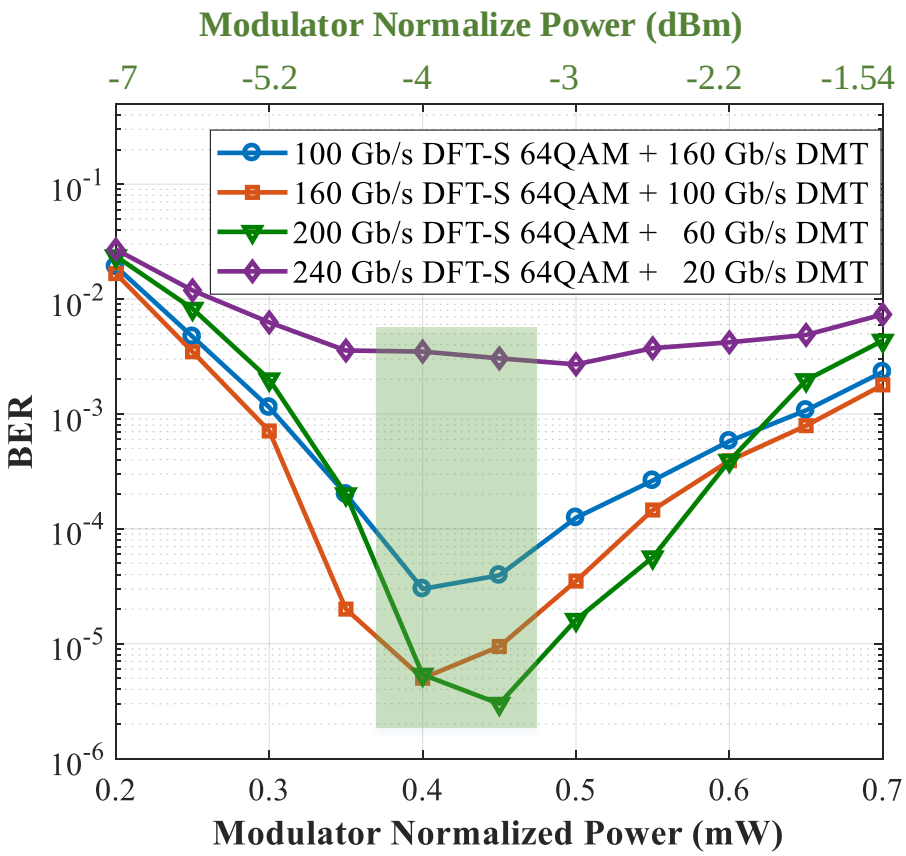

Figure 6.4 – For overall bit rate of 206 Gb/s, noise power of -33 dBm, and 25 GHz system bandwidth: BER versus normalized modulator output power for four different hybrid spectral allocations.

6.6.1 Fixed QAM level for DFT-S

We fix the overall bit rate to 320 Gb/s and examine three candidate levels for the DFT-S QAM partition: 32QAM, 64QAM, and 128QAM. We next sweep the hybrid spectral partition and find the BER for that hybrid modulation. Figure 6.5 plots a) BER and b) QAM power portion vs. the hybrid partition. The lower x-axis is keyed to the bandwidth allocated to DFT-S QAM, while the upper x-axis gives this frequency as a percentage of the total bandwidth covered by the FFT (again, 64 GHz). For example, for DFT-S 64QAM with 20 GHz bandwidth, the bit rate for DFT-S 64QAM is $20 \times 6 = 120$ Gbit/s and the DMT bit rate is $320 - 120 = 200$ Gbit/s. The three curves in Fig. 6.5 are for 32QAM, 64QAM, and 128QAM, shown by red (circle marker), green (triangle marker), and blue (square marker) lines, respectively.

The dashed horizontal line in Fig. 6.5.a is a reference point for the BER when using strictly DMT with waterfilling and no DFT-S QAM. We observe that for higher QAM modulations (64 and 128), there is a clear optimum hybrid spectral allocation minimizing BER. At 32QAM,

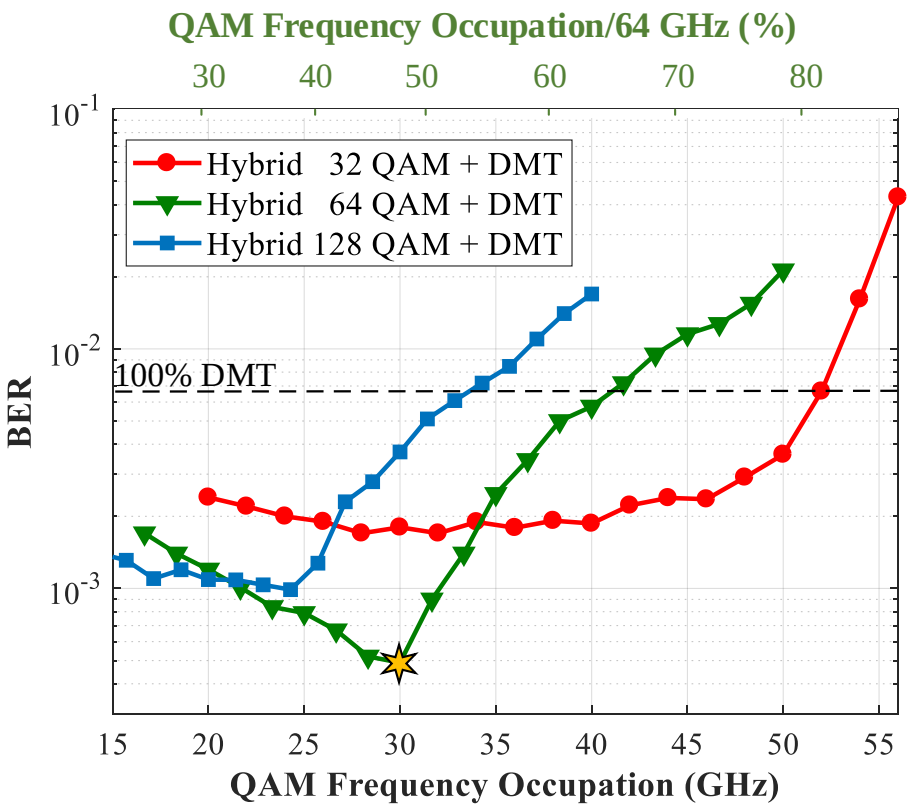

(a)

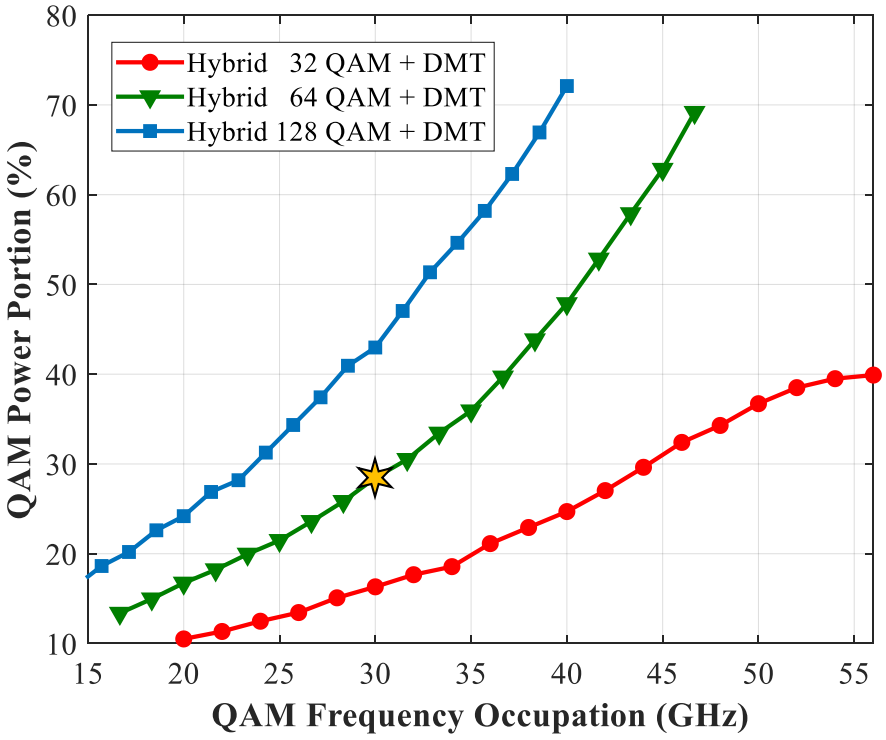

(b)

Figure 6.5 – a) BER and b) QAM power portion, each versus DFT-S QAM frequency occupation for three different choices of QAM order; 320 Gb/s overall bit rate, -33 dBm noise power, 25 GHz system bandwidth, and 0.42 mW modulator output power.

the BER curve is very shallow, with a range of QAM frequency occupation achieving best BER. In Fig. 6.5.b we plot the percentage of power allocated to QAM as a function of QAM frequency occupation. The percentage grows monotonically, as a greater portion of spectrum requires more power. As higher order DFT-S QAM has greater sensitivity to AWGN, the curve is highest for 128QAM, lowest for 32QAM. We see in Fig. 6.5.b that for 32QAM the power allocation to QAM saturates at 40%; in this region DMT can exploit its flexibility to go to higher order modulations. For 32QAM, the hybrid performs better than 100% DMT, but does not achieve the gains when QAM is permitted to go to higher orders (64 and 128).

Higher order DFT-S QAM at a given frequency occupation means higher bit rate in the DFT-S QAM part; we have higher spectral efficiency, but more sensitivity to the AWGN. At high frequency occupation (35% and higher), we see in Fig. 6.5.a the typical relative performance: lowest BER for 32QAM and highest BER for 128QAM. At lower occupation (33% and below), we see the trade-off in the hybrid modulation: lower BER by balancing the PAPR (nonlinear) and AWGN (linear) impairments.

More power devoted to QAM means more PAPR reduction; at the same time, it reduces the DMT power allocation making it harder to achieve the DMT BER target. This trade-off is visible in the intersecting curves and clear minima (64QAM and 128QAM cases) in Fig. 6.5.a BER curves. For instance, at 22 GHz the curves for 64QAM and 128QAM BER intersect. Above 22 GHz DFT-S 64QAM is a better choice, as DMT does not have enough resources (power and spectrum) to overcome the restrictions imposed by noise sensitivity in DFT-S 128QAM. The minima occur when the two DMT effects (PAPR advantage, power allocation disadvantage) balance.

Returning to 32QAM, this is clearly not a good choice for the 320 Gb/s target. The flat part of the curve shows there is a balance in reduced PAPR and limited DMT frequency range. For 320 Gb/s, the best choice is 64QAM with 30% QAM frequency occupation, as shown in Fig. 6.5.a and 6.5.b by a gold star. Despite the nonlinear curves in Fig. 6.5b, the optimal power allocation happens to be about 30% (y-axis) as well.

6.6.2 Experimental validation

Figure 5.3 from chapter 5 shows the BER versus bit rate DMT and hybrid modulation format in which we have three different configurations of hybrid with different DFT-S portions to find the best one. Details about our experimental setup is provided in subsection 5.5. Considering the curves for hybrid modulation, if we increase the DFT-S portion from 64 to 80 Gb/s the PAPR decreases and the performance increases. The best case for this figure is when the DFT-S portion includes 80 Gb/s of data rate. By increasing DFT-S portion more than 80 Gb/s, the performance of hybrid goes down until it becomes worse than single carrier for the case of 90 Gbps DFT-S. This validates our simulation results in Fig.5.3.a where we

have an optimum QAM frequency occupation for all cases. The experiment is done before developing our driving strategy, so we couldn't include that part in our experiment.

6.6.3 Experimental validation

In 5, we reported an experimental investigation of the hybrid modulation, but without optimization of the driving strategy outlined in section III. In that experiment, we examined only 16QAM for the DFT-S portion, but at three different frequency occupations. The 100% DMT case was also examined. We used a silicon photonic traveling wave modulator with a 3 dB bandwidth of 20 GHz. Due to coupling losses, the SNR was limited to 23 dB. The 20 GHz band and was divided into 256 subbands for the hybrid modulation; a total of 120 Gb/s was transmitted.

Details of our experimental setup are provided in 5.5, while Fig. 5.3 shows the BER versus bit rate achieved. Pure DMT (blue, circle markers) has higher error rate than all three hybrid modulation scenarios. When sweeping the DFT-S frequency occupancy from 25% to 35% we can see the importance of PAPR mitigation peaking and diminishing. From 25% occupancy (representing 64 Gb/s of the total 120 Gb/s) we increase to 31% (80 Gb/s) to see the best performance. Increasing occupancy beyond this point leads to a small power allocation to DMT that causes a decrease in performance. At 35% occupancy, the hybrid performance is worse than pure DFT-S, *i.e.*, DMT is not helping. This validates our simulation results in Fig. 6.5a, where we have an optimum QAM frequency occupation.

6.6.4 Best hybrid for bit rate

We repeated the optimization procedure described in the last subsection as we swept bit rates. The highest modulation level for a DMT subchannel was 128QAM, hence the modulation levels we examined for DFT-S QAM were sufficient to cover achievable performance. Figure 6.6 shows a plot of BER for the best choice of hybrid configuration in red (star markers). The maximum bit rate under the FEC threshold of 3.8e-3 (7% overhead hard decision FEC) for DMT alone is 320 Gb/s. This rate increases by 360 Gb/s if we use hybrid modulation. As the bit rate decreases, the performance enhancement of the hybrid decreases. Pushing to these aggressive bit rates in a 64 GHz bandwidth (see spectral efficiency given in upper axis), requires a DMT portion with a high bit allocation. However, including more DMT leads to less PAPR reduction.

Figure 6.7 shows the hybrid spectral allocation that yielded the best performance for each bit rate, i.e., the DFT-S frequency occupation for the points in Fig. 6.4. From 260 to 340 Gb/s, the best constellation for DFT-S QAM is 64QAM. Above 340 Gb/s, it is better to reduce frequency occupation and increase QAM order to send more bits over a smaller frequency range; DMT waterfilling over more frequency bins allows the bit rate to grow.

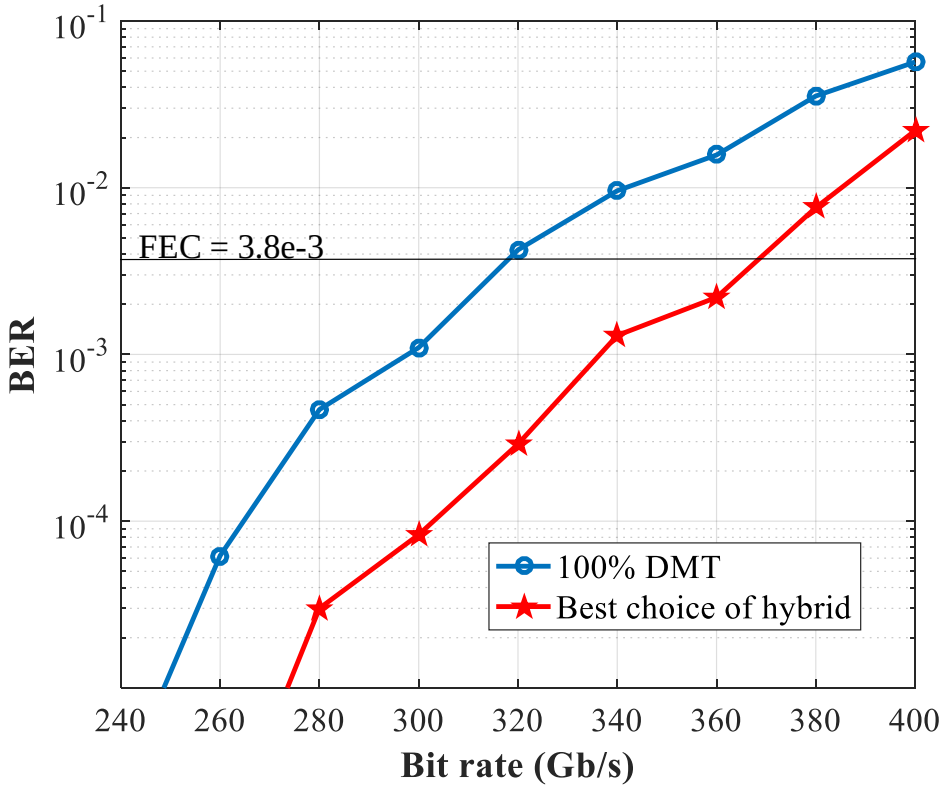

Figure 6.6 – For noise power of -33 dBm, 25 GHz system bandwidth, and modulator output power of 0.42 mW: BER versus bit rate for 100% DMT (blue circle markers) and best choice of hybrid (red star markers).

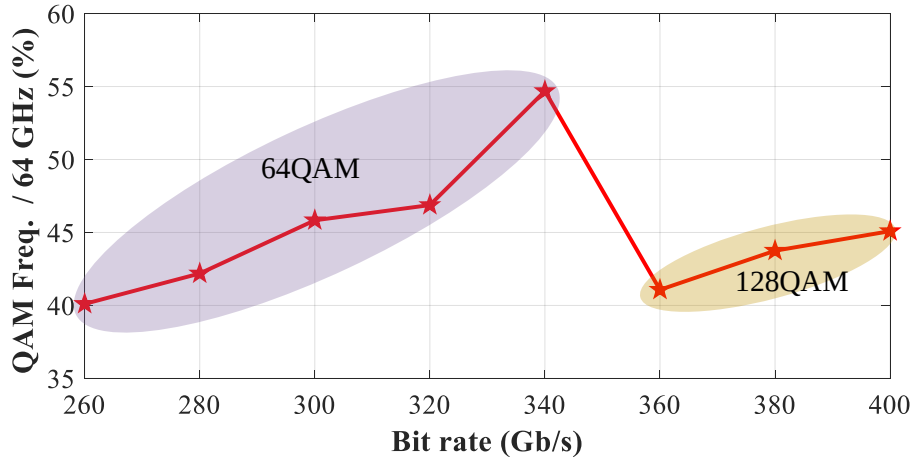

Figure 6.7 – For noise power of -33 dBm, 25 GHz system bandwidth, and modulator output power of 0.42 mW: Best hybrid spectral allocation for targeted bit rates; best DFT-S QAM modulation was 64QAM for bit rates up to and including 340 Gb/s, 128QAM at 360 Gb/s and higher.

6.7 Complexity increase with hybrid

Using a hybrid modulation format enhances system performance, but requires additional DSP blocks for both DMT and QAM subsystems. Such extensive DSP increases the complexity and implementation cost. In this section, we calculate the complexity of hybrid modulation and compare it to DMT. We first identify DSP blocks that represent the largest portion of processing complexity, and then focus on the the complexity for these blocks.

Whether implemented in an application specific integrated circuit (ASIC) or a field programmable gate array (FPGA), the latency of a multiplier is greater than that of an adder. But more importantly, the cost and chip space of a multiplier is much higher than that of an adder. Therefore, we restrict our complexity analysis to the number of multipliers per bit.

In the next subsections we assume zero dispersion, and focus on the complexity of hybrid modulation alone. In the final subsection, we discuss how a dispersion compensation block impacts the overall complexity when using a hybrid.

6.7.1 Common and negligible DSP operations

The DSP tasks in Fig. 6.1 are formatted to identify DSP relevance to our comparison of complexity. All white boxes are DSP needed for both QAM and DMT modulations and are not considered as additional complexity vis-á-vis standard DMT. DSP blocks unique to DFT-S QAM or DMT are shown with blue and green boxes, respectively.

Blocks with high complexity are shown with rounded edges in Fig. 6.1. On the transmitter side, we have an FFT stage for the DFT-S QAM DSP flow, and an IFFT block for the hybrid signal that contribute significantly to complexity. On the receiver side, system complexity is determined by the FFT stage for hybrid signal, and the IFFT block and MMA and DD-LMS equalizers for the DFT-S QAM DSP flow.

To decrease complexity of implementing hybrid modulation we can share the FOC block. The offset estimation is performed after the initial FFT and before splitting the subchannel data between the two DSP flows. We use two frames as a preamble for frequency offset estimation and compensation. Implementing the FOC in an ASIC is simple and could be neglected compare to the other DSP sections [51].

The carrier phase recovery stage was explained in previous sections. We use a training-symbol-based (data aided) algorithm, with a single phase shift for each frame of data for both DMT and DFT-S QAM. The complexity of this CPR method is much lower than that of the blind equalization blocks (MMA or DD-MLS), and therefore it can be neglected in our complexity comparison.

6.7.2 Implementation complexity of main contributors

Next we calculate the number of complex multipliers for DSP blocks with high complexity and estimate the overall complexity for hybrid and DMT. Blocks with dominant DSP complexity in this chapter can be divided in two categories: FFT/IFFT and equalizers. In the next two subsections we calculate number of complex multipliers per signal symbol (CPS) in FFT/IFFTs and equalizers.

FFT + IFFT

The implementation complexity for FFT and IFFT are the same. Each requires $N\log_2(N)/2$ complex multipliers implemented with a radix-2 algorithm, where N is the smallest power of two greater than or equal to the target FFT length. For highest efficiency of hardware resources, we choose a power of two for FFT size. Radix-4 is can be used to implement the FFT and requires only $3N\log(N)/8$ multipliers; however, requiring a power of four limits the options for FFT size even more [52, 53]. We chose the popular radix-2 algorithm for its popularity and greater freedom in choosing FFT length. CPS for a combined FFT and IFFT blocks is

$$CPS_{FFT+IFFT}^{radix-2} = 2 \times \log_2(N)/2 = \log_2(N). \tag{6.1}$$

Equalizer

Any equalizer can be implemented in the time domain (TDE) or the frequency domain (FDE). The computational complexity for FDE is much lower than TDE [54, 55], so we consider only FDE for our comparison.

Consider a frequency domain equalizer with N_{eq} taps and N_{SPS} samples per symbol. To obtain N_{eq}/N_{SPS} output symbols, we need N_{eq} complex multipliers to calculate the equalizer output, and N_{eq} complex multipliers to update equalizer taps. Furthermore, we need eight length N_{eq} FFTs [36]. The CPS for an equalizer with N_{eq} taps, and N_{SPS} number of samples per symbol using the FDE technique is

$$CPS_{EQ}^{FDE} = \left[2N_{eq} + 4N_{eq}\log_2(N_{eq})\right] N_{SPS}/N_{eq} \tag{6.2}$$

6.7.3 Number of multipliers per bit

CPS is a good figure metric for system complexity, but it cannot show the hardware efficiency with bit rate. For such a comparison it is better to calculate the number of required multipliers per bit (CPB) which is

$$CPB = CPS/(BR/BW), \tag{6.3}$$

where BR is the overall bit rate of the system, and BW is the overall frequency range covered by the DAC (64 GHz in our work). BR/BW shows the number of bits per single symbol that is uploaded to the DAC.

6.7.4 Quantifying multiplies/bit

Figure 6.8 shows the CPB as a function of bit rates for standard DMT (red triangle markers) and our optimized hybrid modulation format (blue triangle markers). We provide a bar chart breakdown of contributions to the CPB for 320 Gb/s. The CPB portions of the DFT-S QAM FFT (transmitter) and IFFT (receiver), the DD-LMS, and the MMA are shown with green, gray, and blue boxes, respectively. In the following we explain details of this complexity calculation and the parameters we chose for different cases.

The overall number of multipliers per bit of the common FFT and IFFT blocks is calculated from (6.1) and (6.3). This value is indicated as a red box in the bar chart of Fig. 6.8. We used an FFT size of $N_{FFT} = 1024$ for the common FFT/IFFT blocks. This is the contribution used to trace the DMT complexity curve.

For hybrid modulation, the CPB for all frequency domain equalization and the DFT-S QAM pair of IFFT/FFT is

$$CPB = \frac{6 + 8\log_2(N_1) + 4\log_2(N_2) + \log_2(N_{QAM})}{BR/BW} \tag{6.4}$$

where N_{QAM} is the smallest power of two greater than or equal to the number of sub-channels dedicated to DFT-S QAM portion. At each bit rate, we used the optimum frequency occupation presented in Fig. 6.8 to find N_{QAM}. Only two values of N_{QAM} are used: 512 for occupancy below 50%, and 1024 occupancy above 50%.

In our BER simulation reported in previous sections, we assumed a sufficiently large number of taps for equalizers to have the best achievable performance. This led to N_{eq} of 77 for MMA and 43 for DD-LMS. To quantify complexity, we reduced the number of taps until the performance penalty was less than that of a 0.5 dB decrease in SNR. We restricted ourselves to powers of two when finding the reduced number of taps, leading to N_{eq} of 32 for MMA and 16 for DD-LMS. The N_{SPS} for MMA is two and for DD-LMS is one. The bar chart contributions of MMA and DD-LMS reflect these values. Complexity parameters are summarized in table 6.2.

For the swept bit rates, the frequency occupancy of DFT-S QAM only varies from 40 to 55% per Fig. 6.7. Therefore, the number of multipliers is virtually unchanging across swept bit rates. The CPB (i.e., *per bit*) for the hybrid is decreasing almost linearly with bit rate due to (6.4) denominator of BR.

Table 6.2 – Parameters for Hybrid Modulation DSP

Parameter	Value
N_1	32
N_2	16
N_{FFT}	1024
N_{QAM}	512-1024

6.7.5 Comparative complexity

The plots in Fig. 6.8 for different bit rates cover the case of back-to-back communications, i.e., without dispersion compensation complexity included. Comparing the complexity for different blocks at 320 Gb/s bit rate in Fig. 6.8, the largest portion of the overall multipliers per bit is for the MMA algorithm. In large part this is due to requiring two samples per symbol. MMA, DD-LMS and DFT-S QAM FFT/IFFT blocks consume 87% of the overall number of complex multiplexers per bit for hybrid modulation. This leads to a large difference between DMT and hybrid complexity for the back-to-back case. The complexity difference becomes smaller as we increase bit rate and use the same hardware to send more bits.

For long haul systems, a chromatic dispersion (CD) compensation block is needed for both hybrid and DMT. This CD bloc has complexity on a par with the rounded blocks in Fig. 6.1 for longer links. The number of taps for a CD compensation filter from [52]

$$N_{CD} \approx \frac{LDcRs^2}{4f_c^2}, \tag{6.5}$$

where L is the fiber length in km, D is the dispersion, f_c is the laser frequency, and R_s is the sampling rate. For $f_c = 193$ THz, $R_s = 64$ Gsamples/s, and $D = 18$ ps/nm·km, we obtain $N_{CD} \approx 0.14L$. For short range, $L < 20$ km, four taps are enough. By increasing fiber length to 285 km we need 40 taps and 10.8 multiplexers per bit at 320 Gb/s to remove CD. In this case, the additional hybrid complexity is only 52% of overall complex multipliers. This percentage becomes smaller with increasing fiber length and makes hybrid a good choice for long haul applications.

6.8 Conclusion

We present a numerical study of a hybrid modulation format in which we combine DFT-S QAM for lower frequencies and DMT for higher frequencies. We optimized hybrid modulation for: driving strategy, DFT-S QAM modulation order, and DFT-S QAM frequency spectrum allocation. The performance of the optimized hybrid is compared to that of DMT and we show an improvement with hybrid modulation. The improvement decreases as we increase bit rate in a fixed available bandwidth. The maximum bit rate under hard decision FEC threshold

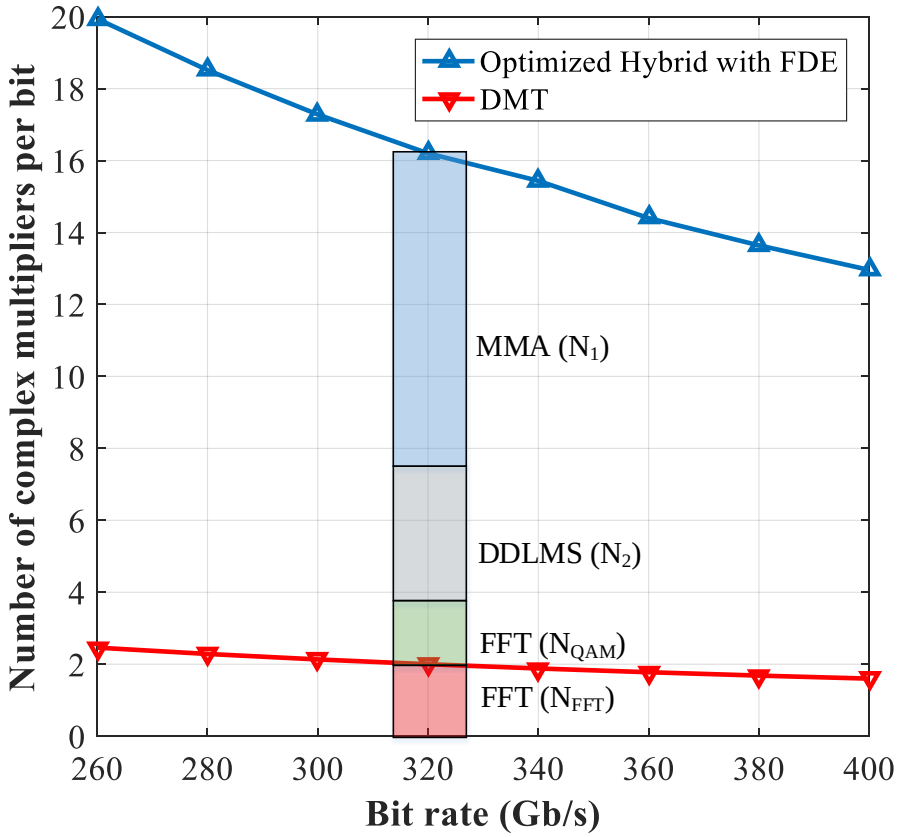

Figure 6.8 – For system bandwidth of 25 GHz, modulator output power of 0.42 mW and noise power of -33 dBm: Number of complex multipliers per bit of hybrid modulation and DMT modulation versus bit rate.

of 3.8e-3 is increased by 40 Gb/s with hybrid modulation instead of DMT. We calculate the number of complex multipliers per bit to compare the complexity between hybrid and 100% DMT. Complexity of hybrid modulation is much higher than DMT for back to back links, but low for links longer than several hundred kilometers.

Chapter 7

Conclusions and Future Work

In this thesis we study the best solutions for Terabit Ethernet as the next generation optical communication system. In the first part of this thesis we focus on short haul applications which requires high transmission rate with low complexity and low cost. We experimentally and theoretically compared PAM and DMT as the best modulation format candidates to achieve high transmission rate with low complexity, because of their compatibility with intensity modulation and direct detection. The second part is about increasing system performance with an advanced modulation format in which we combined DFT-S with DMT to increase the system capacity while preventing high PAPR. This solution is suggested for future coherent detection applications where the implementation cost is reduced we can use advanced modulation formats with high level of spectral efficiency.

In Chapter 2, for the first time, we report more than 100 Gb/s DMT transmission using an O-band silicon photonic modulator with 23 GHz 3 dB bandwidth with IMDD. This chapter provides a low cost low complexity solution for next generation short reach optical communication. We reach 120 Gb/s at 2 km and 110 Gb/s at 10 km, below the hard decision FEC threshold of 3.8e-3. Next we experimentally compared the performance of our DMT transmission with PAM. Results show that for fiber length less than 10 km DMT is a better choice but PAM is the winner if we increase fiber length more than 10 km. PAM is better than DMT for O-band data transmission as it has longer system reach and lower complexity compared to DMT.

In Chapter 3 we focus on C-band solution for 100 Gb/s data transmission. Because of non-zero dispersion on C-band we used SSB-DMT to avoid power fading. As the target of this chapter is short haul applications we considered the phase noise effect caused by a low cost laser. Interaction of laser phase noise with chromatic dispersion was studied on SSB-DMT signal with IMDD. This interaction creates P2A, ICI and power degradation. P2A noise was previously studied on single carrier OOK modulation and our work was the first study of P2A on DMT. Former studies of dispersion-induced ICI and power degradation effects considered

SSB-OFDM with zero padding half of the subcarriers to eliminate the SSBI effect. We used all subcarriers to increase spectral efficiency and we also studied the effect of SSBI degradation. The signal to carrier power ratio is optimized for SSB-DMT by trading off the P2A noise and SSBI. We extract theoretical expressions to calculate BER for any combination of fiber length, laser phase noise and system bandwidth.

Chapter 4 is a theoretical comparison between the best O-band solution and the best C-band solution for next generation optical communication targeting short haul applications. Chapter 2 showed that the best modulation choice on O-band is PAM. In this chapter for PAM modulation we went a step further and considered non-precompensated PAM to reduce the implementation complexity by removing expensive DAC. The only DSP we used for PAM is a block of equalizer at the receiver side. For C-band solution we used SSB-DMT studied in Chapter 3. PAM is not a good solution on C-band because chromatic dispersion and power fading is more severe on PAM compared to DMT. In this chapter we presented a theoretical analysis to fairly compare DMT and PAM. Our comparison shows that increasing fiber length C-band SSB-DMT is a better solution compared to O-band PAM. Therefore the distortion caused by high attenuation in O-band is more than the dispersion in C-band if we avoid power fading.

Chapter 5 is the first experimental demonstration of hybrid modulation on a silicon photonics IQ modulator. In this chapter we target future coherent detection systems with low complexity and study hybrid modulation in a back-to-back situation. Our experiment shows that the use of hybrid modulation increases the performance of a silicon photonics modulation in an SNR-limited regime.

In Chapter 6, we numerically study the performance of the hybrid modulation format. The first step is developing a driving strategy by trading off the effect of the transfer function nonlinearity and AWGN. Then the hybrid combination is optimized in terms of modulation order and frequency occupation for DFT-S partition. We compared optimized hybrid modulation with standard DMT for different bit rates. The improvement decreases as we increase the bit rate in a fixed available bandwidth. The complexity of hybrid modulation is compared to standard DMT in terms of required complex multipliers to implement each modulation format in ASIC or FPGA. For B2B the additional complexity for hybrid modulation format compared to standard DMT is large but by increasing link length more than several hundred kilometers this percentage becomes smaller.

There are several research opportunities to further the work presented in this thesis. Some of these possibilities are listed below:

- In our theoretical comparison in chapter 4 we focused on low complexity non pulse shaped PAM for short range communication. The next step should be considering pulse

shaped QAM modulation for long haul applications in O-band. This study helps us to theoretically investigate the effect of different pulse shaping methods.

- The fiber nonlinearity is neglected in Chapter 3 and Chapter 4. Including fiber nonlinearity in a theoretical study helps to investigate the feasibility of SSB-DMT for long haul applications.
- In Chapter 3 we assumed there is no zero padding. The next step should be optimizing the number of zero padded subchannels to further optimize the DMT signal.
- In Chapter 3 and Chapter 4 we didn't use any clipping method to focus on the hybrid modulation format and see how it can reduce PAPR and enhance the performance. Effect of clipping on hybrid modulation should be studied as future work.

Appendix A

SNR per subchannel estimation for DMT

To find the difference between different sub-channels we should send same data in all of them and see the difference between their outputs. To find this difference we sent QPSK signal in all channels with same power allocation. Comparing transmit and received data we can approximate SNR using calculated SER and EVM for each subcarrier.

A.1 SER to SNR calculation

Assuming additive white Gaussian noise we can calculate symbol error rate of QPSK modulation format in terms of SNR: Gaussian probability Sdistribution with variance σ^2 and mean μ is:

$$P(x|\mu,\sigma) = \frac{1}{\sigma\sqrt{2\pi}} e^{-\frac{(x-\mu)^2}{2\sigma^2}}, \tag{A.1}$$

where $\sigma^2 = N0$ is the noise power.

To calculate SER we first the probably of wrong decision at the receiver assuming transmit symbol of S_1. Same calculation is valid for all QPSK symbols and as symbols are uniformly distributed it is equal to the overall symbol error rate.

$$P(\text{correct decision}|S_1) = P(I_y > 0|S_1)P(Q_y > 0|S_1) = \left(1 - \frac{1}{2}\text{erf}\left(\sqrt{\frac{E_s}{2N_0}}\right)\right)^2. \tag{A.2}$$

$$P(\text{wrong decision}|S_1) = 1 - P(\text{correct decision}|S_1) \approx \frac{1}{2}\text{erf}(\sqrt{\frac{E_s}{2N_0}}), \tag{A.3}$$

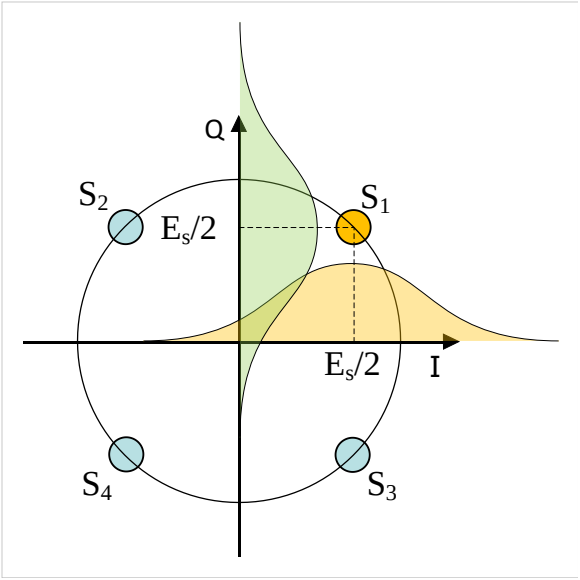

Figure A.1 – QPSK symbol in the presence of additive white Gaussian noise.

where $E_S/N_0 = SNR$ and SER is

$$SER = 2\left(\text{erf}^{-1}(SER)\right)^2 \tag{A.4}$$

To calculate SER in experiment or simulation we calculate number of wrong decisions and divide it by number of symbols. To have an accurate SNR estimation we need to have an accurate SER calculation, which means having more than 100 wrong decisions. When the SNR is high, accurate SER estimation means processing a high volume of symbols.

A.2 EVM to SNR calculation

EVM is another measurement of transmission quality, in this method we calculate the power ratio between error vector and actual signal vector

Figure A.2 shows the concept of EVM. In this figure red dot shows the position of received data and orange circle shows the position of transmit symbol. The EVM in dB is

$$EVM = 20\log\left(\frac{P_{error}}{P_{ref}}\right) \tag{A.5}$$

And the SNR approximation from EVM using same algorithm as in [56] is

$$EVM \approx \frac{1}{k\sqrt{SNR}}, \tag{A.6}$$

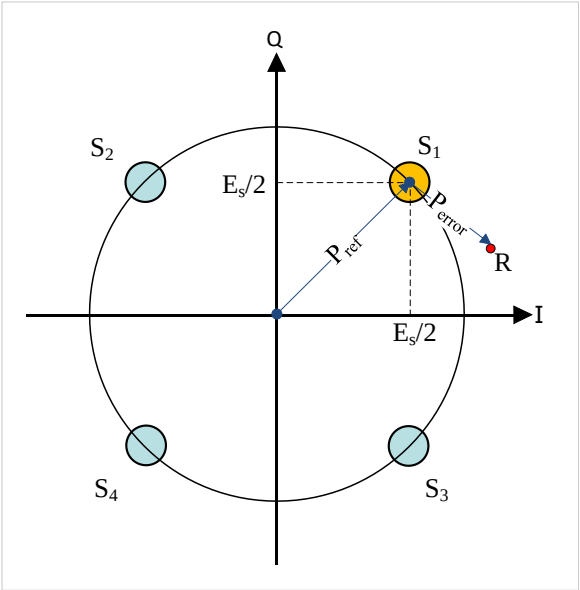

Figure A.2 – EVM calculation.

where k is modulation dependent factor and $k = 1$ for QPSK. To calculate EVM we use decision directed method to locate reference symbol. To have an accurate EVM calculation we need to locate symbol correctly which means we have a higher limit for noise power or lower limit for SNR. This limit is around 7 dB [56].

Figure A.3 shows the difference between EVM and SER estimation of SNR. In this figure we add AWGN noise to QPSK data with a known SNR (red curve), then we approximate SNR from EVM (blue curve), and from SER (black curve). Figure A.3 black curve accuracy is limited to SNR less than 10 dB as we have limitation in number of symbols. Blue curve accuracy is limited to SNR less than 7 dB, and validates results from [56].

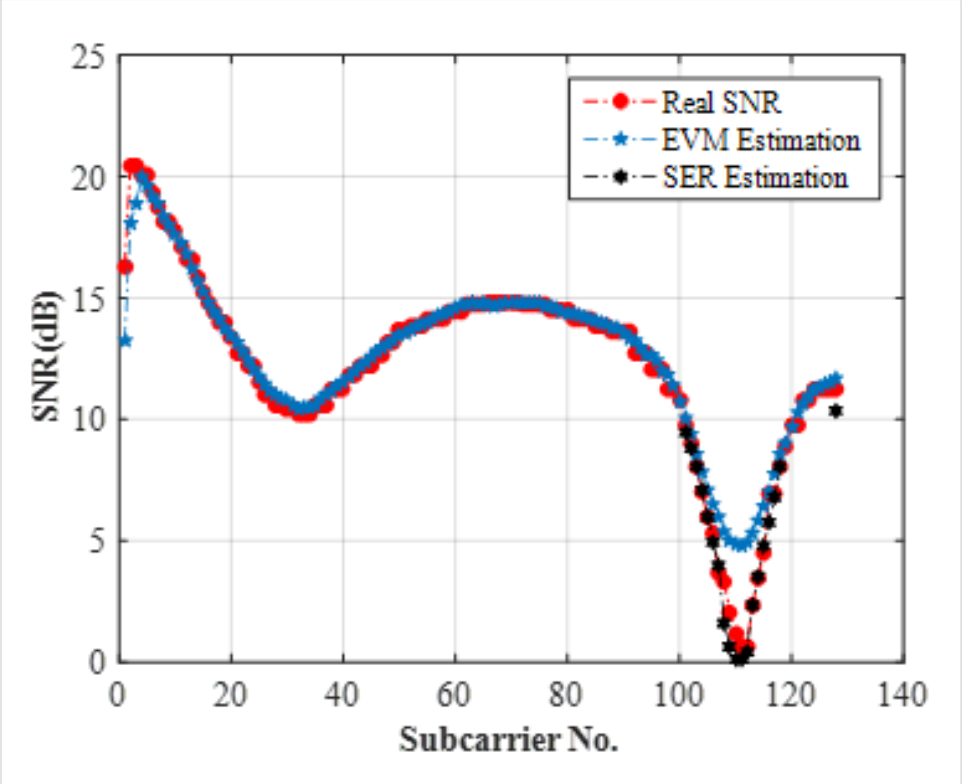

Figure A.3 – Evaluation of SNR estimation.

Appendix B

Simulation of uniform SSB-DMT transmission and SNR estimation

Figure B.1 shows the simulation setup and DSP flowchart for uniform SSB-DMT transmission. The transmitter side DSP generates a PRBS that is modulated onto complex QAM symbols for single sideband uniform DMT. The frequency domain signal is converted to the time domain via the IFFT with size equal to twice the number of subchannels. To remove dispersion induced ISI, a sufficiently long cyclic prefix is added to the signal. Parallel-to-serial conversion, clipping and quantization are the last DSP blocks.

The DAC is simulated as an 8-bit quantization at 64 GSamples/sec; correspondingly, the overall two-sided frequency spacing is 64 GHz. The resolution of the DAC is assumed to be 8 bits. The peak to average power ratio is mitigated with a clipping ratio of 10 dB. Simulations were performed to confirm that using a DAC with fewer bits led to quantization noise that would have impaired performance. The DAC provides I and Q data outputs for the DDMZM. The DDMZM is modeled as in [15], and by a Gaussian transfer function whose bandwidth is adjusted for the scenario to be simulated. Indeed this transfer function is used to capture the bandwidth limitation of the channel.

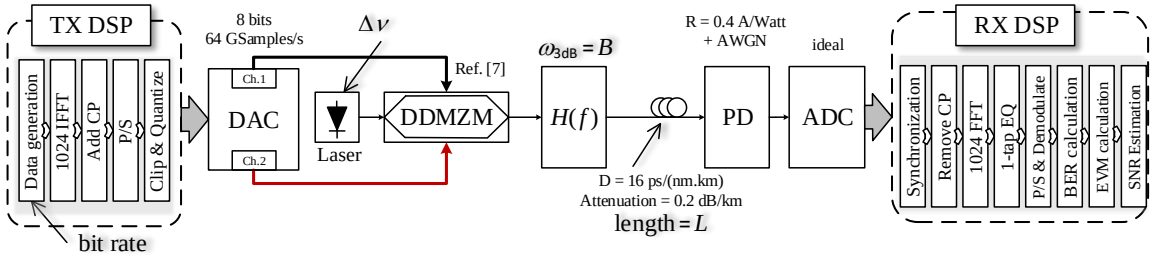

Figure B.1 – Monte Carlo simulation block diagram and DSP flowchart for uniform SSB-DMT transmission.

The laser phase noise is modeled as a Wiener process with a specified linewidth $\Delta\nu$. The modulated light is propagated in a fiber of a given length L using typical C-band characteristics: 16 ps/(nm×km) dispersion and 0.2 dB/km attenuation. The signal is photodetected (PD) and modeled as a square law device with AWGN. The AWGN is meant to capture both thermal and shot noise and is included in the analysis in the $SNR_{k(RS)}$ term. An ideal analog to digital converter (ADC) is assumed for detection, i.e., no distortion. The receiver data is synchronized and the cyclic prefix is removed in the time domain. The signal is converted to the frequency domain via an FFT. After one-tap equalization the EVM of each subchannel signal is calculated. Then the data is demodulated and the SER for each subchannel is calculated. Using EVM and SER we estimate SNR per subchannel (SNR estimation from EVM is valid for low EVM and SNR estimation from SER is accurate when the number of errors and EVM are high).

The estimated SNR from this Monte Carlo simulation is used to validate our theoretical expressions in section 3.4.1. Once validated, theoretical expressions will be employed in sections 3.5 and 3.6 for SSB-DMT.

Appendix C

SSBI calculations

SSBI is the interference caused by subchannels beating with each other; it is independent of carrier power. This contribution can be shown to be

$$\begin{aligned} & P_c\gamma^2 \left(\left| \sum_{k=1}^{N} d_k e^{j[2\pi k\Delta f(t-T_k)+j\Phi(t-T_k)]} \right|^2 - \left[\sum_{k=1}^{N} |d_k|^2 \right] \right) \\ & \approx 2P_c Re \left[\gamma^2 \sum_{n=1}^{N} \sum_{\substack{m=1 \\ m\neq n}}^{N} d_n d_m^* e^{j2\pi(n-m))\Delta ft} \right], \end{aligned} \tag{C.1}$$

where the interplay with phase noise and chromatic dispersion were neglected in the approximation, i.e., $T_k = 0$ and $\Phi(t) = 0$. To calculate the noise power per subchannel, consider the SSBI frequency domain representation. Each uniform SSB-DMT subchannel has an equal power delta function; square law detection is a convolution of the uniform SSB-DMT signal with itself in the frequency domain, so that $SSBI(f)$ is

$$\sum_{n=1}^{N} \sigma_{n(s)}^2 \delta(f - n\Delta f) * \sum_{m=1}^{N} \sigma_{n(s)}^2 \delta(f - m\Delta f) \tag{C.2}$$

The convolution yields the following result for an individual subchannel

$$\sigma_{k(SSBI)}^2 = \sum_{n=-N}^{N} \sigma_{n(S)}^2 \sigma_{k-n(S)}^2. \tag{C.3}$$

Recalling that $N\sigma_{n(S)}^2 = P_c\gamma^2$, we see that the sum of the variance per subchannel yields the total SSBI (C.1).

Appendix D

SER calculation

The noise contributions in (3.17) are modeled as AWGN. Therefore, the SNR in a given subchannel determines its symbol error rate. When conditioned on a given phase rotation θ, the subchannel symbol error can be found via the complementary error function erfc. If the channel has a bandwidth limitation, the SNR_k is reduced by the channel filter (a Gaussian filter with 3 dB bandwidth of B) attenuation at that subchannel.

Points in a regular MQAM constellations have two, three or four nearest neighbors: more neighbor implies, higher SER. Points with two nearest neighbors (2NN) have SER_{2NN} given by

$$\begin{aligned}\int_{-\infty}^{\infty} \Bigg[1 - \Bigg(\Bigg[1 - \frac{1}{4}\mathrm{erfc}\left(b\sqrt{SNR_k}\cos\left(\frac{\pi}{4}+\theta\right)\right) \\ -\frac{1}{4}\mathrm{erfc}\left(b\sqrt{SNR_k}\cdot\sin\left(\frac{\pi}{4}+\theta\right)\right)\Bigg]\Bigg)^2\Bigg] f_k(\theta)d\theta,\end{aligned} \tag{D.1}$$

where b is the normalization factor of MQAM varying with M, and $f_k(\theta)$ is the probability density function of PR, a zero mean Gaussian with a variance of σ_{PR}^2.

For constellation points with three nearest neighbors (3NN) we have SER_{3NN} given by

$$\begin{aligned}\int_{-\infty}^{\infty} \Bigg\{1 - \Bigg[1 - \frac{1}{2}\mathrm{erfc}\left(k\sqrt{\frac{2E_s}{N_0}}\cdot\cos\left(\frac{\pi}{4}+\theta\right)\right) \\ -\frac{1}{2}\mathrm{erfc}\left(k\sqrt{\frac{2E_s}{N_0}}\cdot\sin\left(\frac{\pi}{4}+\theta\right)\right)\Bigg] \\ \Bigg[1 - \frac{1}{4}\mathrm{erfc}\left(k\sqrt{\frac{2E_s}{N_0}}\cdot\cos\left(\frac{\pi}{4}+\theta\right)\right) \\ -\frac{1}{4}\mathrm{erfc}\left(k\sqrt{\frac{2E_s}{N_0}}\cdot\sin\left(\frac{\pi}{4}+\theta\right)\right)\Bigg]\Bigg\} f(\theta)d\theta.\end{aligned} \tag{D.2}$$

For constellation points with four nearest neighbors (4NN) we have SER_{4NN} given by

$$\int_{-\infty}^{\infty} \left\{ 1 - \left[1 - \frac{1}{2}\text{erfc}\left(b\sqrt{SNR_k} \cdot \cos\left(\frac{\pi}{4} + \theta \right) \right) \right. \right. \\ \left. \left. -\frac{1}{2}\text{erfc}\left(b\sqrt{SNR_k} \cdot \sin\left(\frac{\pi}{4} + \theta \right) \right) \right]^2 \right\} f(\theta) d\theta. \tag{D.3}$$

Finally the overall SER for MQAM is

$$SER_{MQAM} = \frac{1}{M} \sum_{i=1}^{M} SER_i. \tag{D.4}$$

where SER_i is replaced by SER_{jNN} for constellation point i with j nearest neighbors. Assuming Gray coding, the overall BER for MQAM is

$$BER_{MQAM} = \frac{1}{\log_2 M} SER_{MQAM}. \tag{D.5}$$

Publication List

During my PhD, I had the privilege of contributing to the following research works, some of which were presented in detail in this thesis:

1. A. Yekani, and L. A. Rusch, "Numerical Study of a Hybrid Optical DMT/DFT-S QAM Modulation ", *submitted to Journal of Lightwave Technology.*

2. A. Yekani, and L. A. Rusch, "Interplay of Bit Rate, Linewidth, and Reach on Optical DMT and PAM with IMDD ", *submitted to IEEE Transactions on Communications.*

3. A. Yekani, and L. A. Rusch, "Flexible Modulation and Frequency Allocations for SNR-limited Coherent Systems ", *Canadian Conference on Electrical and Computer Engineering*, 2018.

4. H. Sepehrian, A. Yekani, L. A. Rusch, and W. Shi, "Bandwidth-Aware Figure of Merit for Silicon-Photonic Depletion Mode Modulators", *Optical Fiber Communication Conference*, 2018, paper Tu2E.2.

5. A. Yekani, S. Amiralizadeh, and L. A. Rusch, "Analytical Study of Optical SSB-DMT with IMDD", *Journal of Lightwave Technology*, vol. 36, no. 3, pp. 666–674, Apr. 2018.

6. A. Yekani, S. Amiralizadeh, and L. A. Rusch, "Interplay of Bit Rate, Linewidth, and Reach on DMT vs. PAM Performance ", *Conference on Lasers and Electro-Optics*, 2016, paper SF1L.6.

7. H Sepehrian, A. Yekani, L. A. Rusch, and W. Shi, "CMOS-Photonics Codesign of an Integrated DAC-Less PAM-4 Silicon Photonic Transmitter", *IEEE Transactions on Circuits and Systems*, vol. 16, no. 12, pp. 2158–2168, 2016.

8. S. Amiralizadeh, A. Yekani, and L. A. Rusch, "Discrete multi-tone transmission with optimized QAM constellations for short-reach optical communications", *Journal of Lightwave Technology*, Vol. 34, Issue 15, pp. 3515–3522, 2016.

9. A. Yekani, and L. A. Rusch, "PAM vs. DMT: A performance comparison of modulation formats for IMDD ", *Photonics North (PN)*, 2016.

10. A. Yekani, S. Amiralizadeh, and L. A. Rusch, "Comparison of 100 Gb/s O-band PAM-4 vs. C-band DMT for different laser linewidths and fiber lengths ", *Conference on Lasers and Electro-Optics*, 2016.

11. A. Yekani, M. Chagnon, C. S. Park, M. Poulin, D.V. Plant and L. A. Rusch, "Experimental comparison of PAM vs. DMT using an O-band silicon photonic modulator at different propagation distances ", *European Conference on Optical Communication* , 2015.

Bibliography

[1] A. Yekani, M. Chagnon, C. S. Park, M. Poulin, D. V. Plant, and L. A. Rusch, "Experimental comparison of PAM vs. DMT using an O-band silicon photonic modulator at different propagation distances," *European Conference and Exhibition on Optical Communication*, vol. 2015.

[2] A. Yekan, S. Amiralizadeh, and L. A. Rusch, "Analytical Study of Optical SSB-DMT with IMDD," *J. Lightwave Technol.*, vol. vol. 36, no. 3, pp. 0733–8724, 2018.

[3] "Cisco Visual Networking Index: Forecast and Methodology, 2016–2021," *Cisco Public Information*, vol. Sept., 2017.

[4] "Cisco Global Cloud Index: Forecast and Methodology, 2016–2021," *Cisco Public Information*, vol. Feb., 2018.

[5] P. D. Dobbelaere, A. Narasimha, A. Mekis, B. Welch, C. Bradbury, C. Sohn, D. Song, D. Foltz, D. Guckenberger, G. Masini, J. Schramm, J. White, J. Redman, K. Yokoyama, M. Harrison, M. Peterson, M. Mack, M. Sharp, R. LeBlanc, S. Abdalla, S. Gloeckner, S. Hovey, S. Jackson, S. Sahni, S. Yu, T. Pinguet, and Y. Liang, "Silicon photonics for high data rate optical interconnect," *IEEE Optical Interconnects Conf. (OI)*, vol. paper WA2, 2012.

[6] "IEEE P802.3bs 400GbE Task Force," vol. 2017.

[7] M. Poulin, C. Latrasse, J. F. Gagné, Y. Painchaud, M. Cyr, C. Paquet, M. Morsy-Osman, M. Chagnon, S. Lessard, and D. V. Plant, "107 Gb/s PAM-4 transmission over 10 km using a SiP series push-pull modulator at 1310 nm," *European Conference and Exhibition on Optical Communication*, vol. paper Mo.4.5.3, 2015.

[8] G. Contestabile, Y. Yoshida, A. Maruta, and K. Kitayama, "Four-Channel 100-Gb/s Per Channel Discrete Multitone Modulation Using Silicon Photonic Integrated Circuits," *J. Lightwave Technol.*, vol. vol. 34, no.1, pp. 79–84, 2015.

[9] S. Randel, F. Breyer, S. C. J. Lee, and J. W. Walewski, "Advanced Modulation Schemes for Short-Range Optical Communications," *IEEE J. Quantum Electron.*, vol. vol. 16, no.5, pp. 1280–1289, 2010.

[10] H. Chen, L. Li, W. Yan, B. Liu, Z. Tao, and J. C. Rasmussen, "Comparison of discrete multi-tone and pulse amplitude modulation under different distortions for 100Gb/s system," *Asia-Pacific Conference on Communications*, vol. 2013.

[11] Y. Kai, M. Nishihara, T. Tanaka, T. Takahara, L. Li, Z. Tao, B. Liu, J. C. Rasmussen, and T. Drenski, "Experimental comparison of pulse amplitude modu-lation (PAM) and discrete multi-tone (DMT) for short-reach 400-Gbps data communication," *European Conference and Exhibition on Optical Communication*, vol. paper Th.1.F.3, 2013.

[12] M. Chagnon, M. Osman, M. Poulin, C. Latrasse, J. F. Gagné, Y. Painchaud, C. Paquet, S. Lessard, and D. Plant, "Experimental study of 112 Gb/s short reach transmission employing PAM formats and SiP intensity modulator at 1.3 μm," *Opt. Expres*, vol. vol. 22, no. 17, pp. 21018–21036, 2014.

[13] Y. Kai, M. Nishihara, T. Tanaka, R. Okabe, T. Takahara, J. C. Rasmussen, H. Ishihara, K. Goi, and K. Ogawa, "130-Gbps DMT transmission using silicon Mach-Zehnder modulator with chirp control at 1.55- μm," *Optical Fiber Communication Conference*, vol. paper Th4A.1, 2015.

[14] P. S. Chow, J. M. Cioffi, and J. A. C. Bingham, "A practical discrete multitone transceiver loading algorithm for data transmission over spectrally shaped channels," *IEEE Trans. on Commun.*, vol. vol. 43, no. 2/3/4, pp. 773–775, 1995.

[15] L. Zhang, Q. Zhang, T. Zuo, E. Zhou, G. N. Liu, and X. Xu, "C-band single wavelength 100-Gb/s IM-DD transmission over 80-km SMF without CD compensation using SSB-DMT," *Optical Fiber Communication Conference*, vol. paper Th4A.2, 2015.

[16] W. R. Peng, "Analysis of Laser Phase Noise Effect in Direct- Detection Optical OFDM Transmission," *J. Lightwave Technol.*, vol. vol. 28, no. 17, pp. 2526–2536, 2010.

[17] Z. Li, M. S. Erkılınç, K. Shi, E. Sillekens, L. Galdino, B. C. Thomsen, P. Bayvel, and R. I. Killey, "SSBI Mitigation and the Kramers-Kronig Scheme in Single-Sideband Direct-Detection Transmission With Receiver-Based Electronic Dispersion Compensation," *J. Lightwave Technol.*, vol. vol. 35, no. 10, pp. 1887–1893, 2017.

[18] A. Mecozzi, C. Antonelli, and M. Shtaif, "Kramers–Kronig coherent receiver," *Optica*, vol. vol. 3, no. 11, pp. 1220–1227, 2016.

[19] Z. Li, M. S. Erklnç, R. Maher, L. Galdino, K. Shi, B. C. Thomsen, P. Bayvel, and R. I. Killey, "Two-Stage Linearization Filter for Direct-Detection Subcarrier Modulation," *IEEE Photonics Technology Letters*, vol. vol. 28, no. 24, pp. 2838–2841, 2008.

[20] X. Wang, J. Yu, Z. Cao, J. Xiao, and L. Chen, "SSBI mitigation at 60GHz OFDM-ROF system based on optimization of training sequence," *Opt. Express*, vol. vol. 19, no. 9, pp. 8839–8846, 2011.

[21] J. H. Yan, Y. W. Chen, B. C. Tsai, and K. M. Feng, "A Multiband DDO-OFDM System With Spectral Efficient Iterative SSBI Reduction DSP," *IEEE Photonics Technology Letters*, vol. vol. 28, no. 2, pp. 119–122, 2016.

[22] S. Randel, D. Pilori, S. Chandrasekhar, G. Raybon, and P. Winzer, "100-Gb/s discrete-multitone transmission over 80-km SSMF using single-sideband modulation with novel interference-cancellation scheme," *European Conference on Optical Communication*, vol. 2015.

[23] J. Ma, "Simple signal-to-signal beat interference cancellation receiver based on balanced detection for a single-sideband optical OFDM signal with a reduced guard band," *Opt. Letter*, vol. vol. 38, no. 21, pp. 4335–4338, 2013.

[24] W. R. Peng, I. Morita, and H. Tanaka, "Enabling high capacity direct-detection optical OFDM transmissions using beat interference cancellation receiver," *European Conference and Exhibition on Optical Communication*, vol. 2010.

[25] S. Yamamoto, N. Edagawa, H. Taga, Y. Yoshida, and H. Wakabayashi, "Analysis of laser phase noise to intensity noise conversion by chromatic dispersion in intensity modulation and direct detection optical-fiber transmission," *J. Lightwave Technol.*, vol. vol. 8, no. 11, pp. 1716–1722, 1990.

[26] M. Chagnon, M. Morsy-Osman, M. Poulin, C. Paquet, S. Lessard, and D. V. Plant, "Experimental parametric study of a Silicon Photonic Modulator Enabled 112 Gb/s PAM Transmission system with a DAC and ADC," *J. Lightwave Tech.*, vol. vol. 33, no. 7, pp. 1380–1387, 2015.

[27] N. Kikuchi, R. Hirai, and T. Fukui, "Practical Implementation of 100-Gbit/s/Lambda Optical Short-Reach Transceiver with Nyquist PAM4 Signaling using Electroabsorptive Modulated Laser (EML)," *Optical Fiber Communication Conference*, vol. paper Th3A.2, 2015.

[28] A. Samani, D. Patel, M. Chagnon, E. El-Fiky, R. Li, M. Jacques, N. Abadía, V. Veerasubramanian, and D. V. Plant, "Experimental parametric study of 128 Gb/s PAM-4 transmission system using a multi-electrode silicon photonic Mach Zehnder modulator," *Opt. Express*, vol. vol. 25, no. 12, pp. 13252–13262, 2017.

[29] J. Zhang, J. Yu, and H. C. Chien, "EML-based IM/DD 400G (4 x112.5-Gbit/s) PAM-4 over 80 km SSMF based on linear pre-equalization and nonlinear LUT pre-distortion for inter-DCI applications," *Optical Fiber Communication Conference*, vol. paper W4I.4, 2017.

[30] W. Wang, P. Zhao, Z. Zhang, H. Li, D. Zang, N. Zhu, and Y. Lu, "First Demonstration of 112 Gb/s PAM-4 Amplifier-free Transmission over a Record Reach of 40 km Using

1.3 μm Directly Modulated Laser," *Optical Fiber Communication Conference*, vol. paper Th4B.8, 2018.

[31] L. Zhang, T. Zuo, Y. Mao, Q. Zhang, E. Zhou, G. N. Liu, and X. Xu, "Beyond 100-Gb/s Transmission Over 80-km SMF Using Direct-Detection SSB-DMT at C-Band," *J. Lightwave Tech.*, vol. vol. 34, no. 2, pp. 723–729, 2016.

[32] P. Dong, J. Lee, Y. K. Chen, L. L. Buhl, S. Chandrasekhar, J. H. Sinsky, and K. Kim, "Four-Channel 100-Gb/s Per Channel Discrete Multitone Modulation Using Silicon Photonic Integrated Circuits," *J. Lightwave Tech.*, vol. vol. 34, no. 1, pp. 79–84, 2016.

[33] J. Zhou, L. Zhang, T. Zuo, Q. Zhang, S. Zhang, E. Zhou, and G. N. Liu, "Transmission of 100-Gb/s DSB-DMT over 80-km SMF Using 10-G class TTA and Direct-Detection," *European Conference and Exhibition on Optical Communication*, vol. 2016.

[34] W. A. Ling, Y. Matsui, H. M. Daghighian, and I. Lyubomirsky, "112 Gb/s transmission with a directly-modulated laser using FFT-based synthesis of orthogonal PAM and DMT signals," *Opt. Express*, vol. vol. 23, no. 15, pp. 19202–19212, 2015.

[35] Y. Kai, M. Nishihara, T. Tanaka, T. Takahara, L. Li, Z. Tao, B. Liu, J. C. Rasmussen, and T. Drenski, "Experimental comparison of pulse amplitude modulation (PAM) and discrete multi-tone (DMT) for short-reach 400-Gbps data communication," *European Conference and Exhibition on Optical Communication*, vol. 2013.

[36] K. Zhong, X. Zhou, T. Gui, L. Tao, Y. Gao, W. Chen, J. Man, L. Zeng, A. P. T. Lau, and C. Lu, "Experimental study of PAM-4, CAP-16, and DMT for 100 Gb/s Short Reach Optical Transmission Systems," *Opt. Express*, vol. vol. 23, no. 2, pp. 1176–1189, 2015.

[37] A. Yekani, S. Amiralizadeh, and L. A. Rusch, "Interplay of Bit Rate, Linewidth, and Reach on DMT vs. PAM Performance," *IEEE Conference on Lasers and Electro-Optics*, vol. paper SF1L.6, 2017.

[38] W. A. Ling, I. Lyubomirsky, R. Rodes, H. M. Daghighian, and C. Kocot, "Single-Channel 50G and 100G Discrete Multitone Transmission With 25G VCSEL Technology," *J. Lightwave Technol.*, vol. vol. 33, no. 4, pp. 761–767, 2015.

[39] E. Pikasis, S. Karabetsos, T. Nikas, and D. Syvridis, "Rate-Adaptive DFT-Spread DMT and CDMA-DMT for 1-mm SI-POF Short-Range Links," *J. Optical Engineering*, vol. vol. 55, no. 10, pp. 1574–1577, 2016.

[40] T. M. Schmidl and D. C. Cox, "Robust frequency and timing synchronization for OFDM," *J. IEEE Transactions on Communications*, vol. vol. 45, no. 12, pp. 1613–1621, 1997.

[41] C. R. Berger, Y. Benlachtar, R. I. Killey, , and P. A. Milder, "Theoretical and experimental evaluation of clipping and quantization noise for optical OFDM," *Opt. Express*, vol. vol. 19, no. 18, pp. 17713–17728, 2011.

[42] S. Amiralizadeh, A. T. Nguyen, , and L. A. Rusch, "Modeling and compensation of transmitter nonlinearity in coherent optical OFDM," *Opt. Express*, vol. vol. 23, no. 20, pp. 26192–26207, 2015.

[43] X. Li and L. J. Cimini, "Effects of clipping and filtering on the performance of OFDM," *IEEE Communications Letters*, vol. vol. 2, no. 5, pp. 131–133, 1998.

[44] F. Li, J. Yu, J. Z. Z. Cao, M. Chen, and X. Li, "Experimental Demonstration of Four-Channel WDM 560 Gbit/s 128QAM-DMT Using IM/DD for 2-km Optical Interconnect," *J. Lightwave Tech.*, vol. vol. 35, no. 4, pp. 941–948, 2017.

[45] W. A. Ling, Y. Matsui, H. M. Daghighian, and I. Lyubomirsky, "112 Gb/s transmission with a directly-modulated laser using FFT-based synthesis of orthogonal PAM and DMT signals," *Opt. Express*, vol. vol. 23, no. 15, pp. 19202–19212, 2015.

[46] F. Zhang, J. He, R. Deng, Q. Chen, and L. Chen, "Performance improvement by orthogonal pulse amplitude modulation and discrete multitone modulation signals in hybrid fiber-visible laser light communication system," *J. Opt. Eng.*, vol. vol. 55, no. 10, pp. 55–55, 2016.

[47] W. A. Ling, I. Lyubomirsky, R. Rodes, H. M. Daghighian, and C. Kocot, "Single-Channel 50G and 100G Discrete Multitone Transmission With 25G VCSEL Technology," *J. Lightwave Tech.*, vol. vol. 33, no. 4, pp. 761–767, 2015.

[48] A. Yekani, , M.Banawan, , and L. A. Rusch, "Flexible Modulation and Frequency Allocations for SNR limited Coherent Systems," *Canadian conference on electrical and computer engineering*, vol. 2018.

[49] I. Fatadin, D. Ives, and S. J. Savory, "Blind Equalization and Carrier Phase Recovery in a 16-QAM Optical Coherent Sys-tem," *J. Lightwave Tech.*, vol. vol. 27, no.15, pp. 3042–3049, 2009.

[50] T. Pfau, S. Hoffmann, and R. Noe, "Hardware-Efficient Coherent Digital Receiver Concept With Feedforward Carrier Recovery for M -QAM Constellations," *J. Lightwave Tech.*, vol. vol. 27, no. 8, pp. 989–999, 2009.

[51] D. Perels, S. Haene, P. Luethi, A. Burg, N. Felber, W. Fichtner, and H. Bolcskei, "ASIC implementation of a MIMO-OFDM transceiver for 192 Mbps WLANs," *European Solid-State Circuits Conference*, vol. 2005.

[52] J. Leibrich and W. Rosenkranz, "Frequency domain equalization with minimum complexity in coherent optical transmission systems," *Optical Fiber Communication Conference*, vol. paper OWV1.5, 2010.

[53] A. Oppenheim and R. Schafer, "Discrete-time signal processing," *Prentice Hall*, vol. chap. 9, 2009.

[54] K. Zhong, X. Zhou, T. Gui, L. Tao, Y. Gao, W. Chen, J. Man, L. Zeng, A. P. T. Lau, and C. Lu, "Adaptive frequency-domain equalization in digital coherent optical receivers," *Opt. Express*, vol. vol. 19, no. 13, pp. 12789–12798 , 2011.

[55] J. Wei, Q. Cheng, R. V. Penty, I. White, and D. Cunningham, "Analysis of Complexity and Power Consumption in DSP-based Optical Modulation Formats," *Advanced Photonics for Communications*, vol. paper SM2D.5, 2014.

[56] R. Schmogrow, B. Nebendahl, M. Winter, A. Josten, D. Hillerkuss, S. Koenig, J. Meyer, M. Dreschmann, M. Huebner, C. Koos, J. Becker, W. Freude, and J. Leuthold, "Error Vector Magnitude as a Performance Measure for Advanced Modulation Formats," *IEEE Photonics Technology Letters*, vol. vol. 24, no. 1, pp. 62-63, 2012.